TAMPERE UNIVERSITY OF TECHNOLOGY
Degree Programme in Automation

ANTTI-JUHANA MÄKI

OPTICALLY INDUCED ELECTRIC FIELDS AND THEIR USE IN MICROFLUIDICS AND CELL MANIPULATION APPLICATIONS

Master of Science Thesis

Examiners:
Prof. Pasi Kallio, PhD Pekka Ronkanen

The topic and the examiners have been approved by the Faculty of Automation, Mechanical and Materials Engineering Council meeting on 09.12.2009

ABSTRACT

TAMPERE UNIVERSITY OF TECHNOLOGY
Master's Degree Programme in Automation Technology
MÄKI, ANTTI-JUHANA: Optically Induced Electric Fields and Their Use in Microfluidics and Cell Manipulation Applications
Master of Science Thesis, 98 pages, 9 appendix pages
June 2010
Major: Microsystem Technology
Examiners: Professor Pasi Kallio and PhD Pekka Ronkanen
Keywords: Droplet manipulation, digital microfluidics, electrowetting, optoelectrowetting, modelling

This thesis is a part of OPTIMI (Optically actuated microfluidics) project supported by Academy of Finland. The participants of the project were Tampere University of Technology (TUT) and Helsinki University of Technology (HUT). The goal of the project was to develop a flexible biomedical microfluidic system composed from completely optically induced components.

Electrowetting is a mechanism to transport microscale droplets electrically. In electrowetting-based manipulation, droplet is moved by locally modifying the surface tension of liquid. In this thesis, optically induced electrowetting, named as optoelectrowetting, that is using a photoconductive surface for addressing electric fields used for electrowetting, is presented. Optoelectrowetting provides a flexible, illumination-based creation of electric fields that are used to control surface tension of liquid. The scope of this thesis work is to develop a system where the optoelectrowetting mechanism could be implemented to enable manipulation of microliter droplets. This thesis focuses on modelling the optoelectrowetting device in order to provide the requirements for effective optoelectrowetting system. The idea is that these requirements could be used as a guideline for developing a reconfigurable microliter droplet manipulation platform using optoelectrowetting.

Theoretical backgrounds of the optoelectrowetting together with the closely related phenomena are discussed in the first part of this thesis. It includes also a short overview of applications, where optically triggered photoconductive layer have already been used. Furthermore, some potential applications are outlined in this part.

The second part of this thesis consists of experimental work and modelling. Based on the requirements for the effective optoelectrowetting manipulation presented in the experimental part, an optoelectrowetting device is proposed. Experiments that are supporting the proposed model are reported.

In the last part of this work, the refined requirements for effective optoelectrowetting manipulation are presented. As a result of the proposed model, the usability of the system is considered. In the end of this thesis, possible future development with the outlined device is discussed.

SUOMENKIELINEN TIIVISTELMÄ

TAMPEREEN TEKNILLINEN YLIOPISTO
Automaatiotekniikan koulutusohjelma
MÄKI, ANTTI-JUHANA: Optisesti luotujen sähkökenttien käyttö mikrofluidistiikan ja solumanipuloinnin sovelluksissa
Diplomityö, 98 sivua, 9 liitesivua
Kesäkuu 2010
Pääaine: Mikrosysteemitekniikka
Tarkastajat: Professori Pasi Kallio ja TkT Pekka Ronkanen
Avainsanat: Digitaalinen mikrofluidistiikka, pisaran pintajännityksen muuttaminen sähköisesti, optisesti luotujen sähkökenttien käyttö, mallintaminen

Tämä diplomityö on osa Suomen Akatemian rahoittamaa OPTIMI – projektia (Optisesti ohjattava mikrofluidistiikka), jossa tarkoituksena oli tutkia ja kehittää menetelmiä integroida useita erilaisia optisia ohjausmenetelmiä yhdelle alustalle. Projektin tavoitteena oli siinä kehitettyjen menetelmien hyödyntäminen mikrofluidistiikan eri sovelluksissa, esimerkiksi lääketieteellisessä diagnostiikassa ja analysoinnissa. Tampereen teknillisen yliopiston lisäksi projektissa oli mukana Teknillisen korkeakoulun (kuuluu nykyisin Aalto-yliopistoon) Automaatio- ja systeemitekniikan laitos.

Projektin ensimmäinen vaihe liittyi erilaisten optisesti ohjattujen menetelmien perehtymiseen ja arviointiin niiden toteuttamiskelpoisuudesta projektin puitteissa. Selvityksen perusteella tämän diplomityön aihe päätettiin rajata koskemaan vain mikropisaroiden manipulointia. Työn tavoitteena on mallintaa järjestelmä, jossa tilavuudeltaan mikrolitran kokoluokkaa olevaa pisaraa pystytään ohjaamaan valolla luotujen sähkökenttien avulla. Muut työn ydinaihetta läheisesti sivuavat aiheet, kuten valolla luotujen sähkökenttien käyttö solumanipuloinnin sovelluksissa, esitellään ainoastaan lyhyesti tässä työssä.

Mikrofluidistiikan avulla monet perinteiset laboratoriotestit voidaan siirtää yhdelle alustalle. Samalla testianalyysien automatisointiastetta on mahdollista kasvattaa, mikäli vain löydetään ratkaisu useamman eri toiminnon integroimiseen samalle alustalle. Lisäksi analyyseihin tarvittavaa aikaa pystytään pienentämään mikrofluidistiikan avulla, koska useat prosessit, esimerkiksi analyyseissä yleiset kemialliset reaktiot, tapahtuvat huomattavasti nopeammin pienemmässä tilavuudessa. Täten mikrofluidistiikka mahdollistaa analyysien nopeuden ja määrän merkittävän kasvattamisen. Massatuotannossa edullisten mikrofluidistiikkaan perustuvien analyysialustojen etuja perinteisiin menetelmiin verrattaessa ovat myös vähäisempi käytettävien aineiden, kuten kemikaalien, käyttö ja kulutus sekä kannettavien laitteiden suoma mahdollisuus paikan päällä tapahtuvaan seurantaan.

Perinteisessä mikrofluidistiikassa järjestelmät ovat rakennettu miniatyrisoimalla makromaailmassa käytettyjä komponentteja. Esimerkiksi nesteen liikuttelu tapahtuu tyypillisesti alustaan liitettyjen mikropumppujen avulla mikrokanavissa, joiden poikkileikkausmitat ovat yleensä alle millimetrin kokoluokkaa. Mittasuhteiden

pienentäminen aiheuttaa muun muassa sen, että nesteen virtausnopeus tietyllä paineella hidastuu mikrokanavassa verrattuna suurempaan kanavaan. Pienenemisestä johtuvat ilmiöt saattavatkin aiheuttaa merkittäviä pullonkauloja erityisesti nopeutta vaativissa analyyseissa. Seurauksena on helposti se, että kaikkien tarvittavien komponenttien, erityisesti tarpeeksi tehokkaiden pumppujen, miniatyrisointi yhdelle sirulle ei onnistu. Tästä johtuen viime aikoina onkin kehitelty useita erilaisia mikroluokan nesteiden siirtoon perinteisiä menetelmiä paremmin soveltuvia tekniikoita. Yksi kiinnostavimmista uusista tekniikoista on niin kutsuttu digitaalinen mikrofluidistiikka, jossa perinteinen jatkuva nestevirtaus mikrokanavissa on korvattu erillisten pisaroiden ohjaamisella.

Digitaalisessa mikrofluidistiikassa fyysiset mikrokanavat on korvattu pinnalla, jonka alla sijaitsee ohjattava elektrodimatriisi. Pisaroiden liikutteleminen tapahtuu niin kutsuttua electrowetting-periaatetta hyväksikäyttäen. Kyseisessä menetelmässä nestepisaran manipulointi onnistuu muuttamalla sen pintajännitystä tarpeeksi suuren sähkökentän avulla. Pintajännityksen vaihtuminen aiheuttaa muutoksen pisaran ja pinnan väliseen kontaktikulmaan. Kytkettäessä sähkökenttä vain yhdelle nestepisaran puolelle, pystytään pisaraan pintajännitystä muokkaamaan paikallisesti. Tällöin nestepisaran kontaktikulman muutos on erisuuruinen pisaran vastakkaisilla puolilla, luoden paine-eron pisaran sisälle, joka saa aikaan pisaran liikkumisen. Elektrodimatriisia sopivasti ohjaamalla pystytään samanaikaisesti manipuloimaan useampia pisaroita, täten mahdollistaen samanaikaisesti suuren määrän yksilöllisesti ohjattavia rinnakkaisia operaatioita.

Tyypillisesti järjestelmän mikroelektrodit valmistetaan perinteisillä mikropiirien valmistusmenetelmillä. Koska pienin mahdollinen liikuteltavissa oleva pisaran koko määräytyy käytettyjen mikroelektrodien perusteella, vähentää niiden käyttö alustojen uudelleenkäytettävyyttä erisuuruisten pisaroiden liikuttamisessa. Lisäksi, mikäli elektrodeja halutaan edelleen pienentää pienempien pisaroiden ohjaamista varten, niiden kytkeminen vaikeutuu. Tästä johtuen hiljattain on esitetty konsepti, jossa pisaran manipulointi perustuu esitettyyn electrowetting-periaatteeseen ilman yllä esitettyjä ongelmia. Sen toiminta perustuu valojohtavan kerroksen käyttämiseen sähkökenttien osoittamisessa. Kyseisen kerroksen johtavuutta pystytään paikallisesti kasvattamaan sopivalla valaistuksella. Esitetyssä järjestelmässä pisaran hallitsemiseen tarvittavat sähkökentät luodaan virtuaalisesti säädettävällä valolla. Koska koko elektrodikerros on samassa potentiaalissa, myös elektrodien yksilöllisestä osoituksesta aiheutuva ongelma poistuu. Toimintaperiaate on se, että kun valoa ei tuoda järjestelmään, valojohtavan kerroksen impedanssi on suuri. Tämä estää merkittävän sähkökentän vaikutuksen pisaraan. Valaistaessa valojohtavan kerroksen impedanssi pienenee, sallien pisaran valo-ohjatun kontrolloimisen. Tämä mahdollistaa joustavan ja uudelleen muokattavan järjestelmän rakentamisen mikrofluidistiikan eri sovelluksiin, ratkaisten samalla suurimmat perinteisessä digitaalisessa mikrofluidistiikassa esiintyvät ongelmat.

Tämän työn tarkoituksena on suunnitella laite, jolla mikroskooppisen mikropisaran ohjaaminen onnistuu optisesti luotujen sähkökenttien avulla. Yhteistyö projektissa oli

päätetty niin, että Teknillinen korkeakoulu kehittää ja valmistaa analyyseissä käytettävän alustan, kun taas Tampereen teknillinen yliopisto keskittyy alustan implementoimiseen mikrofluidistiikan sovelluksiin. Tästä johtuen tämän diplomityön pääpaino on optisesti luotujen sähkökenttien käytön mallintamisessa mikrofluidistiikan sovelluksiin.

Työn keskittyessä mallintamiseen, ilmiön taustan kartoittaminen perustui suurelta osin muiden tutkimusryhmien raportointeihin. Tässä katsauksessa tuli selkeästi esille, kuinka esitetyt mallit ja tutkimustulokset aiheesta ovat vielä ristiriitaisia. Koska projektin tavoitteena oli mahdollisimman monipuolisen ja toimivan järjestelmän rakentaminen, on tarkasteltavan ilmiön yksityiskohtainen tietämys erittäin tarpeellista. Työssä olikin ensiarvoisen tärkeää ymmärtää, miten optisesti luodut sähkökentät vaikuttavat nestepisaran käyttäytymiseen.

Työn ensisijaisena tavoitteena oli rakentaa malli, joka kuvaisi tarpeellisen tarkasti käsiteltyä ilmiötä. Julkaisuiden osittain ristiriitaisesta ilmiön esittämisestä johtuen tämän työn tuloksena ehdotetun mallin toimintaperiaate on uusi, vaikka se käyttääkin ilmiön mallintamisessa hyödyksi jo olemassa olevia ekvivalenttipiirejä. Huolimatta siitä, että uusi malli onkin hyvin pelkistetty, alustavien testien perusteella se todettiin olevan käyttökelpoinen ja siten soveltuvan haluttuun käyttötarkoitukseensa. Järjestelmän suunnittelussa aluksi muodostetaan sitä vastaava ekvivalenttipiiri, jossa eri kerrokset on mallinnettu niille sopivilla komponenteilla. Tämän jälkeen mallin avulla lasketaan näiden eri komponenttien arvot kyseisessä järjestelmässä. Kun saadut arvot sijoitetaan ekvivalenttipiiriin, on mahdollista laskea nestepisaran pintajännitykseen vaikuttavan voiman suuruus. Tämän perusteella pystytään arvioimaan, kuinka nestepisara käyttäytyy pinnalla. Mallin avulla on mahdollista myös tutkia, kuinka järjestelmän parametrien muuttaminen vaikuttaisi laitteen toimintaan. Tätä voidaan käyttää hyväksi kahdessa eri tapauksessa. Ensinnäkin, muodostettua mallia apuna käyttäen on mahdollista määritellä parhaiten sopivia ohjausparametreja jo valmiina oleviin järjestelmiin, sen avulla voidaan esimerkiksi löytää tietyn järjestelmän optimaalisin sähkökentän taajuusalue. Mallin avulla pystytään myös suunnittelemaan järjestelmä, joka mahdollistaa nestepisaran tehokkaan liikuttamisen optisesti luotujen sähkökenttien avulla.

Työssä kehitellyn mallin perusteella ehdotetun järjestelmän pitäisi mahdollistaa toivottu nestepisaran manipulointi optisest luotujen sähkökenttien avulla. Mahdollisessa jatkokehityksessä on ensiarvoisen tärkeää, että alustan rakentamiseen liittyvät ongelmat saadaan ratkaistua. Esimerkiksi elektrodien päällystäminen valojohtavalla kerroksilla todettiin erittäin haasteelliseksi. Valmistuksesta johtuvat vaikeudet tulivat konkreettisesti esille erityisesti omien mittausten aikana. Koska ilmiö on verrattain uusi eikä kattavaa teoriaa ole esitetty, on myös ensisijaisen tärkeätä panostaa ohjausmenetelmän taustalla vaikuttavien ilmiöiden tarkempaan teoreettiseen ja kokeelliseen tutkimiseen.

FOREWORD

This thesis has been made in the Department of Automation Science and Engineering at Tampere University of Technology as a part of OPTIMI project funded by Finnish Academy.

The examiners of this work have been Prof. Pasi Kallio and PhD Ronkanen. I would like to express my deepest appreciation to them for their precious guidance during this thesis.

The entire MST-group (Micro- and Nanosystems Research Group) has deserved my sincerest gratitude. The work community has been inspirational, helpful and pleasurable.

I have an honour to express my deepest gratitude to my parents Eevaliisa and Seppo and my sister Anniina who have always supported my studies. Even when 'n:th' academic year started. I would also like to thank my futsal team ACE and football team NePa for providing important counterbalance to the work and ensuring to stay physically (and mentally) fit. Furthermore, my friends have ensured that I do have something else than work to think on Friday nights, cheers for that! Finally, a special thanks to my girlfriend Mari for withstanding my sometimes long-lasting working days. I gotta feeling that everything gonna be better in the future.

Tampere, June 2010

Antti-Juhana Mäki
Tumppi 3 D 144
FIN-33720 Tampere
Tel.: +358 40 736 4613

TABLE OF CONTENTS

SYMBOLS AND ABBREVIATIONS

Symbols

A	[m^2]	Area
A_c	[m^2]	Droplet contact area
A_{dark}	[m^2]	Dark area
$A_{electrode}$	[m^2]	Electrode area
A_{light}	[m^2]	Light area
Bo		Bond number
c		Photoconductive ratio
C	[F]	Capacitance
C_d	[F]	Electrode-electrolyte interface capacitance
C_{ins}	[F]	Insulator layer capacitance
C_{liquid}	[F]	Liquid capacitance
C_{photo}	[F]	Photoconductor layer capacitance
C_s	[F/m]	Specific capacitance
d	[m]	Material thickness
d_e	[m]	Electrode width
E_{DB}	[V/m]	Theoretical dielectric strength
f_c	[Hz]	Cut-of frequency
F_{DEP}	[N]	Dielectrophoretic force
F_{EWOD}	[N]	Electrowetting force (Lippman force)
F_{EWOD_DB}	[N]	Electrowetting force when dielectric breakdown
F_{max}	[N]	Maximum electrowetting force
F_{max_sat}	[N]	Maximum contact angle saturation electrowetting force
F_{min}	[N]	Minimum electrowetting force
h	[m]	Height
g	[m/s^2]	Gravitational constant
$K(\omega)$		Clausius-Mossotti factor
p_{min}	[Pa]	Critical minimum pressure

r	[m]	Radius
r_c	[m]	Droplet contact radius
r_{cell}	[m]	Cell outer radius
r_{cyto}	[m]	Cell cytoplasm radius
R_b	[Ω]	Bulk resistance
R_d	[Ω]	Electrode-electrolyte interface resistance
R_{ins}	[Ω]	Insulator layer resistance
R_{liquid}	[Ω]	Liquid resistance
R_{photo}	[Ω]	Photoconductor layer resistance
R_{photo_dark}	[Ω]	Photoconductor layer resistance (dark area)
R_{photo_light}	[Ω]	Photoconductor layer resistance (light area)
$R_{photo\_tot\_no\_light}$	[Ω]	Total photoconductor layer resistance (dark state)
$R_{photo\_tot\_light}$	[Ω]	Total photoconductor layer resistance (light state)
U	[V]	Applied voltage
U_{DB}	[V]	Dielectric breakdown voltage
U_{OEW}	[V]	Voltage drop over insulator layer
$U_{OEW\_corrected}$	[V]	Corrected voltage drop over insulator layer
U_{ins}	[V]	Voltage over insulator layer
U_{layer_norm}		Normalized voltage over layer
U_{max}	[V]	Maximum voltage
U_{min}	[V]	Minimum voltage
U_{sat}	[V]	Saturation voltage
W_c	[J]	Molecules' cohesive energy per molecule
X_c	[Ω]	Reactance
Z	[Ω]	Impedance
Z_{abs}	[Ω]	Impedance (absolute value)
Z_{ins}	[Ω]	Insulator layer impedance
$Z_{interface}$	[Ω]	Transfer mechanism impedance
Z_{layer}	[Ω]	Layer impedance
Z_{liquid}	[Ω]	Liquid impedance
Z_{photo}	[Ω]	Photoconductive layer impedance

Z_{tot}	[Ω]	Total impedance
α	[rad]	Contact angle hysteresis
γ	[N/m]	Surface tension
γ_{LV}	[N/m]	Liquid-vapour surface tension
γ_{SL}	[N/m]	Solid-liquid surface tension
γ_{SL_eff}	[N/m]	Effective solid-liquid surface
γ_{SL0}	[N/m]	Solid-liquid surface tension at zero voltage
γ_{SV}	[N/m]	Solid-vapour surface tension
δ	[m]	Characteristic molecular dimension
$\Delta\theta$	[°]	Contact angle change in degrees
$\Delta\varphi$	[V]	Transmembrane potential
ε_0	[F/m]	Vacuum permittivity
ε_{cell}'	[F/m]	Cell permittivity using a single-cell approach
ε_{cyto}	[F/m]	Cell cytoplasm permittivity
ε_d		Relative permittivity
ε_m	[F/m]	Medium permittivity
ε_m^*	[F/m]	Complex medium permittivity
$\varepsilon_{membrane}$	[F/m]	Cell membrane permittivity
ε_p	[F/m]	Particle permittivity
ε_p^*	[F/m]	Complex particle permittivity
θ	[rad]	Contact angle
$\theta(U)$	[rad]	Contact angle at voltage U
θ_0	[rad]	Contact angle at zero voltage
θ_{0_d}	[°]	Contact angle at zero voltage in degrees
θ_d	[°]	Contact angle in degrees
θ_{sat}	[rad]	Saturated contact angle
ρ	[kg/m^3]	Density
σ	[S/m]	Material conductivity
σ_{me}	[S/m]	Medium conductivity
σ_p	[S/m]	Particle conductivity
ω	[radius/s]	Angular frequency

Abbreviations

AC	Alternative current
aFP	Amorphous fluoroploymer
AgCl	Silver chloride
a-Si	Amorphous silicon
a-Si:H	Hydrogenated amorphous silicon
CA	Contact angle
CM	Clausius-Mossotti
Cu	Copper
DB	Dielectric breakdown
DC	Direct current
DEP	Dielectrophoresis
DI	De-ionized
DLP	Digital Light Processing
DMF	Digital microfluidics
DNA	Deoxyribonucleic acid
E. coli	Escherichia coli
EDL	Electrical double layer
EW	Electrowetting (direct without an insulator layer)
EWD	Electrowetting on dielectrics
EWOD	Electrowetting on dielectrics
HeLa	A human epithelial cervical cancer cells taken from Henrietta Lacks
He-Ne	Helium-neon
HUT	Helsinki University of Technology
ITO	Indium tin oxide
LCD	Liquid Crystal Display
LED	Light-emitting diode
LDEP	Liquid dielectrophoresis
LOC	Lab-On-a-Chip
LOET	Lateral-field optoelectronic tweezers

MATLAB	The program used in the measurements and handling of the measurement results
MEA	Multi-Electrode Array
MST-group	Micro- and Nanosystems Research Group of Tampere University of Technology
NaCl	Sodium chloride
OET	Optoelectronic tweezers
OEW	Optoelectrowetting
OPTIMI	Optically actuated microfluidics
PDMS	Polydimethylsiloxane
PECVD	Plasma Enhanced Chemical Vapour Deposition
PGO	Praezisions Glas & Optik GmbH
RC circuit	An electrical circuit consisting of resistors and capacitors
RIE	Reactive Ion Etching
RMS	Root-mean-square
Si_3N_4	Silicon nitride
SiO_2	Silicon dioxide
SiOC	Carbon doped silicon oxide
SNR	Signal-to-noise ratio
SU-8	Epoxy-based negative photoresist
Teflon®	Brand name for polytetrafluoroethylene
TUT	Tampere University of Technology
UK	United Kingdom
WBC	Human white blood cell

1. INTRODUCTION

The concern with the area of miniaturized fluid mechanics has been relative high in the last decades because of the various benefits they could provide. Reduced sizes could allow effective automation and integration of multiple processes on a single chip, thus leading to enormous enhancement in functionality, precision and performance of the system when compared to corresponding device in macro world. Because of their benefits of scaling down, microfluidic technologies have become attractive in various areas including biomedical diagnostics, cell biology and tissue engineering. [1; 3; 4]

There are two main technologies for microfluidic devices, continuous-flow and droplet-based microfluidics. The systems based on continuous-flow are typically using closed microchannels fabricated by either a polymeric material or etched into silicon, glass or other solid materials, thus bringing several challenges such as liquid and contact-free interfacing problems. [5] For these reasons, devices that are manipulating discrete droplets have been demonstrated. Compared to conventional systems, the benefit of these systems, called as droplet-based or digital microfluidics, is that significantly lower amount of volumes are required.

Electrowetting, being one of the most used techniques in digital microfludic systems, is an effective tool for manipulating microscale droplets electrically. The working mechanism is to locally change the contact angle between the droplet and the surface, thus generating a pressure gradient inside the droplet that pushes the droplet towards the applied voltage region. Electrowetting-based fundamental microdroplet manipulation operations such as droplet creation and cutting, merging and transportation together with more complex tasks such as droplet mixing have been demonstrated [1; 3].

Optically induced electrowetting, usually called as optoelectrowetting, is a mechanism to control droplets by electrowetting mechanism using electric fields that are actuated by triggering the the photoconductive layer using light. This provides a flexible, dynamic and reconfigurable control of droplets by light. [48-53]

This thesis has been made as a part of OPTIMI (Optically actuated microfluidics) project that was supported by Academy of Finland. The goal of the project was to realize a dynamic and reconfigurable complete optical microfluidic system. The integration of multiple actuation methods on a single chip using optically induced microfluidics would provide a flexible tool with a massive parallel operation capability. This would revolutionize multiple research areas, for instance biological and medical.

The participants of the project OPTIMI were Helsinki University of Technology (HUT) and Tampere University of Technology (TUT). The tasks of the project were

distributed among the participants such that HUT designs and fabricates chips whereas TUT tests and develops biomedical applications for the fabricated chip.

The first task of the project was to investigate the possibilities to use a photoconductive surface in microscale applications. These include droplet manipulation using optically induced electrowetting (OEW), cell and particle control with optically created dielectrophoresis forces, cell electroporation, electrical lysis and stem cell stimulation. Based on the study, it was decided to focus on the OEW that enables manipulation of microscale droplets using optically generated electric field. The scope of this work is to model optically induced device and further propose a device that could be used for effective droplet manipulation after fabrication. Because the focus at TUT is on biotechnological life-science applications, for instance so-called Lab-On-a-Chip concepts, other potential electrowetting applications, such as focus lenses or display technology [1], are beyond the scope of this work and are not covered.

The structure of this thesis that has been done in Micro and Nanosystems Research Group (MST-group) of Tampere University of Technology is as follows. In Chapter 2, the theories of electrowetting and optically induced electrowetting are explained in details. Droplet manipulations using these introduced methods are considered from various aspects. Other closely related phenomena, such as optically induced dielectrophoresis, are briefly outlined in this part. To emphasize the wide usability of optically triggered photoconductive layer, Chapter 2 includes also a short overview of existing and potential applications.

In Chapter 3, the initial tests that were performed using the optoelectrowetting device given by the project are reported. The architecture of the device and the test set-ups are illustrated. This chapter explains also the optoelectrowetting modelling process that has been the main area of this thesis. The modelling process includes two parts. Firstly, the study of the models that have be presented in previous publications is described. Secondly, the modelling of the used optoelectrowetting is reported. This part contains also the description of the optoelectrowetting model and device that has been proposed based on the experiments and modelling.

Chapter 4 reports the experiments that have been performed to asses the proposed model presented in the previous chapter. Based on the observations during these experiments, the usability of the proposed model is considered. It also evaluates the obtained results of the work.

Finally, Chapter 5 draws a conclusion of this all and proposes steps for further development.

2. THEORETICAL BACKGROUND

This chapter presents different techniques to manipulate droplets, cells, and microparticles. Because the focus of this work is on optically induced droplet-based digital microfluidics, named as optoelectrowetting, this area will be introduced extensively. The theory of electrowetting, the underlying working mechanism of optoelectrowetting, is deeply reviewed. Digital microfluidics, electrowetting and optoelectrowetting are presented in the first three sections. In Section 2.4, other phenomena where optically induced electric field could be used, such as cell and particle manipulation, cell lysis and stem cell stimulation, are briefly discussed. Section 2.5 presents new potential applications, where the discussed mechanisms could be used.

2.1. Digital microfluidics

Microfluidics, as a result of the advantages of scaling down, is well suited for so-called Lab-On-a-Chip (LOC) concept that was first proposed in [4]. In LOC, which is nowadays one of the most remarkable areas of fluid mechanics, analytical processes are performed by multiple sequential operations, such as sample pre-treatment, analytical separation and detection and data analysis in a single microfluidic device.

Continuous-flow microfluidic devices can be separated into three different categories, capillary-driven, pressure-driven and centrifugal-based systems, based on their main driving mechanism [5]. While capillary-driven platforms are cheap to fabricate and have a simple working mechanism, they suffer low-level controllability. Pressure-driven systems allow more precise control and flexibility especially if structures are fabricated using comparative cheap, robust and disposable material such as PDMS. Furthermore, they are usually compatibility to standard lab equipment and almost all biochemical sensor principles can be integrated easily with these systems. Drawbacks of pressured-driven platforms are their increased complexity and liquid interfacing problems. In the last group, centrifugal force is used for driving the liquid. A system can be mounted with cheap and disposable plastic cartridges that can be applied to a wide range of different applications. However, these systems are missing the flexibility, thus having contact-free interfacing problems. [5] Recently, a new concept manipulating discrete droplets, typically volumes between $0.1 - 10$ microliters [6], have attained increased attention to overcome the problems related to conventional microfluidic systems. This concept, named as digital microfluidics, uses microdroplets and therefore requires only small volumes in operations. Furthermore, it enables much higher automation to be used when compared to conventional continuous-flow microfluidics. The concept of digital microfludics will be presented next.

2.1.1. Different digital microfluidics mechanisms

In some studies, two different technologies, a closed system where droplet manipulation is based on a two- or multiphase liquid-flow actuation in a physical microchannels, and an open system where droplets, located in a flat surface, are moved by actuating electrodes below the surface, have been used with term “digital microfluidics”. [7] Closed systems, where droplets are moved in microchannels using usually pressure, have high-throughput capability while their flexibility and functionally are considerable low because of their dependency on physical channels. On the other hand, open systems manipulate droplets on a planar surface by actuating electrodes typically arranged in a two-dimensional array. This allows a fabrication of a simple, cheap and flexible system without having any mechanical moving parts using conventional lithographic techniques. [5] In this work, the focus is on open systems and therefore the closed-systems based on droplet movement in physical microchannels are no further discussed. Furthermore, from now on in this thesis, terms closed and open microfluidics systems are only related to systems where droplets are located in a flat surface, and are used to describe two-plate and single-plate systems, respectively, as will be discussed in Section 2.2.4.

In digital microfluidics (DMF), where fluid is operated in a droplet form fixed by the geometry of the system (for instance size of the actuation electrodes), an immiscible surrounding such as air and oil is used to avoid lateral dispersion during transportation. While multiple droplets can be controlled independently at the same time, fluid is quantized and transportation is performed in multiples of the minimum unit volume. For this reason, the flow rate is determined differently in DMF than in a volumetric system, being a sum of the speed and the size of a single droplet times the number of droplets that have been transported [8]. There are several advantages in digital microfluidics architecture compared to continuous-flow, some of them presented next. First, because operations are carried out in a plate using direct electric control, neither moving parts such as pumps and valves nor physical microchannels are required. By programming electric signals, these operations can be performed on the same chip instead of manufacturing physical structures for a specific fluidic function. Furthermore, re-configurable digitalization allows microfluidics functions to be reduced to a set of fundamental operations thus enabling simpler controlling. Secondly, digital microfluidics allows independent control of many droplets simultaneously, thus enabling high speed (up to 25cm/s) and energy efficient transportation (nW to µW per transfer). Finally, consumption of reagents is decreased because there are virtually no dead volumes in digital microfluidics. [6; 8; 9]

Several different mechanisms, such as thermocapillary and surface acoustic wave (SAW) transport [8 and the references therein], electrophoretic, electrowetting and liquid dielectrohoresis, have been used to perform droplet manipulation operations. Especially platforms based on SAW can provide effectively several essential steps, such as mixing, merging and splitting droplets, required in fluent droplet manipulation [5].

Because the aim of this work is to design a system that uses optically induced electric fields for droplet manipulation, the most of these methods are beyond the scope of this thesis and are not discussed more deeply. Next, this work presents briefly the two most widely used electrical-field based droplet manipulation mechanisms in microfluidics, liquid dielectrophoresis (LDEP) and electrowetting.

LDEP has received remarkable interest in the last decade especially because of its rather easy implementation to digital microfluidics systems and good suitability for dispensing and manipulating as small as sub-nanometer droplets. The working principle of LDEP is resting on body forces of a droplet in an applied electric field and it is pertained with insulating fluids. When a non-uniform electric field is applied to an insulating droplet, it will polarize and begin to flow towards areas of the higher (positive dielectrophoresis, discussed more in Section 2.4) electric field strength intensity to minimize the applied electric field energy. [9; 10] In LDEP, as well in the electrowetting actuation mechanism that is closely related to LDEP, droplet transport is achieved by scanning an activation voltage along the electrode matrix ahead of the droplet. There are several publications, such as [9-12], demonstrating droplet creation and manipulation using LDEP. Detailed examination of the nature of the force distribution underlying in an LDEP-based system has been discussed for example in [13]. Furthermore, dielectrophoresis (DEP), the phenomenon behind LDEP-based system, is briefly presented in context with particle manipulation in Section 2.4. When comparing LDEP and electrowetting actuations, the main difference is that in latter the droplet is electrically conductive and the charge accumulates on the surface, thus reducing the contact angle of the droplet on one side and enabling droplet transportation. Because of this divergence between LDEP and electrowetting actuation mechanisms, LDEP requires higher frequency and higher actuation voltage, with typical used values being 50–200 kHz and 200–300 V (root-mean-square value, RMS), respectively, compared to values applied in electrowetting (DC or low-frequency AC voltage with amplitudes lower than 100 V) [15]. In LDEP, this might raise the problems with the electrical connection and heating of solution and therefore its use with different matrix of samples is narrower compared to electrowetting. [1]

Because the droplet manipulation part of this work concentrates on light actuated electrowetting named as optoelectrowetting, LDEP, even though it has been used successfully in various droplet manipulation experiments, will not be discussed in more detail in this thesis. Furthermore, because widely used, the term digital microfluidics is used to describe microfluidics systems where electric fields are used for droplet control from now on in this work. The physics of microliter droplets and electrowetting, the underlying working mechanism of optoelectrowetting, are presented before going to a deeper analysis of optoelectrowetting. The next section presents briefly the most relevant physical aspects of microliter droplets from electrowetting point of view.

2.1.2. The physics of microliter droplets [1]

In digital microfluidics, where a droplet is located on a solid surface, the interface between the droplet and the surrounding medium can be assumed smooth in macroscopic scope as shown in Figure 2.1a). In the macroscopic view, a three-phase contact line can be rather easily defined, where all the three interfaces (liquid-vapour, solid-vapour and solid-liquid), are located. The tangent to the surface at the contact point is defined as a contact angle and expressed with θ. However, when inspected the separation of immiscible fluids, such as water and air, in the microscopic view, the interface is not unambiguous anymore as is shown in Figure 2.1b). The reason is that at molecular level the separation depends on the Brownian diffusion and molecular interactions between the neighbor molecules of each fluid. For polar liquids such as water, these interactions are mostly hydrogen bonds whereas organic liquids experience Van der Waals attractive interactions. As can be seen in Figure 2.1c), molecules located at the interface have only the half of the interactions with neighboring (own) molecules than the molecules in the bulk.

The molecules at the surface are also contact with gas molecules. However, because gasses have lower densities than liquids, molecules located at the interface have a remarkably smaller number of neighbor molecules to interact with than molecules in bulk liquid, resulting dissymmetry in the interactions and thus deficiency of surface energy. At the macroscopic view, a quantity called surface tension has been presented to describe this molecular effect. It can be described following. If denoting the molecules' cohesive energy per molecule as W_c, at the interface an estimated energy loss of a molecule is $W_c/2$ (only half of the number of interactions). Also, if the characteristic molecular dimension is expressed as δ, δ^2 is associated with molecular surface and the approximation of the surface tension γ_{LV} (unit: N/m) between liquid-vapour (gas or liquid) interface can be written as [1]:

$$\gamma_{LV} \approx \frac{W_c}{2\delta^2} \tag{2-1}$$

Given as an example, for air-water interface γ_{LV} is ~0.072 N/m at the room temperature. Surface tension, being a force per unit length, will describe a force that is tangentially toward to the interface. As can be seen from the equation above, surface tension is larger with liquid having large cohesive energy and small molecular dimension, resulting that for example mercury has a larger surface tension than oil or water.

Based on the nature of energy minimization behaviour of any system, it can also be noticed that a fluid system tries to decrease surface areas to minimize the total energy of surface, which is the product of surface tension and interfacial surface area. The reason is that when the surface area is smaller, the smaller is the amount of molecules at the interface, resulting in smaller cohesive energy imbalance. If there would not be any

other forces, interfaces would tend to adopt a flat profile. However, because normally there always exists capillary constraint at the contact between the liquid and the solid, the droplet tends to take as a convex shape that is as close as possible to a sphere [1] when neglecting any droplet deformation right at the three-phase contact line. In this thesis this assumption is performed because the interest is in the macroscopic, or bulk, not in microscopic (or local) shape of the droplet.

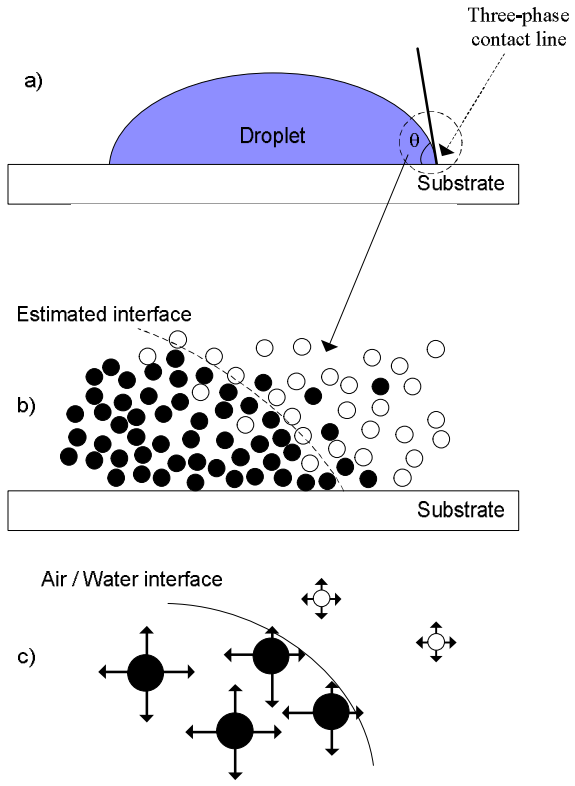

Figure 2.1: a) A macroscopic view of a droplet on a solid surface where θ presents the contact angle of the droplet and is the tangent to the surface at the three-phase contact line. b) An enlarged area of Figure 1a) showing the microscopic interface at the molecular level. c) A simplified illustration of molecules at vapour/liquid interface, where molecules have reduced amount of interactions [redrawn from 1].

As mentioned, surface tension is temperature dependent, resulting that when temperature increases, surface tension will decrease. The phenomenon called Marangoni convection, also called as thermocapillary instability, is the result of a local surface tension change. If a droplet is locally heated by any source like conduction or convection, there will be a gradient of the surface tension at the interface between the warmer and cooler locations. This imbalance creates a fluid motion from the warmer area towards the cooler area. The generated motion inside the droplet will have a huge impact on the behaviour of the droplet, for example increasing significantly the evaporation speed of the droplet.

The surface tension and the contact angle have a relation, which can be described by so-called Young's law at the three-phase contact line [1]:

$$\gamma_{LV}\cos\theta = \gamma_{SV} - \gamma_{SL} \tag{2-2}$$

where γ_{LV}, γ_{SV} and γ_{SL} are the surface tensions of liquid-vapour (gas or surrounding liquid medium), solid-vapour and solid-liquid, respectively, and θ is the contact angle. It should be remembered, that working with real biological fluids that are inhomogeneous and usually contaminate the solid wall by chemical molecules, leads to a change in the value of γ_{SL}, and thus change in the contact angle θ as described by Young's law. A micro-size droplet with the different surface tensions and the contact angle is shown in Figure 2.2 where it is assumed that the surface of the substrate is smooth. It also defines the contact radius r_c as the radius of the droplet area which is contacted to the surface. In this work, this area is expressed as a droplet contact area A_c. Furthermore, in this thesis expression hydrophobic is used to describe a surface where a droplet of any medium has a contact angle larger than 90°, generally termed as a non-wetting surface. On the other hand, a term hydrophilic surface is used when the contact angle is below 90°, generally expressed as a so-called wetting surface. The physics of a droplet on a non-smooth surface, such as textured micropillars structure, is slightly different. These so-called superhydrophobic surfaces having a very large initial contact angle (even over 160° [16]), have some advantages such as easier transportation compared to smooth surfaces, are not discussed in this study. Several publications [1; 16] provide more information about the properties of these microfabricated surfaces in electrowetting applications.

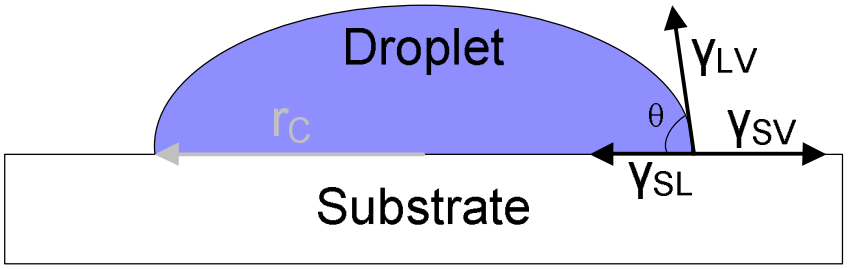

Figure 2.2: A schematic presentation of the force balance at the three-phase contact line and contact radius [redrawn from 1].

Next this thesis will go more deeply into the phenomenon of electrowetting. More detailed information about the physics of droplets, such as surface tension, Marangoni convection and Young's law can be found for example from [1] and [3].

2.2. Electrowetting

Surface tension and capillarity, by overcoming other forces like gravity or inertia that are remarkable in the macroscale, are the dominant forces in the microscale. For this reason, and because their implementation is rather simple, they are attractive driving methods for digital microfluidics applications. It was already discovered a well over hundred years ago [2] (for English translation see [3]), that the presence of electrical potential across a liquid-liquid interface can modify the surface tension of the liquid.

The principle of the reported effect, nowadays called as electrocapillarity effect, is described by the Lippman law, and is the basis of electrowetting-based digital microfluidics systems. In the electrowetting configuration, this law can be illustrated by modifying the equation given in [2]:

$$\gamma_{SL} = \gamma_{SL0} - \frac{1}{2} * C_s * U^2 \tag{2-3}$$

where γ_{SL0} and γ_{SL} are the solid-liquid surface tension when no voltage and after voltage U is applied, respectively, and C_s is the specific capacitance (capacitance per unit area) of an electrical double layer (EDL) for electrowetting (EW), or a dielectric layer for electrowetting on dielectrics (EWOD). The EW and EWOD, two different driving mechanisms of electrowetting, are presented later in this section.

2.2.1. Origins of electrowetting

The difference between electrocapillarity and electrowetting, which is the physics that describes the electric forces on the interfaces of conducting liquids and on three-phase contact lines [1], is that in the electrowetting the generated electric field changes the interfacial tension between the liquid and the solid electrode, not between liquid and liquid as in electrocapillarity. In electrowetting, the applied electric forces are used to modify the apparent capillarity of the droplet. This can be understood as a charge-induced change in the interfacial energy between the droplet and the solid, resulting a change in surface tension that is then detected by the (macroscopic) change in the contact angle of the droplet. [1; 16] There are at least three approaches to obtain the dependency between the contact angle and the applied voltage. The derivation of the given Lippman law can be performed using the classical thermodynamic [1-3], the energy minimization [17; 18] or the electromechanical approaches [15; 19], which all are extensive reviewed in [3].

The validity of the used theory depends on the scale of interest. In this thesis, where the main interest is on the macroscopic contact angle, the energy minimization approach is used. This approach, together with the classical thermodynamic approach, addresses only the static contact angle problems and therefore, it does not give any insight how electric forces are really acting on the droplet in mechanical terms. It still can be considered valid as long as the inspection is restricted to system specific limits, such as

saturation and hysteresis, phenomena that are later discussed. Furthermore, it is has been shown that functional electrowetting devices can be developed using only static assumptions [20]. For a dynamic problem, where viscous effects should be included to specify exactly the forces created by the applied electric field on the interface, the electromechanical approach [15, 19] has been proposed. However, it can be concluded that there are currently inadequate amount of theory that could predict the dynamic behaviour of the droplet; neither the creation of flow patterns inside the droplet nor the translational motion of the droplet are sufficiently understood [1].

2.2.2. The energy minimization approach to electrowetting

In the energy minimization approach, the energy of the droplet is assumed to be dependent on the geometry of the droplet (the contact angle and the contact radius of the droplet) and system parameters. In this approach, the system assumes that the droplet achieves it equilibrium shape when the energy is minimized. The approach views the electrowetting effect as a change (reduction) in solid-liquid surface tension γ_{SL} as a result of the appearance of electric charges in the EDL (EW) or at the dielectric surface (EWOD). The present contact angle of the droplet is a result of a competition between dielectric and surface tension energies. The dielectric energies are trying to enlarge the solid-liquid area to decrease the charge concentration whereas the goal of surface tension energies is to minimize the free surface of the droplet. [1] When voltage is applied, the capacitive energy will be stored in the dielectric layer, increasing dielectric energies, thus reducing the corresponding interfacial energy. Therefore, the wetting of the droplet is enhanced.

As it was mentioned earlier, presented approach simplifies the real situation but can be used to calculate static changes when voltage is kept within certain limits. The dependency between the applied voltage U and a new contact angle θ can be calculated by the combined Young-Lippmann equation proposed by [17]:

$$\cos\theta = \cos\theta_0 + \frac{C}{2\gamma_{LV}A}U^2 = \cos\theta_0 + \frac{\varepsilon_0\varepsilon_d}{2d\gamma_{LV}}U^2 \tag{2-4}$$

where θ_0 is the initial contact angle of the droplet without electric field, C is the capacitance of the insulator layer with the area A, ε_0 and ε_d are the permittivity of the vacuum and the relative permittivity of the dielectric layer (EDL in EW, insulator layer in EWOD) with the thickness d, and γ_{LV} is the liquid-vapour interfacial tension. The latter is usually assumed to be constant [3]. In EWOD-systems, where capacitances of the EDL and the insulator layer can be modelled as in series, the first one is usually ignored from the analysis. This is because of the contribution of the EDL to the total capacitance of the layers is typically small [1]. As it can be seen from the equation, the contact angle θ decreases when voltage is increased. This has experimentally been confirmed to hold as long as the applied voltage is kept between certain higher and

lower threshold values, resulting from the contact angle hysteresis and saturation, respectively, phenomena which are discussed later in this thesis.

The Young-Lippman equation states that if a thinner insulator layer using higher dielectric materials is implemented, lower voltage is required to obtain similar contact angle change if other parameters are kept constant. It should be noticed that for practical EWOD-systems this thinning of the insulator layer cannot be performed beyond the dielectric breakdown of the material (see Section 2.2.7). It can be concluded that as long as the applied electric fields are not exceeding dielectric breakdown of the dielectric layer, the operation range of EWOD-system is between applied voltages U_{max} and U_{min}, which are defined by the contact angle saturation and hysteresis, respectively. These phenomena are presented in Section 2.2.5 and in Section 2.2.6, respectively.

2.2.3. Electrowetting (EW) and electrowetting on dielectrics (EWOD)

As mentioned before, electrowetting-based driving methods can be separated to two mechanisms: direct electrowetting (EW) where a liquid droplet is in direct contact with electrodes, and nowadays more common electrowetting on dielectrics (EWOD, sometimes abbreviated with EWD). In EWOD, a mechanism first proposed in [17], a thin insulator layer is separating a droplet and bottom electrodes. Because of the thickness of the EDL is typically only 1-10 nm [21], EW, where charges are stored between the liquid and the electrode, requires lower driving voltages than EWOD. This is because the EDL has higher value of capacitance than the insulator layer in EWOD. This would make EW more suitable especially for portable applications. However, it has some disadvantages limiting its use in digital microfluidics applications. Since the droplet is directly contacted with the electrode and the EDL cannot stand high voltages, the voltage must be kept low to avoid electrolysis and other undesired electrochemical reactions and thus generation of gas bubbles. This means that, if consider a typical water droplet as an example, the maximum possible voltage difference is only around 0.1V [1]. Therefore, the achievable contact angle changes in EW devices are usually very low. Furthermore, it is rather difficult to return the electrowetting process to an original state when the electrode is once wetted. There is an insufficient reversible control possibility of the droplet in EW-based systems, degrading robustness of the systems [21]. On the other hand, EWOD, which is more common nowadays, is having electrochemical inertness and reversible electrowetting possibility with a suitable insulating layer.

The schematics of EW and EWOD systems are shown in Figure 2.3 [22]. Because of the problems presented above, and that optoelectrowetting, the scope of this work, requires an insulator layer to work properly, this thesis will focus on EWOD-based systems.

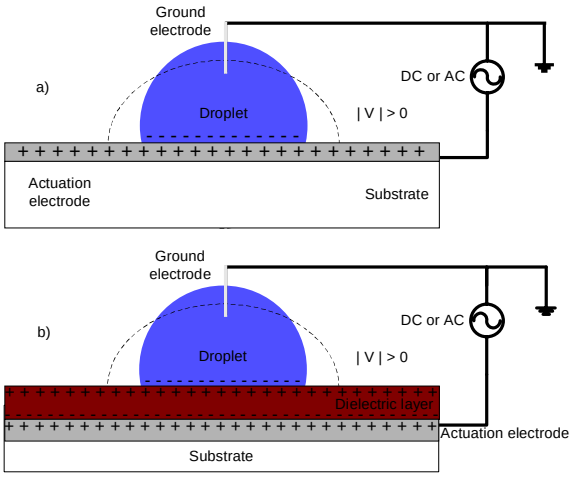

Figure 2.3: The principle of a) EW, and b) EWOD. In EW, charges are distributed at the interface of the electrode and the droplet, whereas in EWOD charges are accumulated at each interfaces [redrawn from 22].

Drawback of EWOD-systems compared to direct EW-systems is that they require typically higher minimum voltage to work [21]. Fortunately, this minimum voltage can be lowered to 20 V or even less using a thin and high permittivity hydrophobic insulating layer such as DuPont™ Teflon® [23] or other amorphous fluoropolymer (aFP) together with silicon dioxide. [22, 24-26] Another approach to minimize the required voltage is to replace air as a driving medium by silicone oil or covering the surface by oil and then drying it, thus leaving a thin oil layer between the droplet and the solid. [24]

2.2.4. Droplet motion with different EWOD set-ups

As discussed earlier, the contact angle of the droplet can controlled by exposing the droplet to external electric field. To enable fluid motion, the electric potential has to apply to only one end of the droplet to decrease locally the solid-liquid interfacial tension, thus reducing the local contact and turning the surface of this area from hydrophobic to hydrophilic. Two opposite sides of the droplet are on top of actuated and non-actuated electrodes, and asymmetry liquid shape is deformed. This generates a pressure difference inside the droplet towards the lower tension, creating forces, which are parallel to the surface, towards the interface that is electrically actuated. If these forces are large enough to overcome hysteresis (see Section 2.2.6), the droplet will move towards the hydrophilic region. [1] When applying sequentially voltage to electrodes, discrete droplets can be transported. [3] As shown in Figure 2.4**,** the droplet edges have to overlap at least two adjacent electrodes (actuation electrode and non-actuating or ground electrode) to enable droplet actuation. Therefore, the size of two electrodes (typically in the order of 800 to 1000 µm) will define the smallest volume of liquid that can be transported. If the height of the spacer between bottom and top electrodes is in the usual range of 100–500 µm, the minimum droplet that can be

manipulated is 0.1 to 1 µl. [3] However, this is a simplified model for the real motion of the droplet. It should noticed that microfabrication lithography techniques typically restrict the gap separating two neighboring electrodes to the order of 10 to 30 µm [1]. There will be always a hydrophobic region between electrodes because of this gap. If the shape of the electrodes is square, the droplet can sometimes undesirably stop between two electrodes as a result of the symmetric conditions on the both side of the droplet and the hydrophobic gap. Increasing the reliability of EWOD-actuation thus preventing unwanted sticking of the droplet between electrodes can be performed by redesigning the shape of the electrodes edges as a zigzag [27] or a comb [28].

Two typical EWOD configurations are presented next. In two-plate, or closed, set-ups the ground electrode is placed on the top of the liquid so that the droplet will be sandwiched between the electrodes as shown in Figure 2.4a). Usually the top electrode is covered with a thin hydrophobic layer, such as fluoropolymer Teflon®, to a enable large contact angle and a small contact angle hysteresis. Without any applied voltage, the contact of the droplet is hydrophobic with both plates. When there is an electric actuation on the rightmost electrode, a local decrease in the interfacial surface tension results in a contact angle reduction on the right side of the droplet, thus creating a pressure difference between the left and right side of the droplet. The droplet will be moved towards the activated electrode. [3] In closed systems, the vertical gap is typically remarkably smaller than the horizontal dimension of the droplet, resulting that the liquid–medium (air or oil) interface is smaller than solid–liquid interface. This means that the energy of this liquid–medium interface is significantly smaller than the solid–liquid interface, and the droplet will deform to the shape of the underlying electrode, such as square. [1] In single, sometimes called also open, systems the ground electrode is located next to the actuation electrodes on the same plate as shown in Figure 2.4b). [7]

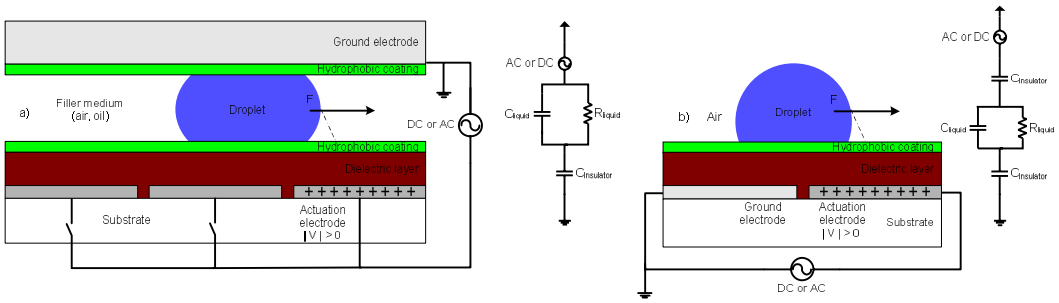

Figure 2.4: A schematic diagram of two typical EWOD set-ups (not in scale) and their equivalent circuits. a) A two-plate set-up where a droplet is moved rightwards by activating the rightmost electrode [Redrawn from 3]. b) A single-plate set-up where the ground electrode is next to actuation electrodes on the same plate, inducing droplet spreading onto the two adjacent electrodes [redrawn from 7].

The two-plate systems have some disadvantages compared to the single-plate systems. Because the droplet has to touch the top and the bottom electrodes in the

manipulation chamber, the range of droplet sizes that can be generated are limited to certain volumes as a given footprint. Single-plate devices also provide easier handling and interfacing with external devices, and better opportunities for optical detection. Furthermore, various different geometries of ground wires and electrodes can be used [29]. However, two-plate devices are, as being closed systems, used in the applications where droplets would otherwise evaporate too fast. Furthermore, as will be discussed in Section 2.2.9, various fundamental operations, such as creating (dispensing) droplets from a larger reservoir, are difficult or even impossible with open systems. [1] In the next two sections, this thesis will study deeply phenomena which are limiting the use of practical EWOD-devices. Based on the limits of EWOD-device, the discussion on the achievable forces in EWOD-systems are considered in Section 2.2.8

2.2.5. Contact angle saturation

The Young-Lippmann equation predicts complete wetting, meaning that the contact angle of the droplet would go to zero if large enough electrical potential would be applied. However, above a certain threshold value, the electrocapillary force affecting the droplet does not increase any more, the change in the contact angle saturates and thus is not anymore dependent of the electrical potential. So the desirable complete wetting is not able to achieve experimentally since this wetting enhancement will not continue at a certain contact angle limit**.** This phenomenon, called as electrowetting saturation, is one of the main challenges in DMF based applications and has been under intensive inspection in last years. [3] The illustration of the contact angle saturation can be seen in Figure 2.5, where theoretical values calculated by the Young-Lippmann equation using given parameters and measured values from [30] are compared. As can be seen, the contact angle is saturated to around 80°, which is the minimum reachable contact angle in this specific set-up.

The origin of contact angle saturation is not fully understood, and comprehensive clarification of its cause or causes are still missing. Some of the proposed explanations are shortly presented here. Extensive review about suggested reasons for contact angle saturation can be found for example in [1] and [3].

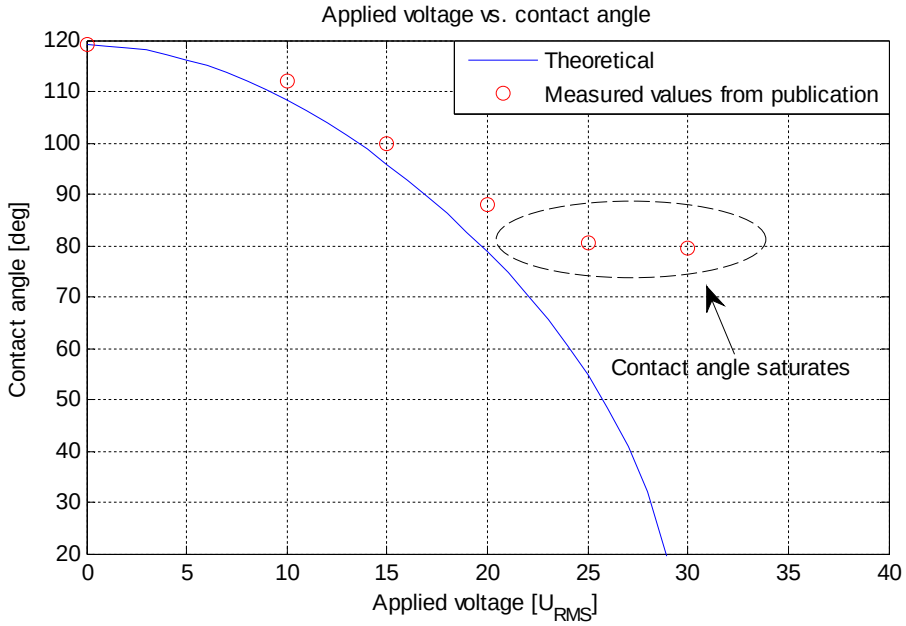

Figure 2.5: Contact angle saturation is shown when compared theoretical and measured contact angles with applied voltage. Dielectric layer consists of 100 nm silicon dioxide (SiO2)-layer coated with 20-nm-thick Teflon®-layer [redrawn from 30].

Verheijen and Prins [31] noticed that saturation was in correlation with the injection of charge carriers into the insulators. The existence of trapped charge across the solid-liquid interface can reduce the electric field at this interface, thus lowering generated electrowetting force. This idea was agreed in [16] and recently [32] and it has achieved popularity, probably because of its simplicity. Anyhow, not everyone has agreed this explanation. For example, Vallet *et al.* [33] assumed that the saturation is the result of ionization of the gas (usually air) near the three-phase contact line. During ionization, charge would begin to leakage through the surrounding gas, leading to saturation of the contact angle. In the same publication, the authors also suggested that the instability of the three-phase contact line could be the origin of saturation. In [18], Shapiro *et al.* considered the non-ideal insulating properties of the dielectric layer. Because of these non-ideal properties, the insulator changes locally to a conductor. In consequence, a major potential drop is shifted from the insulator layer to the droplet, leading to the saturated contact angle. Furthermore, Shapiro *et al.* also proposed another approach. Instead of assuming a perfectly conductive droplet as in the Young-Lippman equation, presenting a small electric resistance dependent of the droplet shape could explain the saturation. The resistance of the droplet is increased when it spreads on the solid, so saturation can be illustrated as a geometrical effect. The drawback of this approach is that the model is highly sensitive to the ratio of the used resistivities, which are difficult to measure precisely. Peykov *et al.* [34] have proposed a so-called the PQRS model, which is known as the zero interfacial tension criterion where saturation is based on the thermodynamic limit of stability. The effective solid-liquid interfacial tension γ_{SL}

decreases as the applied voltage is increased. This tension cannot be negative, so the limiting value of it is zero. When increasing the applied voltage, at point when this tension is vanished, the contact angle saturation is also observed. The problem of this approach is that it needs the information about the solid-vapor surface tension γ_{SV} that might be difficult to specify. However, for Teflon® and other apolar materials used in EWOD, wetting surface tension can be used as a reasonable value of γ_{SV}. The model has usually predicted the experimental value in a good agreement but it is still argued could a negative surface free energy exist. Anyhow, this model is suitable to be used to define maximum actuation voltage, as will be discussed in Section 2.2.8. [1]

2.2.6. Contact angle hysteresis

For microscale drops, capillary hysteresis arises from physical reasons such as surface roughness and defects. It reduces the capillary force of the droplet and can be defined as the deviation of the real contact angle from its theoretical value. Dynamic hysteresis occurs during dynamic motion of an interface. It can be observed when measuring the contact angle of the droplet while increasing and decreasing the applied voltage. There is a difference between advancing (the droplet spreading on the surface when the voltage is increased) and receding (the droplet returning to the original shape) contact angles, leading to a contact angle curve, which is following different path when returning back to the initial stage. The hysteresis is defined as this difference and, based on the experiments, is the result of effects at the solid-liquid interface. [1] Because the surface roughness, heterogeneous chemical composition, or other inhomogeneous conditions of the surface can affect receding and advancing contact angles, the hysteresis can also viewed as the indicator of the quality of the solid surface [31]. Figure 2.6 shows a draft of a contact angle hysteresis curve and experimentally measured contact angle hysteresis with de-ionized (DI) water. In the latter case, hysteresis α is relative low (in degrees around two) because the droplet is immersed in silicone oil. Typically, hysteresis values of DI water on hydrophobic Teflon® surface are ranging from 7-9° when the droplet is surrounded by air [1].

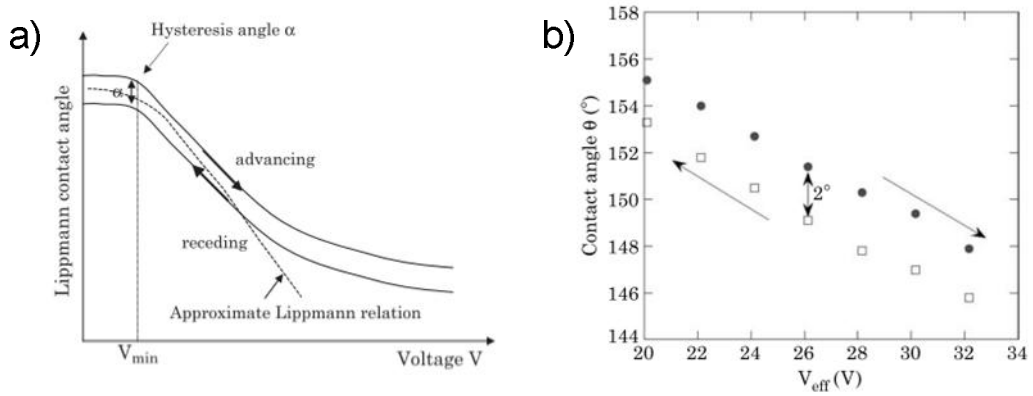

Figure 2.6: a) A sketch of the contact angle hysteresis curve, b) experimentally measured contact angle hysteresis α of DI water droplet located on top of Carbon doped silicon oxide (SiOC) surface, and immersed in silicone oil [1].

In practical EWOD devices, the contact angle hysteresis defines also the minimum level of voltage required for the droplet motion. Experiments have shown that the droplet does not move below this system-specific electrical potential threshold voltage U_{min}. Without hysteresis, this voltage would go to zero and the droplet could move even though applying an infinitely small voltage. [1] It has been also observed that when the liquid droplet is immersed into an oil (usually silicone) environment instead of air, lower actuation voltage was required, leading to the improvement in the transportation of the droplet. [31] It can be concluded that the manipulation of the droplet in air instead of immiscible liquid is more challenging, because the droplet will have lower initial contact angle and higher hysteresis. As will be discussed in more detail in Section 2.2.10, when manipulating physiological fluids such as blood or urine, a thin film of oil will also significantly reduce unspecific adsorption of molecules onto the bottom layer. Furthermore, another issue affecting the hysteresis and saturation is the type of voltage that is used. It has been shown that applying low frequency (typically around kilohertz or less) AC voltage instead of DC, hysteresis is decreased and saturation point is delayed [35, 36], probably because of random pinning forces are reduced [37].

2.2.7. Dielectric breakdown

Insulator, or dielectric, layer will disrupt when exposed to high enough electric field. The threshold value is an intrinsic property of bulk material, and it is called as the critical electric field, usually denoted as E_{DB}. This limit can be also defined as the (theoretical) dielectric strength of a material. For perfect Teflon® material, the theoretical dielectric strength is 59 MV/m (or V/µm) [1]. Without going in details, during dielectric breakdown (DB) the induced electric field over the insulator layer is so high that it is sufficient to free bound electrons inside the material. The result is that an electrically conductive path and a damaging discharge are generated through the material, thus deteriorating or even breaking the insulating capability of the material. [1]

Breakdown voltage is the maximum voltage that certain material can withstand without breaking. For perfect dielectric materials with thickness *d*, this dielectric breakdown voltage U_{DB} can be defined by [3]:

$$U_{DB} = E_{DB} * d \tag{2-5}$$

However, when using real materials, this procedure has some limitations that usually degrade the limit the maximum voltage to lower values than U_{DB}. Firstly, the value of critical electric field is dependent not only on the material, but also the structure of the material; bulk material has typically higher value than thin layers. Secondly, it is possible that the electric fields are exceeding breakdown voltage locally near the three-phase contact line, thus breaking the layer even though U_{DB} would not have reached the limit. [3] Thirdly, electric fields might be locally too high when the substrate is not totally homogenous or there are some adhesion, such as protein or cells, on the substrate. [1] In conclusion, thickness and dielectric strength of the insulator layer must be considered when designing EWOD-device. To keep the device in full-scale action, dielectric breakdown voltage should be higher than the contact angle saturation voltage.

2.2.8. Forces in EWOD-devices [1]

This section considers possible EWOD-forces that can be created. Because there has not been a full consensus on the physics of droplet motion under electrowetting actuation [1], this thesis will only summarize the main points about generated forces. This section defines the voltage and force ranges of EWOD-devices.

Using the Young-Lippmann law [17] presented earlier, the electrical potential *U* can be written in the form:

$$U = \sqrt{\frac{2d\gamma_{LV}}{\varepsilon_0 \varepsilon_d} * (\cos\theta - \cos\theta_0)} \tag{2-6}$$

It has been assumed that the saturation voltage is below the voltage required for dielectric breakdown of the insulator layer in the presented equation. This means, that the minimum and maximum working voltages in practical EWOD-devices are based on contact angle hysteresis and saturation as discussed earlier. The first one will define the minimum voltage required to move the droplet, and will mainly depend on the nature of the droplet and the surface. The latter one gives the upper limit for voltage that can be used. Above this limit the electrocapillary force does not enhance anymore even though voltage is increased, thus it defines the limit where the Young-Lippman law does not hold anymore.

The minimum voltage that is required for droplet motion can be defined from the Young-Lippman law. If considered the linear part of this law, by applying the voltage U to the electrode with width d_e, the so-called "Lippman" force can be expressed [1]:

$$F_{EWOD} = \frac{d_e * C_s}{2} * U^2 \tag{2-7}$$

where C_s is presenting the specific capacitance [F/m^2] defined by $\varepsilon_0 * \varepsilon_d$ / d. Then the criterion of the drop displacement based on the total capillary force can be given by [1]:

$$\begin{aligned} &\frac{d_e * C_s}{2} * U^2 - d_e * \gamma_{LV} \alpha * \left[\cos\theta(U) + \sin\theta(U) - \cos\theta_0 + \sin\theta_0\right] > 0 \\ &\Rightarrow U_{\min}{}^2 = \frac{2 * \gamma_{LV}}{C_s} \alpha * \left[\cos\theta(U_{\min}) + \sin\theta(U_{\min}) - \cos\theta_0 + \sin\theta_0\right] \end{aligned} \tag{2-8}$$

where U_{min}, γ_{LV}, α, θ and θ_0 are the required minimum voltage, the liquid-vapor surface tension, the contact angle hysteresis, the new contact angle under the applied voltage U_{min} and the initial contact angle, respectively. This equation can be simplified by using the Young-Lippman law (2-4), and assuming that U_{min} and α are sufficient small [1]:

$$\begin{aligned} &\frac{C_s}{2\gamma_{LV}} * U_{\min}{}^2 = \frac{\alpha}{1-\alpha}\left[\sin\theta(U_{\min}) + \sin\theta_0\right] \\ &\Rightarrow U_{\min} \approx 2\sqrt{\frac{\alpha * \gamma_{LV} * \sin\theta_0}{C_s}} \end{aligned} \tag{2-9}$$

From the presented equations, it can be noticed that for minimal voltage requirement, as small contact angle hysteresis as possible, a very hydrophobic top layer, and a large capacitance value are the desired properties. The latter is depending on the thickness and permittivity of the material, so a material with a large critical electric field or a thin layer would be desirable. However, there are two limits for using thinner material that should be considered, a practical limit for production, and a dielectric breakdown limit. [1]

As long as dielectric breakdown voltage is not exceeded, the maximum actuation voltage is defined by saturation voltage $U_{max} = U_{sat}$. As discussed previously, there are several proposed reasons for this phenomenon. If using the PQRS model [34] mentioned earlier, this thermodynamic approach defines that when saturation voltage is applied, the effective solid-liquid surface tension γ_{SL_eff} decreases to zero [1]:

$$\gamma_{SL\_eff}(U_{sat}) = \gamma_{SL\_eff}(U_{\max}) = \gamma_{SL} - \frac{C_s * U^2}{2} = 0 \tag{2-10}$$

When γ_{SL_eff} goes to zero, the saturated contact angle is only dependent on the solid-vapour γ_{SV} and the liquid-vapour γ_{LV} surface tensions and Young's law at the saturation can now be presented [34]:

$$\cos\theta_{sat} = \frac{\gamma_{SV} - \gamma_{SL\_eff}(U_{sat})}{\gamma_{LV}} = \frac{\gamma_{SV} - 0}{\gamma_{LV}} = \frac{\gamma_{SV}}{\gamma_{LV}}$$
$$\Rightarrow \gamma_{SV} = \gamma_{LV} * \cos\theta_{sat} \quad (2\text{-}11)$$

From Equation (2-11), assuming that $cos\theta_{sat}$ equals to $cos\ \theta(U_{sat})$, the maximum voltage limit can be defined using the initial solid-liquid surface tension γ_{SL0} [1]:

$$U_{\max} = U_{sat} = \sqrt{\frac{2*\gamma_{SL0}}{C_s}} = \sqrt{\frac{2*(\gamma_{SV} - \gamma_{LV}\cos\theta_0)}{C_s}} = \sqrt{\frac{2*\gamma_{LV}(\cos\theta_{sat} - \cos\theta_0)}{C_s}} \quad (2\text{-}12)$$

Equation (2-12) ignores the fringe effect, which can be understand as the enhance of the electric field near the three-phase line because of discontinuity of material properties at that point. [1] However, it is valid to the neglect fringe effects as long as dealing with sufficiently large droplets because the fringe effects are mainly localized closely around the contact line [3]. If it is desired to operate until the saturation voltage limit, and considering the dielectric breakdown of the dielectric layer so that $U_{max} = U_{sat} = U_{DB}$ it is possible to define the required minimum thickness of the insulator by combining Equation (2-5) and Equation (2-12) and remembering that $C_s = \varepsilon_0 * \varepsilon_d / d$ [1]:

$$d_{\min} = \frac{2 * y_{SL0}}{\varepsilon_0 * \varepsilon_d * E_{DB}^{\ 2}} \quad (2\text{-}13)$$

As can be noticed from Equation (2-13), if the goal is to reduce the thickness of dielectric, it is crucial that material has a large (theoretical) critical electric field E_{DB}. Figure 2.7 illustrates this situation with two different insulator materials, Teflon® and paraffin (material properties from [1]), when the contact angle is changing from 119° to ~80°, measured data from [30] as was illustrated in Figure 2.5. Voltage required for this contact angle change with different Teflon® thicknesses is calculated using Equation (2-12) with values following values: $cos\theta_{sat}$ = 80°, $cos\theta_0$ = 119°, γ_{LV} = 0.072 N/m and ε_d = 1.9 for Teflon®. It shows the required minimum thickness of the insulator layer to enable successful EWOD actuation. If the thickness of the dielectric layer is below this material specific limit d_{min}, the required EWOD actuation cannot achieved because of dielectric breakdown. It can be noticed, that with paraffin having a significantly lower dielectric strength than Teflon® [1], a considerable thicker insulator is needed to reach a desired EWOD-actuation. For Teflon® with thickness d_{min}, the minimum actuation voltage to achieve full EWOD-actuation is when $U_{sat} = U_{DB}$ as shown in Figure 2.7.

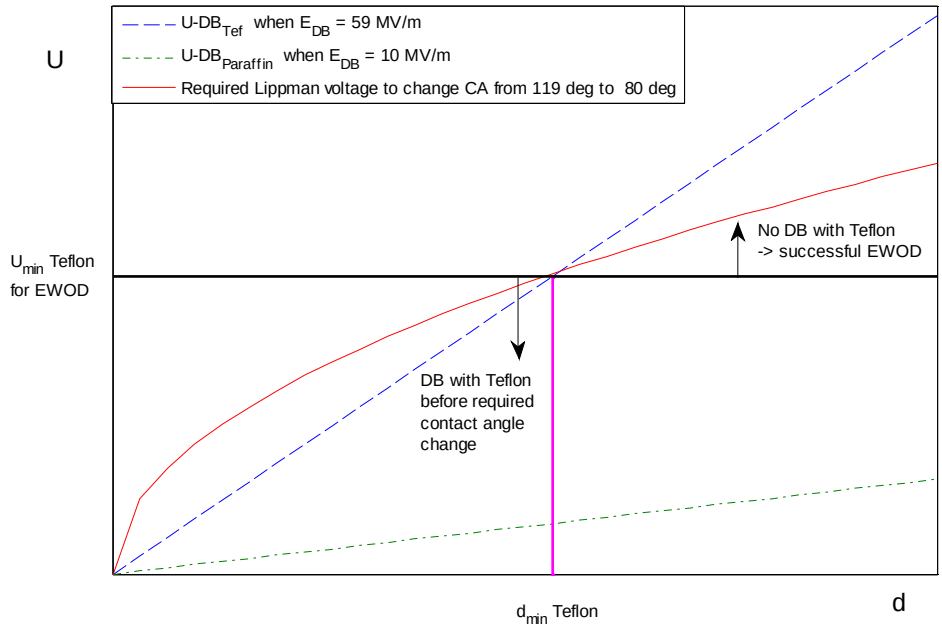

Figure 2.7: Minimum required thickness of the insulator layer to obtain particular contact angle change (values from [30], see Figure 2.5). As it can be seen, with material having lower dielectric strength (for exampleparaffin), desired EWOD actuation is not possible without very thick insulation layer [redrawn from 22].

When considering the EWOD device, the goal is to have a system that has as low minimum electrowetting force f_{min} required for droplet manipulation as possible, and that it could provide as large as possible electrowetting force f_{max}. The range of electrowetting-induced forces can now be defined based on the actuation voltage ranges described earlier. When motion of the droplet is started, electrowetting force is created between an actuated and a non-actuated electrode. Created electrowetting line force density on a three-phase contact line can be deduced from Equations (2-3) and (2-4) [1]:

$$F_{EWOD} = \frac{1}{2} * C_s * U^2 = \gamma_{LV} * (\cos\theta - \cos\theta_0) \qquad (2\text{-}14)$$

Based on the interval $[U_{min}, U_{max}]$, the range of electrowetting force is between F_{min} and F_{max} [1]:

$$F_{\min} = \frac{\alpha}{1-\alpha} * \gamma * \left[\sin\theta(U_{\min}) + \sin\theta_0\right] < F_{EWOD} < \gamma_{LV}(\cos\theta_{sat} - \cos\theta_0) = F_{\max} \qquad (2\text{-}15)$$

If assuming hysteresis angle α as small enough, minimum force can be approximated using equation [1]:

$$F_{\min} \approx 2\alpha\gamma_{LV}\sin\theta_0 \tag{2-16}$$

On the other hand, without dielectric breakdown the maximum actuation force based on saturation is $F_{max\_sat} \sim \gamma_{SL0}$. When considerer electrowetting force in Equation (2-14) at dielectric breakdown voltage U_{DB}, marked as F_{EWOD_DB}, the maximum force is then the minimum between these two forces [1]:

$$F_{\max} \approx \min\left\{F_{EWOD\_DB}, F_{\max\_sat}\right\} = \min\left\{\frac{\varepsilon_0\varepsilon_d * d * E_{DB}{}^2}{2}, \gamma_{SL0}\right\} \tag{2-17}$$

Giving an example of a standard force range with the typical specific capacitance C $(\varepsilon_0*\varepsilon_d / d)$ value of ~0.03 mF/m^2, the minimum electro-capillary forces are in the range of 1-20 µN compared to maximum forces of 15-40 µN [1].

2.2.9. Fundamental droplet manipulation operations in EWOD-devices

In this section, fundamental fluidic operations that are required in many possible EWOD-based applications, such as Lab-On-a-Chip (LOC) [5; 8], are shortly presented. These include droplet creation from a reservoir, transportation of the droplet, cutting the droplet into two and merging two droplets. Furthermore, the principle of advanced droplet mixing operation is illustrated. For more information, such papers as [1; 30] are good starting points.

Droplet dispensing from a larger reservoir is a crucial step towards LOC-applications. If the droplet can be created from an on-chip reservoir, the use of a spotting robot or a mechanical pump can be avoided. [1] For droplet creation, activation of at least three electrodes is required, as shown in Figure 2.8. First, two electrodes next to a reservoir electrode are activated, so that the liquid can flow from the reservoir. Cutting is then performed by deactivating the middle electrode and turning the reservoir electrode on, so that the droplet will be pulled on both ends and it will be cut [38]. In this set-up, the reservoir electrode was larger than other electrodes. Instead of commonly used DI water, the authors in [38] were also able to transport various human physiological fluids, such as saliva and urine when immersed in silicone oil. It was discovered, that moving of such a fluids as serum and whole blood containing more protein, was more challenging than fluids having less protein. Cho *et al.* [30] noticed, that cutting can be difficult, resulting that the liquid is stretched and unpredictable separation is observed. To solve this problem, they used two side electrodes located next to the main fluid route to improve the pulling of the liquid. Both dispensing experiments were performed using two-plate systems. It has been observed, that droplet dispensing in an open (a single plate) EWOD-system is impossible for the commonly used fluids, such as aqueous solutions and biological buffers [1].

Dividing a droplet into two is similar process than droplet creation. Here it is required, that the droplet is lying over at least three electrodes. The size of three electrodes will also define the minimum size of the droplet that can be used to perform all the fundamental operations. [3] The cutting operation is performed by activating both end electrodes and kept the middle electrode non-actuated at the same time. Now, while the droplet will elongate in the longitudinal direction, it will pinch in the middle, and eventually will be cut in two. [30] For a circular droplet in a single-plate system, the cutting is very difficult task for most of the liquids. For covered systems, cutting can be completed quite easily as long as the vertical gap (the distance between the bottom and the top electrodes) is sufficiently small. This is the reason why some open-systems include a closed-system area, where cutting and droplet creation can be performed. [1]

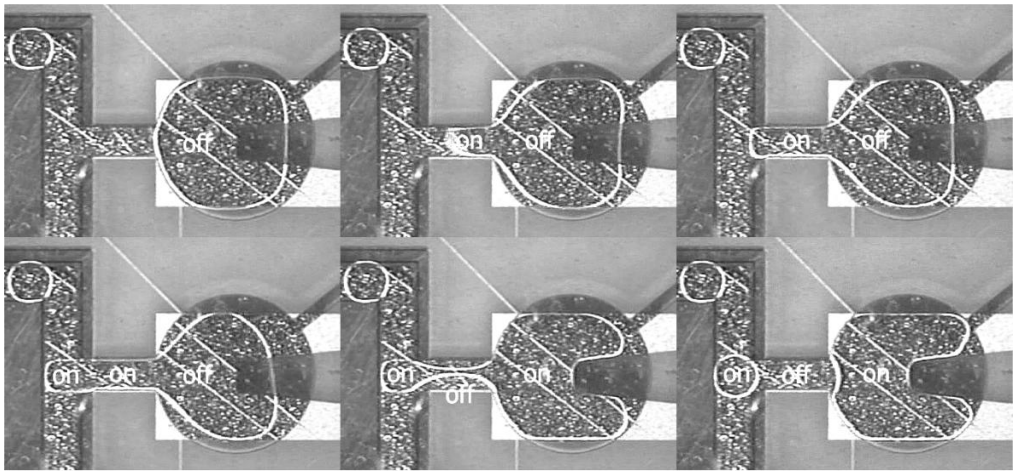

Figure 2.8: Droplet creation from a reservoir, where minimum of three electrodes is required to dispense a droplet [38].

The concept of droplet transportation has been already presented in Section 2.2.4. The maximum achievable speed is depending on many parameters, such as used liquid and droplet volume, applied voltage (amplitude, frequency), the value of gap, filler medium (usually air or silicone oil) and quality (smoothness) and thickness of insulator layer. [1; 3; 30] Maximum speeds that have been reported vary from 150 mm/s [1] to 250 mm/s (150 V) [38] with covered system and around 100 mm/s with open systems [1]. However, as mentioned, these speeds are heavily depending on the system parameters.

Merging of two (or more) droplets is quite straightforward operation. Basically only transporting two droplets towards the same electrode from opposite direction is required. For a larger droplet, also more than one electrode can be used. Merging of the droplet is essential step for droplet mixing, which is a complicated process because of the presence of the laminar flow in microscale droplets. After two droplets are merged, their contents are not quickly mixed together and the liquid is not homogenous. Fluid being in a laminar state, and without any active mixing, the mixing process would be only diffusion based which is too slow for many applications. There are at least three

different processes that have been used to enhance the mixing of the droplets. One option is to move the droplet back and fort. However, for many applications this approach is not sufficient enough, thus other operations have been tried. Even though continuously separating and merging the droplet has shown somehow performing better mixing, it has a drawback a slow process because of many cycles are required. The third mixing process, which have been observed to lead to remarkably better results is to move the droplet in a square loop. The efficiency of this approach is based on that in the square loop motion the bulk liquid will experience stretching-folding pattern at each corner, thus enabling faster mixing. Also the viscosity of the liquid is affecting the mixing efficiency. It has been noticed that mixing of highly viscous fluids, like ionic liquids is more challenging than aqueous droplets having small dynamic viscosity. [1, 30]

To summarize this section, there are several parameters that should be considered when designing an EWOD-actuator. The first one, the threshold voltage is very crucial. It is based on the contact angle hysteresis and defines the minimum required voltage for droplet actuation. Secondly, to implement basic fundamental operations, voltages needed for droplet cutting and creation from an on-chip reservoir are crucial. Times required to mix two droplets is important for many analysis. Another issue that is vital to know is the flow rate of the system. In EWOD-system, this depends on the volume and speed of the individually manipulated droplet, and the number of droplets that can be manipulated parallel at the same time. The electrodynamics of the all the operations presented here are not yet fully known, so numerical simulations could be use to understand better how the liquid properties and electrode shapes are really affecting the droplet motion. Furthermore, simulation could be used to optimize actuation voltage and frequency in EWOD-systems.

2.2.10. Practical aspects of EWOD-devices

In this section, some practical aspects of EWOD-devices are discussed. Many of the problems encountered are related to the layer properties (insulator layer or hydrophobic coating). Problems arising from the contact angle hysteresis, saturation and dielectric breakdown have been discussed earlier. For example hysteresis can be reduced by hydrophobic coatings or immersing the droplet in silicone oil. [38] These problems can be limited by a careful choice of the used insulating material. When designing an EWOD-system, it is crucial to optimize the insulator so that droplet actuation requirements are minimized. At the same time, the surface should be chemically inert and stable, providing a large initial contact for the droplet, be as thin as a possible and have a capability to withstand high electric fields. It can easily noticed, that there will always be a trade-off between these electrical, mechanical and chemical properties of the dielectric material. Given as an example, a thinner insulator layer is desirable to increase the specific capacitance and facilitating droplet actuation. On the other hand, this might lead that dielectric breakdown voltage drops below the saturation voltage thus decreasing the performance and reliability of the system. [3]

The most common way for this far to achieve the desired EWOD-actuation has been to coat a thicker insulator layer (typically for example silicon dioxide (SiO_2), silicon nitride (Si_3N_4) or Parylene C) having a high dielectric strength with hydrophobic material, such as Teflon®. Teflon® has been widely used because it, while providing the hydrophobic surface for most of the liquids, can also be prepared to very smooth, leading to small contact angle hysteresis (less than ten degrees for water droplet surrounded by air) and is resistive to bases and acids, thus having chemical inertness. [3] Using a protocol method developed by Seyrat and Hayes [39], very homogenous Teflon® AF layers having high dielectric strength (≈ 200 MV/m) can be prepared. However, because Teflon® has some problems, such as being relatively expensive and requiring licensing agreement with DuPont, manufacturer of Teflon® [23], some replacements have been proposed. Polyethylene films [40] or plasma-deposited Teflon®-like fluorocarbon films [41] that enable desirable electrowetting behaviour and provide minimal protein absorption, have been used to replace Teflon®.

As mentioned earlier, most of the EWOD-devices require hydrophobic coating to provide a large initial contact angle. This will raise problems when analyzing biological samples including proteins. Hydrophobic surface will experience inevitable cross-contamination of biomolecules, often named as biofouling [38]. The origin of this absorption is coming from hydrophobic or electrostatic interactions. Contamination usually modifies the surface properties, for example lowering the breakdown voltage of the insulator layer or decreasing the contact angle, resulting in a reduced device performance. Another problem arises when one droplet is moved on the area contaminated earlier by the residues of the previous droplet. These residues might then shift to the other droplet, resulting undesirable effects such as incorrect diagnosis from misleading assay outcome. [7] Because the avoidance of cross-contamination during droplet transportation is essential for useful EWOD-devices, several solutions that have been proposed to limit this absorption will be presented next.

Bayiati *et al*. [41] used fluorocarbon films using plasma-deposition. Compared to Teflon®, they can be deposited selectively on the surface, provided better adhesion to the surface and higher smoothness (thickness homogeneity) to reduce the hysteresis. Bayiati *et al*. also claimed that biofouling could be reduced using proper electrowetting conditions including applying voltage only short times and using solutions with higher pH values [41]. The drawback of this approach is that contact angle cahnge is quite low (30-40°) and that the fabrication process is required to be designed carefully because the properties of the fluorocarbon layer depend strongly on the chemical composition of the film. Some groups [42-44] have used optimization of device parameters to reduce adsorption. Yoon *et al.* minimized surface fouling by careful choice of the applied voltage (magnitude, bias, shape and duration) and solution pH, or even keeping the droplet in constant motion [42]. This is not very practical for longer analyses using assays that require solutions with different pHs. Droplet flow paths were optimized so that the cross-contamination was avoided (or at least minimized) in [43], whereas in [44], hydrophobic reactions were minimized using an open EWOD-system instead of a

cover system so that only one hydrophobic surface was present. However, none of these method can avoid hydrophobic interactions. The latter suffers also from evaporation and challenges of performing simple operations such as droplet cutting, the problems arising from open configuration as it has been discussed earlier. Biofouling can be reduced by transporting the droplet in immiscible fluid, such as silicone oil that will prevent also the evaporation [38] Replacing air by oil as a medium will ensure that the droplet is insulated and does not touch the hydrophobic surface. The problem is that this approach is not compatible with all the applications because organic solvents, such as ethanol and DMSO are miscible with medium oil, thus it can not be used with common cell solutions. For this reason, Luk *et al.* [45] used a biocompatible non-ionic surfactant additive to enable control of higher concentrations of proteins and cells without the need for radical changes in pH or oil as a medium. The problem is that when doing long duration analyses based on this method, a humidified environment to control droplet evaporation is required. Two other approaches, replacing permanent hydrophobic layer by removable plastic coverings [46] and use of surfactant solutions to dissolving and removing contaminants from the device surface [47], have been demonstrated. Unfortunately, both require additional tasks leading to increased operation times. For previous case, changing plastic covering manually will decrease also the level of automation of the system.

The last issue discussed in this section is the architecture of EWOD-systems. For system to perform multiple earlier discussed tasks that are needed for various applications, a sufficient amount of individually addressable electrodes is required. Using a conventional system, this would require that each electrode is connected to a power supply line individually. This would increase the complexity of the wiring, thus creating difficulties to connect every single electrode to an electric line without overlapping, crossing, or electrical shorting of any other electrode. One solution for this fabrication problem is to use a matrix technique called as multiplexing, where electrodes on the same row (and on column) are connected to same electric line. Now individual control is possible when switches are used to turning on certain rows and columns thus enabling that only wanted electrodes are activated. Even though it has been showed that multiplexing can be used to handle multiple droplets at the same time, it like any other EWOD-system, is still suffering a low level of flexibility based on fixed electrode structure. As mentioned earlier, the size of the electrode defines what droplet volumes can be controlled by the system. For this reason, Chiou *et al.* [48] proposed in 2003 a new approach, where a layer of photoconductive material is used to control the electrowetting behaviour optically. Now the size of the droplet, instead of depending on the physical dimensions of the fixed electrode, is defined by the area of the used light. This process, called as optoelectrowetting, is the main target of this work and will be presented in the next section.

2.3. Optoelectrowetting

The principle of optoelectrowetting (OEW) is described in the first part of this section. Because it is closely related to electrowetting, this section focuses on the differences between EWOD and OEW working mechanisms. In the latter part, some applications that have been demonstrated are described.

2.3.1. The principle of optoelectrowetting

Optoelectrowetting [48-53] uses the same surface tension modification principle than the conventional EWOD, where the contact angle change is determined by the voltage drop across the insulator layer. However, in OEW-devices an electrically conductive electrode layer covered with a photoconductive layer replaces a fixed electrode grid used in EWOD-systems. Amorphous silicon (a-Si) is the most used photoconductor. In addition, a light source, so far a laser with a power range of 1-5 mW, is implemented to the system. Conductivity of the photoconductive layer increases in the illuminated area, generating a so-called virtual electrode that is used for electrowetting-based droplet manipulation similarly than activating an individual fixed electrode in a conventional EWOD-system.

Usually the used electrode in the OEW device is a transparent ITO-glass (indium tin oxide) or a substrate coated with a very thin electrically conductive layer of metal to enable visual observation. The fabrication process of a typical OEW-device is described in Chapter 3. The benefit of a digital microfluidic system based on this approach is that the chip does not require individual electrical controlling of each electrode because the addressing is based on triggering light as can be seen from the concept of a closed OEW mechanism shown in Figure 2.9. In this set-up, a single featureless planar layer is used as the bottom electrode [50; 51]. The resistance part of the photoconductor is tunable by light as it can be noticed in Figure 2.9. This is because resistivity (and therefore resistance, expressed as R_{photo}) of the photoconductive layer is decreased when exposed to high intensity enough light. This means that the voltage drop is over the insulator layer thus electrowetting actuation of the droplet, is locally controlled by light. Other set-ups [48; 49; 52] have used a structure of an electrode grid below the photoconductive layer. In these systems, directing a light beam onto the electrode activates the individual electrode. It has been shown that a closed OEW-system is generally more common in practical applications than open optoelectrowetting device [52], mainly because of the operating problems (for instance droplet cutting) of non-covered systems as described previously in Section 2.2.

In the OEW mechanism, differently from EWOD, the potential is applied on electrodes continuously. This means, that OEW-based droplet motion and control is only possible when using alternative current (AC) voltage because the entire voltage drop would be across the insulating layer without light illumination in the direct current (DC) mode. The consequence of that would be that contact angle would decrease

everywhere around the droplet, so no pressure difference inside the droplet would be generated and the movement of the droplet would be unachievable. [48]

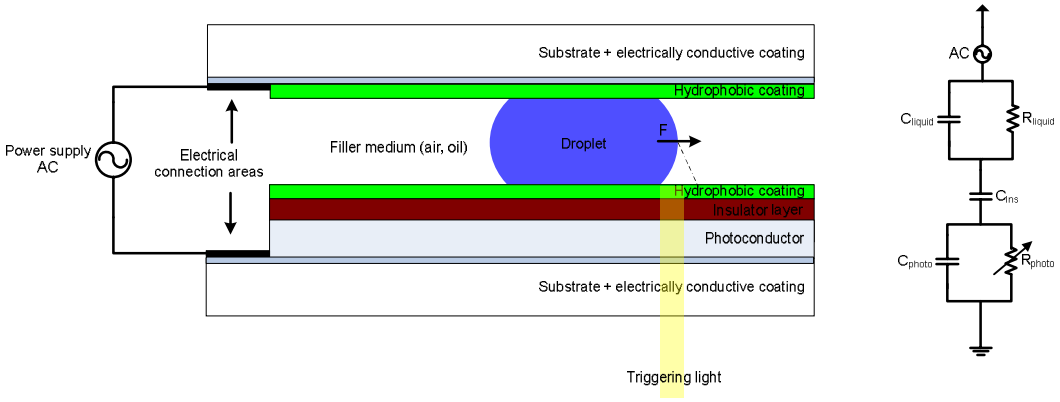

Figure 2.9: The principle and equivalent circuit of a closed optoelectrowetting device (not in scale). A droplet is sandwiched between a bottom photoconductive electrode and a top transparent electrode separated by the spacer (not shown). Triggering light creates a virtual electrode on the right side of the droplet, thus enabling droplet motion. EDL and hydrophobic coatings are now assumed very thin and are neglected in the equivalent circuit.

The difference in the operation principle of the OEW-device compared to the EWOD-device is described next. There is an additional photoconductive layer in the OEW-device as it can be noticed when comparing the equivalent circuits of EWOD and OEW shown in Figure 2.4 and in Figure 2.9, respectively. There are minor differences between the publications on how the OEW-device should be modelled. For instance [48-50] and [51] have a slightly different approach to represent the voltage and capacitance part in Equation (2-4). In the latter approach [51], the voltage drop is considered over the combination of both the photoconductive and the dielectric layer. Then the capacitance *C* in Equation (2-4) would be the total capacitance of the dielectric and the photoconductive layer. However, in this thesis, the original OEW-model [48] is used and will be presented next. The basic working mechanism of the OEW-system is based on the voltage drop over the insulator layer, resulting that in this approach the capacitance of the dielectric layer is considered as *C* in Equation (2-4). In the OEW-system, without light the impedance of the photoconductive layer is higher than that of the insulator layer, leading to the major voltage drop over this layer and prevent of electrowetting. Illumination will generate electron-hole pairs in the photoconductor (photogenerated charge carriers), creating so-called local virtual electrodes where the impedance of the photoconductor will drop. This drop will turn the impedance of the photoconductor layer below the impedance of the insulator layer, shifting the major voltage drop to the insulator layer in the illuminated regions, thus resulting local electrowetting as illustrated in Figure 2.9. [48]

The voltage drop over the insulator layer, U_{ins}, plays a major role for electrowetting modulation. This value of U_{ins} from the applied AC voltage U is calculated from the ratio of the impedance of the insulator layer Z_{ins} compared to the total impedance Z_{tot} of the system [48-50; 52]. Since the electrical double layer and hydrophobic coating are relatively thin and capacitances are in series, these two layers are usually neglected from the calculation for simplicity [52]. If expressing the impedances of the photoconductor layer and the liquid as Z_{photo} and Z_{liquid}, respectively, then U_{ins} can be presented using equation:

$$U_{ins} = \frac{Z_{ins}}{Z_{tot}} * U = \frac{Z_{ins}}{Z_{photo} + Z_{ins} + Z_{liquid}} * U \tag{2-18}$$

It should be noted, that now U and U_{ins} are presenting root-mean-square (RMS) values. Generally, the normalized voltage over the specific layer, expressed as U_{layer_norm}, can be calculated by comparing the impedance of the layer, Z_{layer} and the total impedance of the system:

$$U_{layer\_norm} = \frac{U_{layer}}{U} = \frac{Z_{layer}}{Z_{tot}} \tag{2-19}$$

The purpose of the applied light is to decrease the value of Z_{photo} so that the Z_{ins} will be dominating. Based on Equation (2-18), the combined Young-Lippmann for OEW can be presented as:

$$\cos\theta = \cos\theta_0 + \frac{\varepsilon_0 * \varepsilon_d}{2d\gamma_{LV}} * U_{ins}^{\ 2} = \cos\theta_0 + \frac{\varepsilon_0 * \varepsilon_d}{2d\gamma_{LV}} * \frac{Z_{ins}}{Z_{tot}} * U^2 \tag{2-20}$$

As it can be seen from the equation, when there is no light, the voltage drop over the insulator layer is small, resulting no or very small contact angle change. This OEW-actuation principle and more careful inspection of impedances of each layer will be discussed in the modelling part in Chapter 3.

The properties of the photoconductive layer are crucial for optimal OEW-actuation. Photosensitive hydrogenated amorphous silicon (a-Si:H) is so far the most common material used because it has many advantages, such as low dark conductivity (~10^{-8} S/cm), short carrier recombination lifetime (~µs) and response to visible light, allowing to use low cost light sources [48]. In the same study, the authors noticed that when illuminating a-Si-layer with light having intensity of 65 mW/cm^2, the conductivity was increased by 80 times. This was enough for successful OEW-based droplet movement. However, as will be mentioned in Chapter 3, the deposition of amorphous silicon requires usually still costly and complex high temperature plasma-enhanced chemical vapour deposition method. For this reason, it was proposed that a polymer layer having

high optoelectronic transmission efficiency could replace amorphous silicon layer [54]. With this method, the photoconductor layer could be spin-coated at room temperature, allowing cost effective mass-fabrication of OEW chip using flexible plastics. Further development of polymer, for instance to achieve better lifetime of the material, is required but anyhow this is a promising new approach for biological and biomedical applications.

At the moment, different droplet transportation speeds have been achieved using various set-ups. Using 4 milliwatt laser, a water droplet was moved 7 mm/s across the OEW-surface in a covered system [48], which was then enhanced to 78 mm/s for 100-nl droplet using a slightly modified set-up [49]. In open OEW-device [52], the maximum observed speed was 3.6 mm/s.

2.3.2. Possible applications

Since optoelectrowetting has been used for fundamental droplet operations so far, in this section only these are presented. However, optoelectrowetting seems a promising technique for droplet manipulation in various life science applications, such as DNA amplification procedures and parallel processing of samples for MALDI-MS analysis.

Fundamental droplet operations, which were discussed in more detail in Section 2.2.9 with EWOD case, have been demonstrated. Chiou *et al.* [48] reported a two-dimensional transportation of a de-ionized water droplet. Besides transporting a single droplet, it has been shown that with an OEW-device, multiple droplets can be created from an on-chip liquid reservoir, manipulated at the same time, thus cutting a droplet into two using two optical beams and moving them to opposite directions [49]. These operations, shown in Figure 2.10, were successfully completed by using multiple scanning light beams.

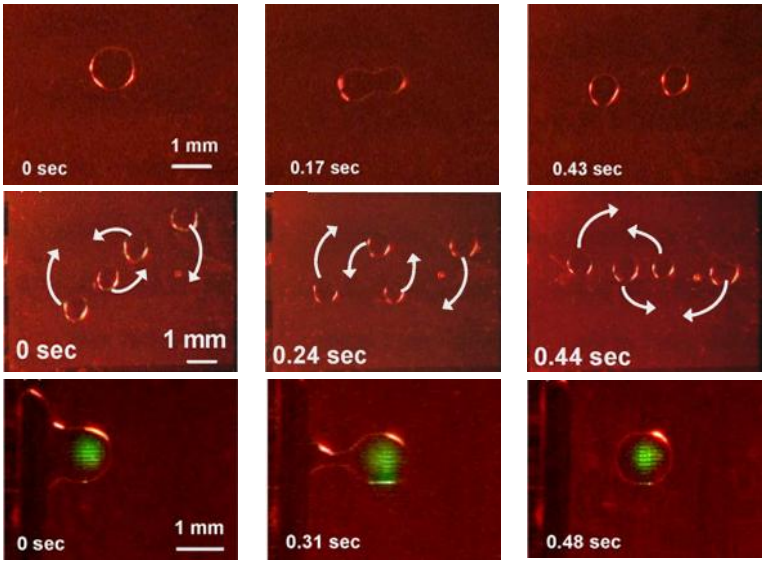

Figure 2.10: Demonstration of droplet splitting (topmost figures from left to right), parallel multiple droplet transportation (middle) and droplet creation from a liquid reservoir (lowest) [49].

Because of many possible OEW-driven microfluidics applications are closely related to a phenomenon called as dielectrophoresis, optically induced dielectrophoresis manipulation mechanism together with other relevant phenomenon will be discussed in the next section.

2.4. Other phenomena related to photoconductive surface

In this section, some operations that could be performed by triggering the photoconductor layer are shortly presented. Section 2.4.1 focuses on optically induced dielectrophoresis for particle and cell manipulation whereas electroporation, electrical cell lysis and stem cell stimulation are briefly reviewed in Section 2.4.2.

2.4.1. Dielectrophoresis and optically induced dielectrophoresis

This section presents first the principle of dielectrophoresis, introduced by Pohl [55] in 1978, before explaining a novel idea of optically induced dielectrophoresis proposed by Chiou *et al.* [56; 57] in 2003. In the last part, some applications using optically induced dielectrophoresis are presented.

Dielectrophoresis

Dielectrophoresis (DEP) can be described as the forces affecting a polarisable particle created by a non-uniform electric field. The particle will form a dipole inside the electric field, and will experience attractive (positive DEP) or repulsive (negative DEP)

forces depending on the dielectric properties (permittivity and conductivity) of the particle and surrounding medium and the frequency of the applied electric field. Figure 2.11 shows the principle of generated positive DEP force towards the higher electric field (left particle) and negative DEP force repelling the right particle in the direction of lower electric field strength because of different dielectric properties. For a circular particle with radius r and surrounded by the medium with permittivity of ε_m, this DEP force F_{DEP} can be calculated by [55]:

$$F_{DEP} = 2\pi * r^3 * \varepsilon_m * \mathrm{Re}[K(\omega)]\Delta(U^2) \tag{2-21}$$

where U is RMS-value of the applied electric field and $Re[K(\omega)]$ is the real part of the Clausius-Mossotti (CM) factor. It depends on the permittivities and conductivities of the surrounding medium and the particle ε_m, ε_p and σ_{me}, σ_p respectively and the angular frequency of the electric field ω. Dielectrophoretic force is frequency dependant because the magnitude of real part of CM factor varies with frequency and is expressed by [55]:

$$\mathrm{Re}[K(\omega)] = \frac{\varepsilon_p^{\,*} - \varepsilon_m^{\,*}}{\varepsilon_p^{\,*} + 2 * \varepsilon_m^{\,*}}$$
$$\varepsilon_p^{\,*} = \varepsilon_p - j\frac{\sigma_p}{\omega}, \varepsilon_m^{\,*} = \varepsilon_m - j\frac{\sigma_{me}}{\omega} \tag{2-22}$$

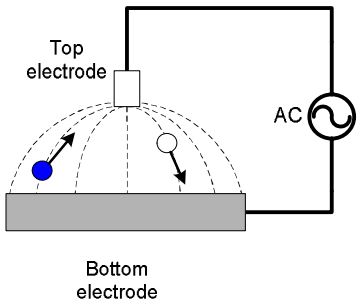

Figure 2.11: The principle of positive (left particle) and negative (right particle) dielectrophoretic forces.

The real part of the CM factor will define, is the particle experiencing positive ($Re[K(\omega)] > 0$) or negative force towards the higher electric field. This allows separation of different particle types based on their dielectric properties. This idea is shown in Figure 2.12, where simulated values of $Re[K(\omega)]$ are plotted for typical live and dead mammalian cells. It the simulation, cell properties are calculated using a so-called single-cell approach. Firstly, the cell is modelled as a combination of a membrane and a cytoplasm having permittivities of $\varepsilon_{membrane}$ and ε_{cyto}, respectively.

Using permittivity values together with outer radius of a cell r_{cell} and a radius of cytoplasm r_{cyto}, a single-cell model having a new permittivity of ε_{cell}' can be obtained [58 and references therein]. Using this approach, as shown in Figure 2.12, it can be noticed that if the applied electric field frequency is below 100kHz, live cell will experience negative DEP force whereas dead cell is affected by positive DEP, thus enabling separation of live and dead cells. For medium, relative permittivity and conductivity, were assumed to be 78 and 0.1 S/m, respectively. Cell properties are from [58].

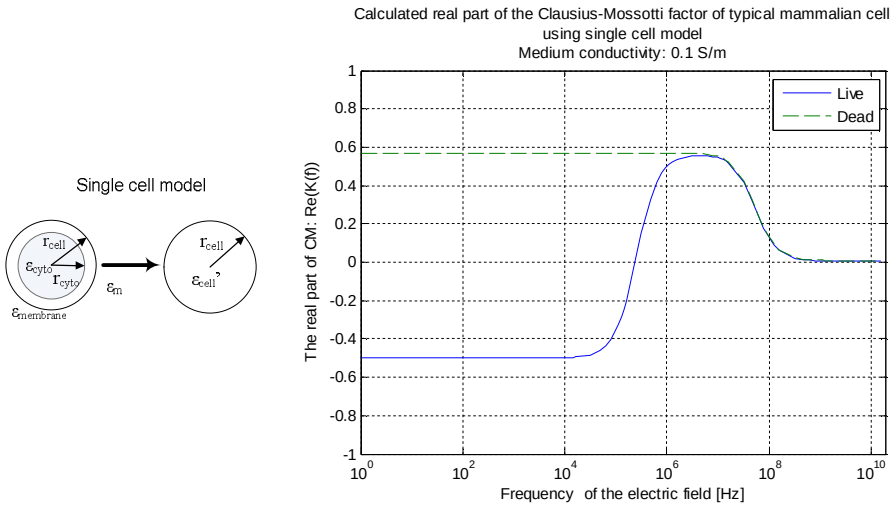

Figure 2.12: The simulated real part of CM factor for typical live and dead mammalian cell using single cell model shown in the left. See text for the details.

Even though it has been demonstrated that it is possible to manipulate particles effectively over a large area using DEP, it has similar problems to EWOD. Fixed electrodes processed by photolithographic techniques are not reconfigurable (different sizes for different particles, for instance cells and microparticles), reducing the flexibility of the system. For this reason, a reconfigurable and continuous system where light-patterned virtual electrodes would address dielectrophoretic forces proposed by Chiou *et al.* [57; 58] is presented next.

Optically induced dielectrophoresis

Chiou *et al.* [56; 57] demonstrated a concept where particle and cell manipulation was performed by optically induced dielectrophoresis. The authors in [57] named the concept as optoelectronic tweezers (OET). Compared to conventional DEP-device, the fabrication method of the OET-device, which is similar to the OEW-device except the insulator layer is usually only a thin hydrophobic coating on top of the photoconductor, is less expensive and easier because it requires no photolithography. A schematic of a typical OET-device is shown in Figure 2.13. To trigger virtual electrodes, various

illumination set-ups have been used. The prior experiments were performed using a 0.8mW helium-neon (He-Ne) laser source [56], but later it has been used a combination of common data projector and objective with a different incoherent light sources, such as a light emitting diode [57] or a 150W halogen lamp [59].

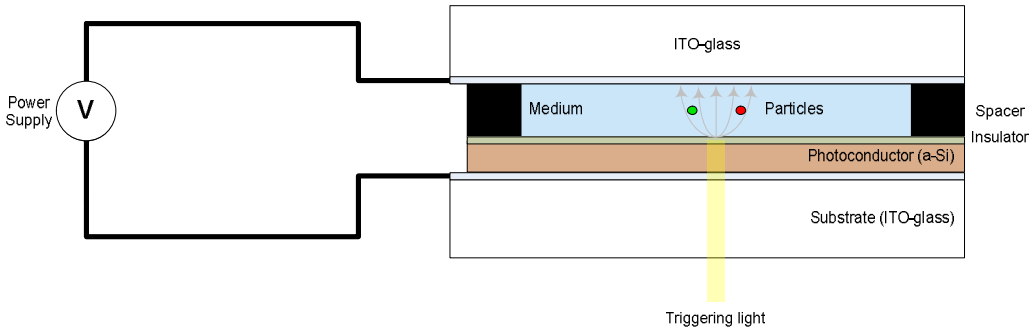

Figure 2.13: A schematic of a typical OET-device (not in scale). Triggering light will created a non-uniform electric field, thus enabling light controlled DEP-actuation of particle.

The working mechanism of the OET-device is following. Without light, the major voltage drop will be over the photoconductor as in the OEW-device. When light is exposed, this major voltage drop will be shifted locally to the medium (compared to the insulator layer in the OEW-device) because there is only a thin insulator layer to prevent electrolysis. These locally created virtual electrodes will generate non-uniform electric fields inside the chamber allowing particle manipulation. If the system is integrated with microvision-based image analysis, the OET-device can separate automatically particles based on their visual attributes such as size, color, and texture [59]. However, the main problem of each typical OET device is that the maximum photoconductivity of amorphous silicon (lower than 0.1 S/m) will limit the working range to low-conductive media. Therefore, the OET-device can not be used with high conductive solutions such as real cell culture media. Proposed solution is to replace a-Si layer with a surface consisting of silicon bipolar phototransistors [60; 61]. Even though this approach enables the manipulation of particles in high conductive solutions; it will also increase the complexity and cost of the system.

Applications

In this section, some applications using the principle of OET are shortly overviewed. For example in many biomedical processes, such as in sample pretreatment [62], a high-speed and sensitivity separation of microparticles or cells is necessary. OET-based systems seem to provide liable and fast method for separation. As mentioned, manipulation of multiple particles individually at the same time by optically induced dielectrophoresis forces was demonstrated first time by Chiou *et al* [57]. In their set-up, which was using a standard OET device, over 15 000 light-induced particle traps were

generated on a 1.3 mm x 1.0 mm area using a commercial digital light processing (DLP) projector. Polystyrene beads with diameter of 4.5µm were trapped and transported in parallel. Sorting of different particles by their sizes (10µm and 24 µm) was successful. Furthermore, the device was capable of selectively collect live human B cells from a mixture of live and dead cells.

The same group showed later more complex patterning of live human B cells [58]. They have also demonstrated automated particle sorting by integrating microvision-based pattern recognition with OET device as was mentioned earlier [59]. In the set-up, image analysis and pattern recognition was used as a feedback for pattern generation. Their system could automatically recognize, short and move in parallel polystyrene particles with different sizes of 10µm, 16µm and 20 µm. Negative DEP force generated by automatically created light patterns was used in manipulation. They claim that with further optimizing, the system could be able to short particles also with their different colors, shapes and textures. Alternative solution to separate different particles could be varying wavelength, width and brightness of the triggering light to obtain various DEP forces. This was proposed by Lin *et al*. [63]. They managed to separate different particles automatically with a high throughput. They were able to sort automatically polystyrene beads with different sizes (10 to 20 µm) by scanning manipulation area with different line patterns. As mentioned previously, it should be remembered that one major problem stays with all the proposed systems; they do not work efficiently when dealing with high-conductive solutions as was already discussed in Section 2.4.1.

Table 2.1 provides a summary of the reported cell manipulation experiments using the OET-devices. In the table, used cell types, voltages and frequencies together with light sources that have been used in cell manipulation are listed.

Table 2.1: The summary of OET cell manipulation [56-61].

Used cell types	Red and white blood cells, E. coli, HeLa, Jurkat
Used voltages [V]	3 – 14
Used frequencies [kHz]	100 - 200
Used light sources	LED, 0.8 mW He-Ne laser 150 W halogen lamp

As it can be noticed from the table presented above, various cell types have been manipulated effectively with the OET-device. It should be remembered that these tasks have been mainly performed using non-real cell culture media, thus affecting the cell viability.

2.4.2. Electroporation, electrical cell lysis and stem cell stimulation

In this section, electroporation, electrical cell lysis and stem cell stimulation are presented without going in details. References given following are providing more information. Some applications are also illustrated.

Electroporation and optically induced electroporation

In electroporation, high electric fields are applied to a cell. The idea is to *temporarily* increase the permeability of the cell membrane by creating pores on the cell membrane via electric fields. This structural rearrangement of the cell membrane will happen if opposite charges of outer and inner membrane, called as the transmembrane potential $\Delta\varphi$, is higher than the dielectric breakdown voltage of the cell membrane, typically between 0.2 V to 1.5 V. Now membrane will pass polar substances, such as proteins or drugs, and these can be introduced into the cell. Using this approach, a single cell electroporation device has been introduced using conventional microelectrodes. [64]

Electroporation is one of the most common cell membrane poration methods and it has various applications in the field of medicine, biology and biotechnology, ranging from cell research by loading DNA, fluorescence probes, antibodies and enzymes into cell to drug delivery by introducing molecules inside cell [65; 66]. Conventional poration methods are unable to manipulate multiple cells at the same time. A methdod proposed in [67] overcomes the problem by integrating OET-based cell manipulation to parallel single cell electroporation. The system set-up is shown in Figure 2.14. First, several HeLa cells were transported by optically induced dielectrophoretic forces using lower electric field (2 kV/m). Some of manipulated cells were chosen and subjected to the electroporation changing electric bias to 150 kV/m. The experiments showed that they were able to inject fluorescence inside selected cells and kept them alive, proving successful reversible electroporation.

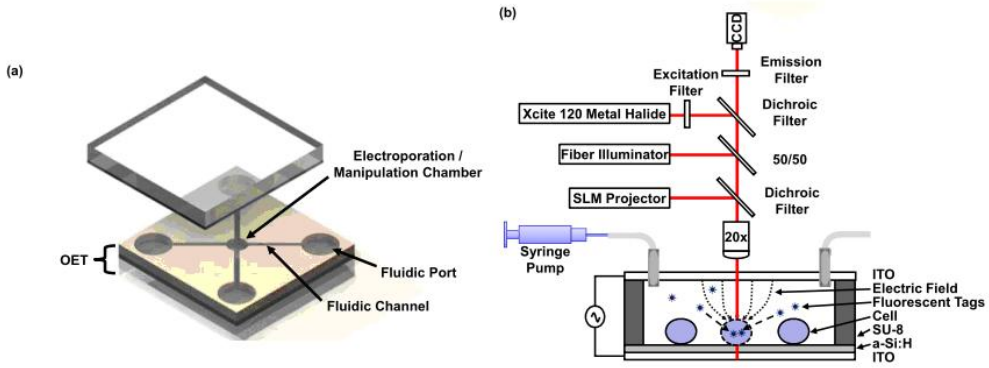

Figure 2.14: a) Device layout and b) diagram of working principle of light-induced electroporation [67].

The authors in [67] concluded that optimal electric field strength for HeLa cells is between 140-230 kV/m. With higher electric field, cell lysis was increased. This demonstration verifies that OET-based device is capable to perform multiple tasks (cell manipulation, electroporation, and lysis) which are required for true cellular manipulation platform.

Electrical cell lysis and optically induced electrical cell lysis

In this part, electric cell lysis together with some applications are presented. In a variety of research fields such as genome research and drug development, cell lysis is a common and very crucial technique to obtain intracellular materials such as proteins and nucleic acids for further analysis [68]. The idea in cell lysis is to disrupt the membrane of the cell so that it will break. With many conventional methods, the main challenges are to lyse a specific cell within a group of cells and to break only the cell membrane without damaging the nucleus inside. This is essential especially when the interest is in mitochondria studies. [69]. In electrical cell lysis, breaking of the cell is performed using high enough electric field. It has been shown that a micro cell lysis device using patterned conventional microelectrodes with small gaps can reduce the required voltage for cell lysis. [68]. Recently, it has been demonstrated that virtual electrodes created on a photoconductive surface, allow more flexible and better parallel control of an individual cell. [69; 70] The principle of optically induced dielectrophoresis-based electroporation and cell lysis is shown in Figure 2.15.

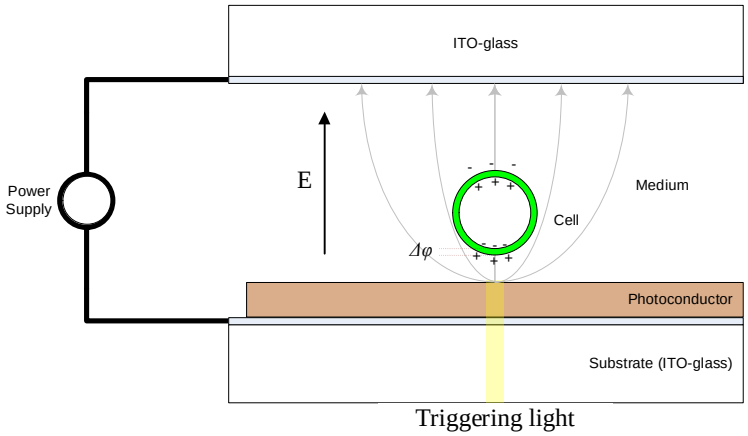

Figure 2.15: A schematic of an OET-based electroporation and cell lysis device (not in scale). The cell is exaggerated drawn to shown membrane potential Δφ which is controlled by the induced electric field inside the chamber. No insulator layer is provided in this set-up [redrawn from 69].

The basic idea of OET-based electroporation and cell lysis is to use light to introduce high enough electric field strength over the chosen cell. With this approach, while using a standard data projector [70], an individual and parallel reconfigurable operation is possible. Experiments have shown that for different cell types, various electrical treatments are required. To perform cell lysis, for instance human white blood cells (WBC) required 200 kV/m at AC of 3 MHz for optimal lysis rate [71] whereas *E. coli* was lysed using over 700 kV/m of 500 µs DC square pulse [68]. No lysis of *E. coli* was obtained using AC up to 2.1 MV/m at 2 MHz. Lin *et al.* [69] lysed mammalian

cells including a fibroblast cell and an oral cancer by applying point-to-point voltages of 7 and 9 V at 20 kHz, respectively. However they mentioned neither how high electric field was applied electric field, nor the height of the used cell chamber. Based on the presented experiments, Table 2.2 provides a summary of used parameters for electrical cell lysis with different cells.

Table 2.2: The summary of electrical cell lysis.

Used cell types	E. coli [68]	Mammalian fibroblast [69]	HeLa [70]	WBC [71]
Used frequencies [kHz]	0 (DC)	20	100	3000
Pulse width [µs]	500 (square)	-	-	-
Threshold electric field strength [kV/m]	700	? (7V applied)	~1500	200

Based on the table provided above (and as mentioned in [69]), it can be concluded, that operational conditions such as voltage, illumination power and beam spot size affect the cell lysis rate on OET based cell lysis devices and thus should be optimized for different cells individually.

Electrical stem cell stimulation and optically induced electrical stem cell stimulation

The principle of stem cell stimulation electrically is presented next. It will focus on the parameters required for stimulation based on a literature survey. A new concept of electrical stem cell stimulation using optically created virtual electrodes is presented with other applications in Section 2.5.3. Stem cells can be defined as specific cells having characteristics that distinguish them from the other types of cells. Firstly, being unspecialized cells, they can renew themselves through cell division for a long timeperiod. Secondly, under certain experimental or physiological conditions they can become in theory any type of cell with special functions. This phenomenon is called a cell differentiation. The purpose of stem cell stimulation is to make them differentiate to desired cells such as cardiac myocytes. This would allow using stem cells as a treatment in many diseases such as Parkinson's disease. Table 2.3 summarizes some of the electrical stem stimulation results that have been performed. Because the purpose is to give only some rough idea of the required electrical treatment, it is not a comprehensive summary. It should be noticed that cellular differentiation in the developing embryo is a complex process including numerous processes that are required to perform in addition to electrical stimulation. [72]

Table 2.3: Summary of electrical cell stimulation results

Cell type	AC-treatment	DC-treatment	Results
4-day-old embryoid bodies of mouse embryonic fibroblast [73]	-	A single, 90 s pulse 100 – 500 V/m	500 V/m enhanced cardiomyocyte differentiation
4-day-old murine embryoid bodies [74]	-	A single 60 s pulse 125 – 750 V/m	500 V/m twofold increase of angiogenesis values
Neonatal rat ventricular myocytes [75]	Rectangular pulse (1Hz, 2 ms) for 5 days, 500 V/m	-	Induced cell alignment and coupling, 7x increment of contractions
Embryoid bodies derived from human embryonic stem cells (4 and 8 days old) [76]	-	A square-wave pulse (1 and 90 s) , 1000 V/m	The highest rate of reactive oxygen species generation observed for signal duration of 90 s

Based on summary in presented in Table 2.3, requirements for stem cell stimulation device are given. Requirements are categorized into two groups, electrical and optical, as shown in Table 2.4.

Table 2.4: Electrical stem cell stimulation - requirements

ELECTIRCAL REQUIREMENTS	**Electric field strength [V/m]**	~500
	Frequency [Hz]	DC (AC: 1)
OPTICAL REQUIREMENTS	**Minimum and maximum pulse length**	2 ms to 90s
	Maximum pulse frequency	5 Hz

For electrical stem cell stimulation, DC-voltage is mostly used. It is not difficult to satisfy optical requirements of two milliseconds pulse length if using a-Si as a photoconductive material. This is because of its short carrier recombination lifetime as mentioned before.

2.4.3. Summary

A summary of the requirements for operations presented previously in Section 2.4 is given in this section. Table 2.5 presents the minimum and the desirable requirements that the device should fulfill to be able to perform all the tasks listed in earlier. With the minimum requirements, all the operations should be possible at least with one cell type. On the other hand, if the system can achieve the desirable requirements, all the operations are possible with each cell type discussed in Section 2.4.

Table 2.5: Minimum and desirable properties of system using photoconductive layer

REQUIREMENTS		Minimum	Desirable
ELECTIRCAL REQUIREMENTS	**Electric field strength [kV/m]**	0-150	0-1000
	Frequency [kHz]	DC to 100	DC to 3000
OPTICAL REQUIREMENTS	**Pulse length**	1ms to 90s	0.1ms to 90s
	Pulse frequency [Hz]	1	5

It should be noticed, that different cells requires different operations requirements, and therefore it is not easy to control all the cells with a single set-up. Most probably, a more suitable solution is to design an own device for each cell type or operation. However, this would decrease the level of the flexibility of the system.

2.5. Potential applications

The purpose of this section is to present some novel applications, where optically controlled surface could be used. These potential applications are outlined without going into the details. It is discussed, how combining OEW and OET techniques could increase the flexibility, speed, accuracy and thus performance of the system. The purpose of this part is not to provide exact parameters for the requirements but more like presenting promising concepts. Firstly, this section considers the integration of OEW and OET devices. Secondly, a concept of a reconfigurable valve is presented. In addition, the stem cell stimulation device and the Lab-On-a-Chip concept using photoconductive surface are outlined.

2.5.1. Integrating OEW and OET devices

Integration of parallel individual particle control and discrete droplet manipulation is required to realize a real Lab-On-a-Chip device based on digital microfluidics. The basic droplet manipulation operations required for digital microfluidics circuits are creation, transportation, merging (mixing) and cutting (splitting) the droplet. As it has been shown previously, Cho *et al.* [30] demonstrated all these fundamental operations using electrowetting-based actuation of the droplets in air. They have also proposed a system for particle separation and concentration inside the droplet using electrophoresis forces [26]. However, drawback of this approach is that the system is not suitable for a single cell study because similar particles having same electrical properties such as charge cannot be manipulated separately.

For the reason presented previously, Shah *et al.* [77; 78] integrated optoelectronic tweezers and EWOD-driven droplet microfluidics device. OET enables that particles can be individually controlled based on their different dielectric properties or visual differences such as size and color thus allowing greater control and flexibility for cell studies. With this integration, studying of single cell behaviour could be accomplished more accurately. The first generation device, which schematic is shown in Figure 2.16a) [77], consists of center OET region for particle control surrounded by EWOD area for

droplet manipulation. Even though this set-up was able to perform both EWOD and OET functions individually, it was difficult to demonstrate a complete sequence of EWOD-OET operations. OET is ineffective in EWOD region while the region of OET cannot be used for EWOD droplet manipulation. This reduces the effectiveness of the illustrated system, because particle manipulation is restricted to a relatively small OET region. It has also been studied how the hydrophobicity of the OET region affects the integration effectiveness [78]. Three different possible designs with different hydrophobic OET area sizes were considered as illustrated in Figure 2.16b). It was noticed that it was quite difficult to capture all the particles inside the droplet and maintain them in the desired positions.

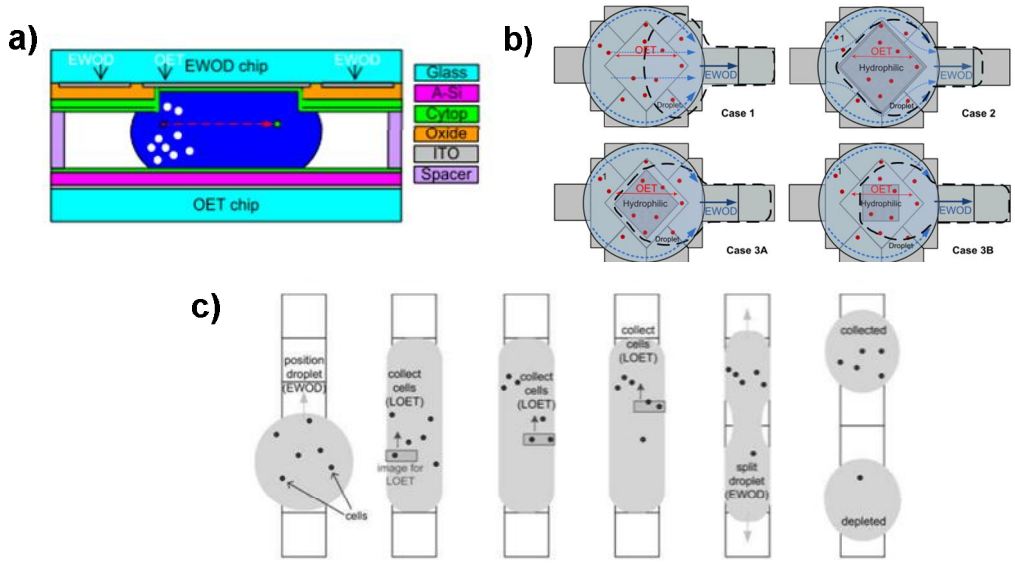

Figure 2.16: a) A schematic of device integrating OET and EWOD. Top glass is composed of central OET electrodes surrounded by EWOD electrodes [77]. b) Various different designs of OET area in integrated particle and droplet manipulation device [From the supplementary material of 78]. c) A schematic of operations accomplished on the integrated LOET/EWOD device. [79] See text for details of each step.

Because the first-generation integrated EWOD-OET device was insufficient to control droplets and particles effectively, a new device to overcome these problems was proposed [78; 79]. In this system, a typical EWOD device (the top layer of the system) without having special "OET only" region is integrated with so-called lateral-field OET (LOET) device (bottom layer). The main difference between OET and LOET is that latter is using electrode fingers located on the same plate to generate lateral electric field instead of vertically oriented as in conventional OET. This way, both OET and EWOD manipulations can performed in the whole chip area, thus eliminating the problems occurred in the first-generation devices discussed earlier. The schematic of the system is shown in Figure 2.16c), where following operations are performed from left to right: i) a droplet containing cells is placed on the surface. ii) The droplet is positioned properly

by EWOD to enhance LOET manipulation and iii) the cells are transported upwards by moving projected image pattern multiple times because of the limited LOET image area compared to droplet dimensions. iv) Only a few cells are not concentrated on one region. v) The droplet is split by EWOD, vi) resulting that cells are separated in collected and depleted droplets. Successful live HeLa cell manipulation within a droplet was demonstrated [79].

2.5.2. Reconfigurable valve

In many biological applications, such as disease diagnosis for point-of-care devices, it is essential to achieve an exact amount of liquid. Many conventional systems, based on pumps, valves and fixed microchannels manufactured by using typical fabrication methods [80], are well designed to deliver precise volume based on their physical dimension. The systems are using passive valves to ensure that the volume is as desired.

A common problem with the presented devices is that they can provide only certain specified volumes. If another volume is demanded, a new chip with changed dimension is required to be designed and fabricated thus restricting the flexibility of the system in various applications. Here it is proposed a method that integrates OEW to conventional microchannel-based liquid handling. PDMS microchannels, opened in the bottom, are placed on the top of the typical OEW chip, as described earlier except that now only a small part of the surface is covered with hydrophobic coating, to form closed microchannels for pressure driven microfluidics. Instead of getting only one fixed volume, for instance five microliters, by manipulating the hydrophobic area different volumes could be achieved depending on the size of the projected pattern on the hydrophobic surface at the end of microchannel as shown in Figure 2.17. First the liquid is moved to hydrophilic-hydrophobic interface (point A) by conventional pressure-based micropump. When liquid is approaching the interface, pressure is decreased so that liquid is still moving in hydrophilic area. Now, if pressure is kept constant and is low enough, liquid will stop in the interface because higher-pressure requirement in the hydrophobic area. Similar approach but using conventional EWOD actuation mechanism has been used to control continuous fluid flow [81]. Reconfigurable valve could be now performed by implementing optoelectrowetting mechanism to locally change hydrophobic area to hydrophilic on the illuminated area. When liquid is stopped in the desired position between interface (A) and reaction chamber (C), the rest excess liquid could be directed to the waste chamber (B). The total volume of the liquid that would enter to the reaction chamber would then depend on the area (width) of projected light, allowing flexible control of volume size by using computer-controlled image generation.

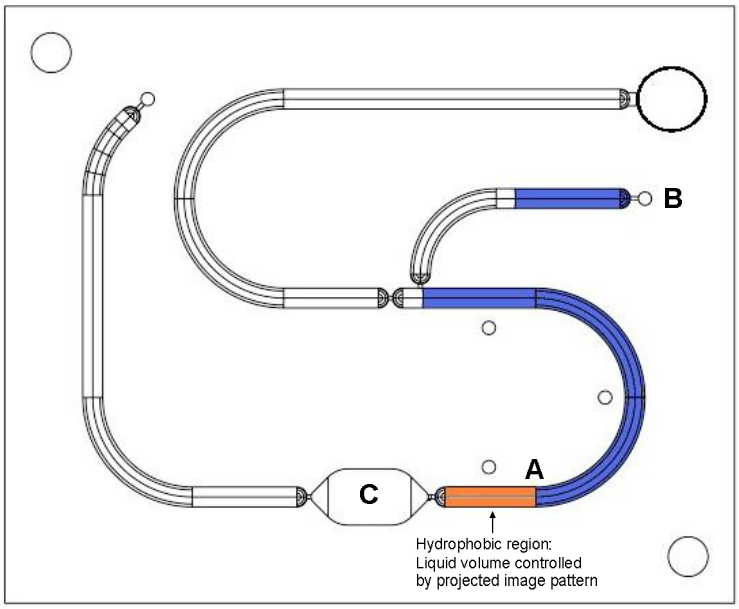

Figure 2.17: Illustration of the proposed reconfigurable valve prototype chip based on continuous flow in PDMS microchannel and hydrophobic optoelectrowetting area.

The concept of reconfigurable valve was explained in this section. It should be noticed that careful design of the parameters, such as channel dimensions, applied pressures and voltages and light intensities and patterns is required to enable effective reconfigurable valve for continuous microfluidic applications.

2.5.3. Stem cell stimulation using optically triggered virtual electrodes

Stem cell stimulation is concerned in this section. To better illustrate the proposed concept, a brief theory of electrical stem stimulation is given before proposing a flexible stem cell device.

Conventional electrical stem cell stimulation

A common method for electrical stimulation and monitoring of electrical activity of electrogenic cells, either in cardiac, muscle and neuronal tissue or isolated, is to use MEAs (Multi-Electrode Array) that is a two-dimensional designed arrangement of voltage probes. The tissue containing cells is typically separated from the electrodes by silicon nitride layer. The purpose of electrical stimulation is to enhance stem cell (for an example neuronal or cardiomyocyte) differentiation in a controlled manner by applying electrical potential on the culture chamber. Electrical treatment should produce functional cells for stem cell based treatments such as heart or brain disorder. For this reason, also measuring the electrical activity of stem cell during stimulation is essential. A typical set-up using a MEA, shown in Figure 2.18a), includes substrate-integrated planar electrodes used for both electrical activity recording and electrical stimulation.

Extracellular stimulation is performed by applying either voltage or current pulses to the MEA electrodes. Electrical activity can be measured by recording the spatial distribution of the voltage in a thin layer of a conductive tissue sheet above the MEA electrodes relative to the reference electrode located in the solution as illustrated in Figure 2.18a). [82]

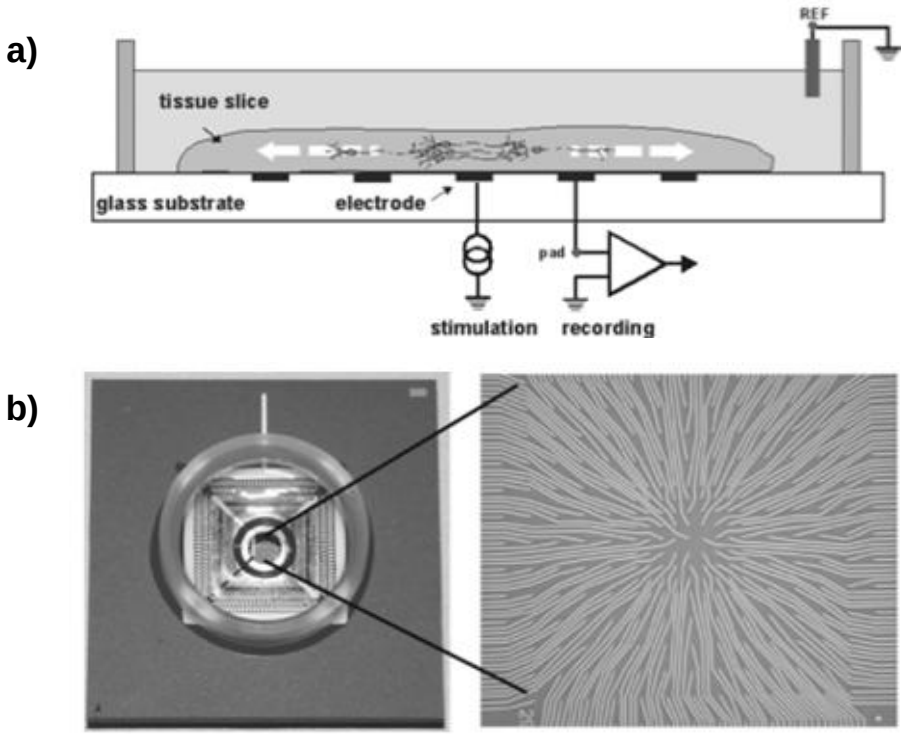

Figure 2.18: a) A schematic of MEA-based system for electrical stimulation and activity recording in tissue slices, b) layout of a high-density MEA. [82]

When using the typical MEA surface, it is crucial to achieve high enough signal-to-noise ratio (SNR) for extracellular recordings. This can only obtained if a high spatial resolution (interelectrode distance is small) and a tight contact between the electrodes and the tissue is provided. Standard MEAs usually have 8x8, 6x10 or even 2x30 electrodes, last one providing either a good spatial resolution in a small recording area or vice versa. To achieve both a high resolution and a large recording area, high-density MEAs have been developed. MEAs are wire-bonded to a standard PC socket, enabling easy mounting of the chip in an industry standard holder. The layout of 256 electrodes in an area of 2.8 x 2.8 mm^2 is presented in Figure 2.18b). Even this more sophisticated system presented above encounters problems when working with samples, such as acute brain slices, where a high-accuracy mounting and positioning is required. The distance between the intact cell layer and the MEA electrode can easily expand too large thus lowering SNR of the recorded signal. Even though difficulties appeared with the slice position and the contact between the tissue and electrodes can be improved by

developing MEAs with numerous opening in the substrate [82], still higher spatial resolution is desirable to enhance measurement data collection and analysis.

Electrical stem cell stimulation using photoconductive layer

Based on the observations discussed in the previous section, a stimulation chamber, where a photoconductive layer integrated with light-patterned virtual electrode generation would be used to replace MEA surface, seems promising. This system, illustrated in Figure 2.19, could allow stimulation in the desired area using a virtual electrode where visual inspection including image analysis and pattern recognition would be used.

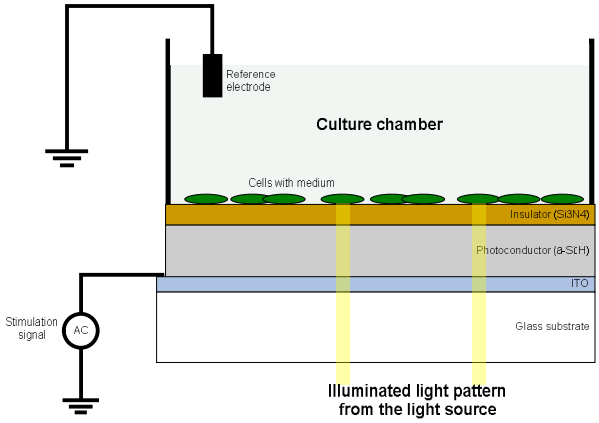

Figure 2.19: A concept of the proposed stem cell stimulation device using optically induced virtual electrodes (not in scale).

If the stimulation requires a closed system, the reference electrode could be ITO-glass placed on top of the culture chamber opposite to the bottom electrode presented in Figure 2.19. Parameters that have to be considered are the thicknesses of each layer, biocompatibility of the surface where cells are adhered, and applied voltages. Silicon nitride, which has been shown to be a biocompatible material [83-86], does not induce toxic reactions in cells/tissues they are placed in intimate contact with, is used as an insulator layer in this set-up. A relative thin insulator layer is required so that the major voltage drop will be inside the culture chamber in the illuminated areas, whereas in the dark regions the major voltage drop should be over photoconductive layer (amorphous silicon). Because of the limited conductivity of a-Si, one challenge with the proposed system is when working with typical high-conductive culture media as it was discussed previously. In the electrical stimulation, the applied voltage plays an essential role. Obviously, different cell types should be treated differently. For example, DC-pulses with 500 V/m electric field strength was used to enhanced cardiomyocyte differentiation of undifferentiated mouse embryonic [73]. In the proposed culture chamber having height of one millimeter, it would mean that the electric field potential

over culture chamber should be around 0.5 V on the illuminated areas. The set-up is required to design so that strong enough electric fields are generated in the culture chamber without exceeding the dielectric strengths of each layer and thus preventing electrolysis and undesired electrochemical reaction at the interface of the insulator and electrolyte.

2.5.4. Lab-On-a-Chip platform for diagnostic purpose

The discussion about Lab-On-a-Chip (LOC) system that would use OEW (or EWOD) and OET principles to perform multiple task on a single device is provided in this part. It will present typical tasks that are required in total analysis systems and consider how these tasks could be accomplished using OEW/OET mechanisms. The ultimate goal of the lab-on-chip technology is to establish a complete system including multistep automatic standard laboratory processes on a microscale chip. An automatic chip that would be able to fulfill multiple tasks would reduce the need of skilled technicians, leading to more cost-effective and faster analysis. Given molecular data collection for diagnostic as an example, it is estimated that 90% of the cost and 95% of total time needed is related to sample collection, transportation and preparation [87]. Droplet based liquid manipulation using OEW integrated effectively with OET for a single particle/cell control on a same chip would also remove the need of mechanical components such pumps, channels, mixer, and valves. While lowering sample and reagent consumption, this system could enhance the flexibility of the system compared to conventional techniques.

The fundamental droplet and particle manipulation operations are the basic requirements for total Lab-On-a-Chip device. The system must be able to perform routine droplet-based functions such as creation, transportation, cutting and merging of droplets. Furthermore, more advanced operations including separating, mixing and concentration control of biological reagents and samples, are essential for effective Lab-On-a-Chip systems [30]. Based on the observations in previous sections, most of the required sample preparation and analysis steps have been demonstrated with OEW/OET device individually. Integration of all these tasks successfully would enable the development of a digitally controlled general-purpose platform, realizing a programmable chemistry Lab-On-a-Chip. However, there are still various challenges to overcome, such as biofouling on hydrophobic surface, working with high-conductive solutions and successful integration of OET and OEW as it has been discussed. The recent development of this research area shows the potential of OEW+OET device and might lead to a platform where droplet manipulation steps such as sample preparation, creation and transportation are fully automated.

2.6. Conclusion

In this chapter, theoretical background that is required to understand optically induced electrowetting mechanism was presented. The physics of microliter droplet and

electrowetting were described extensively, whereas other observed phenomena related to photoconductive surface were illustrated non-extensively. Section 2.5 focused on applications, where the described manipulation techniques might have potential to enhance dramatically the system performance. This last part was provided to better illustrate the wide range of applications, where photoconductive surface could be used.

3. TESTING AND MODELLING OPTOELECTROWETTING

In this chapter, fabrication of the OEW chips, performed experiments, the modelling procedure of the OEW device and proposed modifications for the device are reported. Section 3.1 provides a short summary of required fabrication steps of OEW chips, whereas experiments are reported in the next section. The modelling part is covered in Sections 3.3 and 3.4. Based on the discovered reasons for the problems encountered during the tests, a new model for the new chip is proposed in Section 3.5. Unfortunately, the limitations of the project could not allow fabricating this chip, preventing to test and verify the proposed model. Some supporting tests for the model proposed in this chapter are reported in Chapter 4.

3.1. Fabrication procedures of OEW chips

Collaboration in the project was such that the partner in Helsinki University of Technology (HUT) [88] develops the fabrication processes of the chip and TUT develops bio applications for the produced chips. For this reason, the fabrication procedures of the first OEW chips are very shortly described. The process involves three main steps. Firstly, a bottom electrode is covered with a photoconductive layer. Next, an insulator layer is deposited on top of the photoconductor. If needed, an additional hydrophobic layer is coated. Finally, one edge of the chip is etched to enable electrical connection to the bottom electrode. Next in this section, these steps are explained in more details.

The chips were fabricated using facilities provided by Micronova [89]. The system used for Plasma Enhanced Chemical Vapour Deposition (PECVD) was Plasmalab 80 Plus from Oxford Instruments Plasma Technology, UK [90]. ITO-glass type CEC020S ($\leq$ 20 Ω/square) from Praezisions Glas & Optik GmbH (PGO) [91] was used as both bottom and top electrode. First, a 1.5µm-thick a-Si layer was deposited on top of an ITO-electrode using PECVD. It was noticed that it is crucial to clean the ITO-surface before deposition. The photoconductor layer was coated with silicon nitride (Si_3N_4) or Teflon® layer. Silicon nitride was deposited using PECVD machine whereas Reactive Ion Etching (RIE) machine is used for deposition of Teflon® layer. To finish the chip and provide electrical connection, one corner of the chip was etched to expose an electrically conductive ITO-layer.

Two different batches of the OEW chips, shown in Figure 3.1, were manufactured in the beginning. In the first batch, a-Si layer was covered with a layer of seven-

nanometer-thick Teflon®. One side of the chip was a smooth surface, whereas the other side was a micropillar-structured Teflon® surface. This type of pattern was used because it should provide a superhydrophobic (for more detailed information, see for example [1]) contact with water droplets. The structure was fabricated using typical lithography methods.

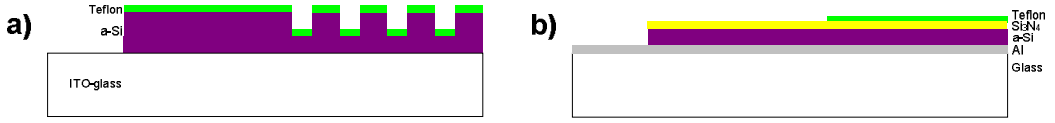

Figure 3.1: Schematics of different OEW chips, a) Teflon® – Structured Teflon® OEW chip with 1.5µm-thick a-Si and 7nm-thick Teflon® layers on top of the ITO-glass (not in scale), b) Teflon® – Si_3N_4 OEW chip, where a glass is coated with a thin aluminium layer (~7nm), 1.5µm-thick a-Si, 12-nm-thick Si_3N_4, and 7nm-thick Teflon® layer on one side of the chip (not in scale).

Structured Teflon® was not used in the second batch. During the process of the second batch, adhesion problems when depositing the a-Si layer on the ITO-glass became significant. It was noticed that there were so huge quality variation between ordered ITO-glasses that even the proper cleaning of ITO-glass did not enable deposition of a-Si. Based on this, it was decided to replace ITO-glass by normal glass coated with a thin aluminum (Al) using sputtering method to provide electrical connection but still maintaining the transparency of the bottom electrode. A 12-nm-thick Si_3N_4 layer was deposited on top of 1.5-µm-thick a-Si layer. After that, 7-nm-thick layer of Teflon® was deposited on top of one side of the chip as illustrated in Figure 3.1b). In the next section, the first initial tests using these surfaces are described.

3.2. Experiments

The purpose of the tests were to experience, can optoelectrowetting be performed with the provided chips. The goal was to achieve evidences, that these set-ups could be used to perform later operations that are more complex, such as droplet manipulation and creation. For this reason, three different initial tests were performed. In the first two tests, Teflon®-Structured Teflon® surface was used. Teflon®-Si_3N_4 chip was used in the third test. The frequency range of applied AC voltage during these first tests, mostly between 150 Hz and 500 Hz, was chosen based on the used frequencies on the OEW-studies [48-53].

3.2.1. Initial contact angle measurement

To investigate the developed surface, a small droplet was pipetted on the surface. Images were taken using a common digital camera [92]. It was noticed that in the first batch, shown in Figure 3.2a) and b), the contact angle of the droplet was only slightly

larger on structured rough Teflon® surface side than on the smooth Teflon® side. On the other hand, the difference between the sides in the second batch could be easily observed as illustrated in Figure 3.2c).

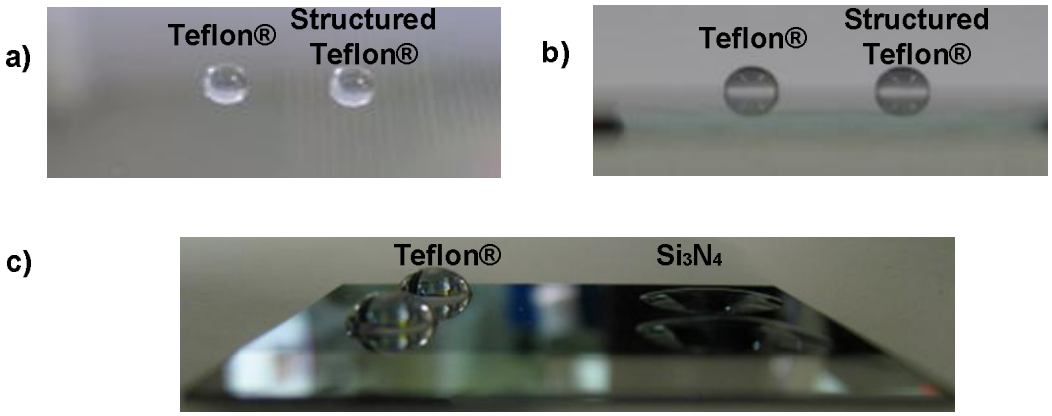

Figure 3.2: Pipetted droplets on the fabricated chips a) an upper view of two DI water droplets on the fabricated Teflon® – Structured Teflon® OEW chip and b) a side view, c) a side view of four DI water droplets on the fabricated Teflon®-Si_3N_4 OEW chip.

Because the purpose of this test was to investigate the behaviour of the droplets on the surfaces, not to precisely define the initial contact angle, no precise contact angle analyses was performed during this experiment. However, it is still easy to notice that the Teflon® surface was not as hydrophobic as it has been reported (typically over 115° for smooth Teflon® surfaces [30; 93]). The reason for that is not clear. It might be, that the surface was somehow contaminated during the tests, or that the roughness of the surface was too high to provide a hydrophobic contact. It has been also reported, that minor alterations in the fabrication and test processes, including a surface preparation protocol and used sample handling technique, may cause significant changes in the properties of the surface, resulting changes in the initial contact angle. For instance, the preparation method will remarkably affect the dielectric strength of a film and how consistent is the coating. It is possible that when using larger voltages, some undetected slow kinetic changes will introduce time-dependent effects to the system. [93] However, tests were performed even though not knowing the original reasons for droplet behaviour on the Teflon® surface.

3.2.2. Reconfigurable valve

The purpose of the first tests was to establish a reconfigurable valve described in Section 2.5.2. For the proof-of-concept test, simple straight microchannels with the width of 1000 µm and height of 250 µm were fabricated by molding polydimethylsiloxane (PDMS) on an existing SU-8 mold. The middle part of the channel was opened to provide an electrical contact for liquid. Two connection holes were punctured on the both ends of the channel to enable connection of tubing from a

pump. The PDMS-channel was then placed on the OEW chip so that the open middle part was crossing both surface regions, the smooth and structured Teflon®. The top ITO-electrode was placed onto the open part to entirely enclose the microchannel. The bottom and top electrodes were connected to power supply to provide electric field inside the microchannel. A connection slice made by PDMS was irreversible bonded on top of the punctured hole on the structured Teflon® side to provide more reliable and stable connection between the microchannel and a house-made pressure source controlled by computer. A droplet of DI water was injected on one connection hole (the smooth Teflon® side) and it was sucked through the channel using negative pressure. The liquid meniscus was monitored from top using a motorized tube microscope (12x Zoom Vision System from Navitar [94]) together with a camera (XCD-X710 from Sony [95]) that was connected to computer.

The hypothesis was that with a certain critical minimum pressure value p_{min}, , a droplet could be sucked towards structured Teflon® side. At the interface, the droplet would be stopped because of the rougher structure Teflon® surface. Without applying any light, a certain pressure increment would be required to move the droplet to the structured Teflon® side. However, if light is applied to the interface (and to structured Teflon® side), these regions would become locally hydrophilic. The result would be that lower pressure increment would be needed in this case. This way, the size of the droplet could be controlled by the size of the light. The schematic of the measurement set-up described above is shown in Figure 3.3a). As mentioned, a similar set-up but using conventional EWOD-system to control continuous flow was presented earlier in [81].

The problems related to the fabricated surfaces where observed during the first measurement without neither light nor voltage. The liquid did not stop at the interface when applying the minimum negative pressure to move the liquid, and therefore the idealized light-based reconfigurable valve could not be even tried. The reason for this was that there was not remarkable change of the wetting properties between the surfaces. The liquid moved on the structured Teflon® with the same minimum pressure as on the smooth Teflon®.

The problems related to the fabricated surfaces where observed during the first measurement without neither light nor voltage. The liquid did not stop at the interface when applying the minimum negative pressure to move the liquid, and therefore the idealized light-based reconfigurable valve could not be even tried. The reason for this was that there was not remarkable change of the wetting properties between the surfaces. The liquid moved on the structured Teflon® with the same minimum pressure as on the smooth Teflon®.

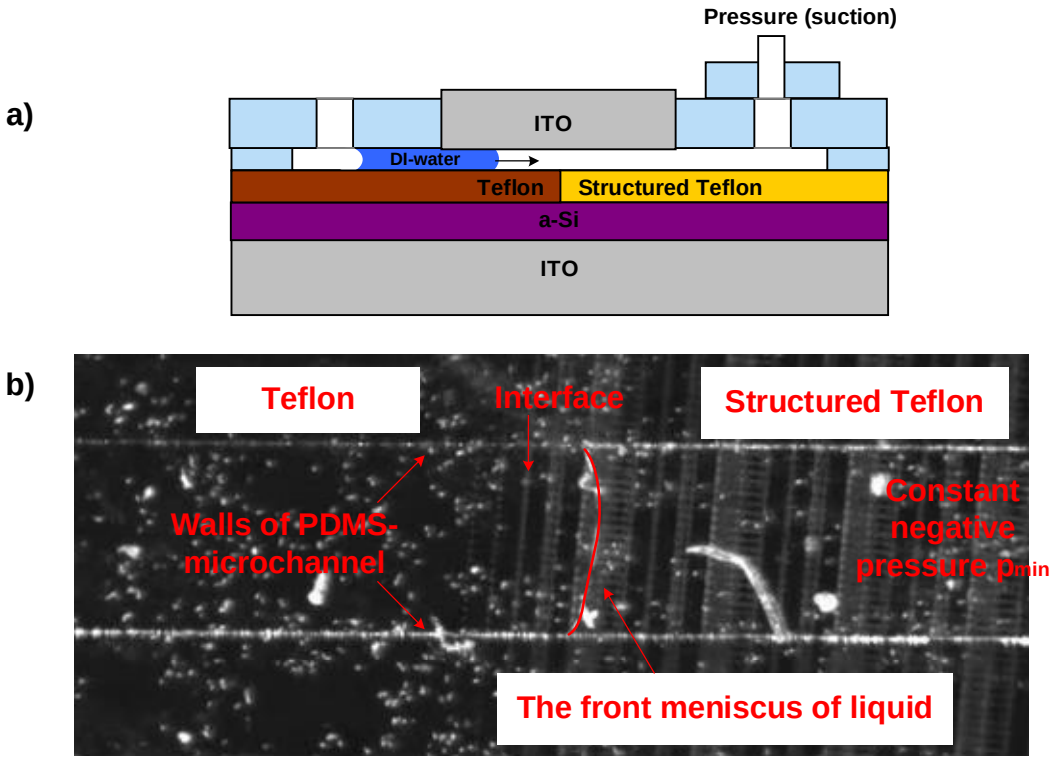

Figure 3.3: a) A schematic of the proof-of-concept test of the reconfigurable valve, b) testing Teflon®-Structured Teflon® interface. As can be seen, the front meniscus enters into the structured Teflon® side even though the negative pressure is kept constant.

Liquid movement with the same minimum pressure was confirmed with another test using a closed PDMS-microchannel (same dimension) that was bonded on the same surface than in the previous test. As previously, no electrical actuation was used to manipulate liquid. Again, a minimum negative pressure was applied to move the liquid from the smooth Teflon® side towards the structured side. It was observed, that even though the velocity of the liquid decreased at the interface, it did not stop. Deceleration was noticed because the liquid had to fill the first capillary structure (whole channel width) before bursting to the second structure, as shown in Figure 3.3b).

3.2.3. OEW proof-of-concept test with a sessile droplet

A simple optoelectrowetting proof-of-concept test, a set-up shown in Figure 3.4, was also performed using the same chip that was used in the previously presented reconfigurable valve experiment. The goal was to inspect, is it possible to change the contact angle of a sessile droplet with the current OEW chip and used DLP-light. If successful, the test would proof the workability of the used set-up shown in in Figure 3.4. A droplet of DI water was placed on top of Teflon® layer. The droplet was inspected using a conventional digital camera (IXUS 800 from Canon Digital [92]). AC voltage with different signal shapes (rectangular and sine) and frequencies between 150

Hz to 300 Hz with point-to-point voltages ranging from ± 10 to ± 75 V created by a signal generator (33120A from Agilent [96]) and an amplifier (SVR-150 from Piezomechanik GmbH [97]) were applied to the circuit. Triggering light from a conventional DLP-projector (LP420 from InFocus [98]), directed upwards using a right angle mirror, was used to illuminate an area larger than the droplet. It was expected, that the contact angle of the droplet would decrease everywhere symmetrically, as idealized in Figure 3.4c) for a perfectly smooth Teflon® surface.

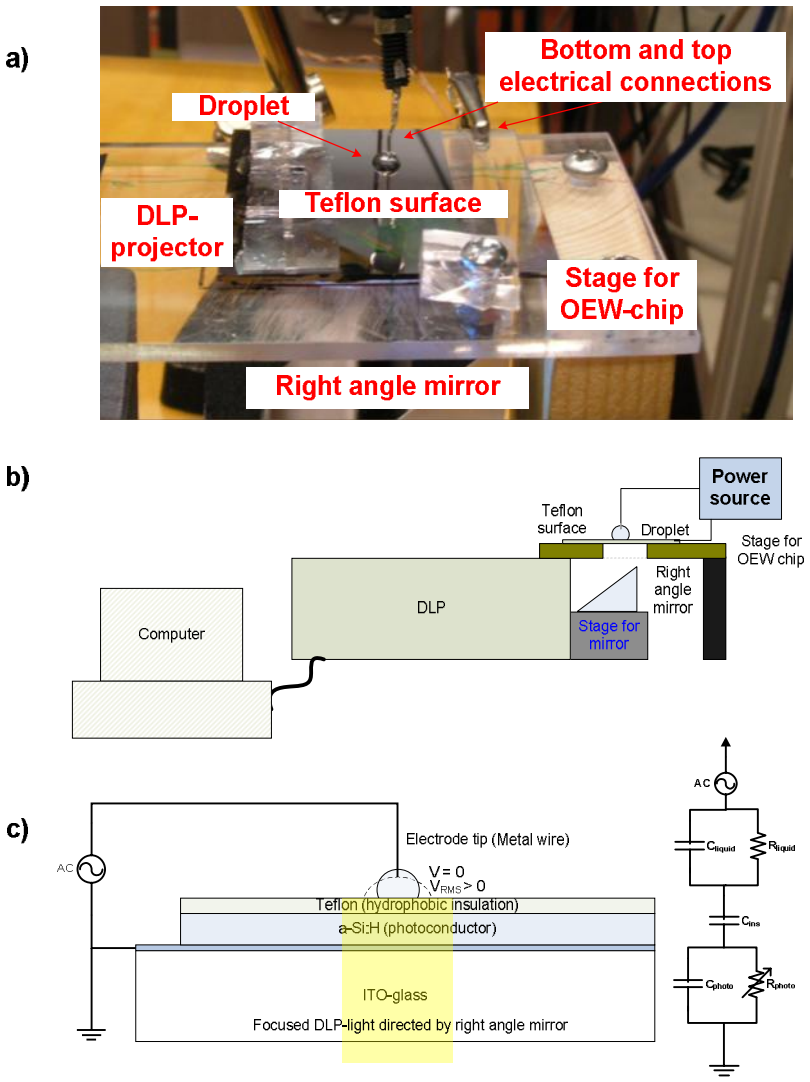

Figure 3.4: a) Test set-up for OEW proof-of-concept test, b) a schematic of the set-up, and c) a closer view.

During the performed test, no significant droplet spreading was noticed at any used voltage. Some minor contact angle changes were observed when higher voltages (> 42

V) were applied. However, this happened after gas bubbles were formed inside the droplet, probably because of electrolysis.

The conclusion for that these tests were not successful is that the hydrophobic properties of the Teflon® layer were not high enough to provide optoelectrowetting. It also might be, that the surface had contaminated for some unknown reason. The initial contact angle during the measurement was observed to be slightly below 90 degrees, even though originally it was noticed to be remarkably higher straight after fabrication (data not shown).

3.2.4. Testing Teflon® – Si3N4 OEW chip with a sessile droplet

Based on the test described in the previous section, it was noticed that the micropillar structure did not provide as large initial contact angle as it was planned. For this reason, the second batch of OEW chips having with half Teflon® half Si_3N_4 top layer was fabricated as was shown in Figure 3.1b). The idea was to use this batch to perform an OEW proof-of-concept test with a sessile droplet that was not successful with the previous design. It was also decided to try different light sources (the used DLP-projector and a laser), a smaller volume (from 100 µl down to 2 µl) and different frequencies (from 500Hz sine to continuous DC-voltage) in these experiments to observe their relevance for the obtained results.

With the second batch, as was shown in Figure 3.2c) the difference between droplet located on Teflon® and Si_3N_4 sides can easily noticed. However, even though Si_3N_4 side is very hydrophilic, Teflon® side is only barely hydrophobic as shown in Figure 3.5. This remarkably restricts the maximum achievable electrowetting effect.

Figure 3.5: A barely hydrophobic Teflon® surface (left) and a very hydrophilic silicon nitride surface (right).

When optoelectrowetting tests were performed, rather large voltages up to over 70V were used. First, optoelectrowetting was tested with DI water droplets (50-100µl) using the DLP-light [98]. The system set-up with the DLP-light is shown in Figure 3.6a). 500 Hz sine signal with amplitude ranging from 15 to 45V was applied without any noticeable electrowetting effect on the droplet. When voltage was increased to 75V, the surface was destroyed as can be seen in Figure 3.6b).

Another test with the same chip using a smaller droplet volume (20 µl) was performed. In these experiments, DI water was replaced by more conductive isotonic sodium chlorine (NaCl, 9mg/ml, 0.154 mol/l) liquid because it was expected to enhance the electrowetting effect. The experiments were performed by applying 500 Hz sine with amplitude of 7.5 V using the same the DLP-projector as previously and a laser (1

mW, 675 nm, M5L/10 from MEL Mikroelektronik GmbH [99]) as a light source to illuminate one side of the droplet. No noticeable electrowetting effect was observed. However, because of NaCl has a lower impedance than DI water, electrolysis occurred with lower voltages as can be noticed in Figure 3.6c) and d). It has been suggested that a breakdown of dielectric layer (a-Si in this case) is related to earlier breakdown of thin topcoat (Teflon® in this case) [1]. Another reason might be related to Teflon® surface, which was noticed to be quite rough. It might be that at the vicinity of a structural inhomogeneity, there was some amplified anomalous electric field strength. This could have been so large that the Teflon® coating could not withstand it. To conclude, this question is still unclear and requires further studies.

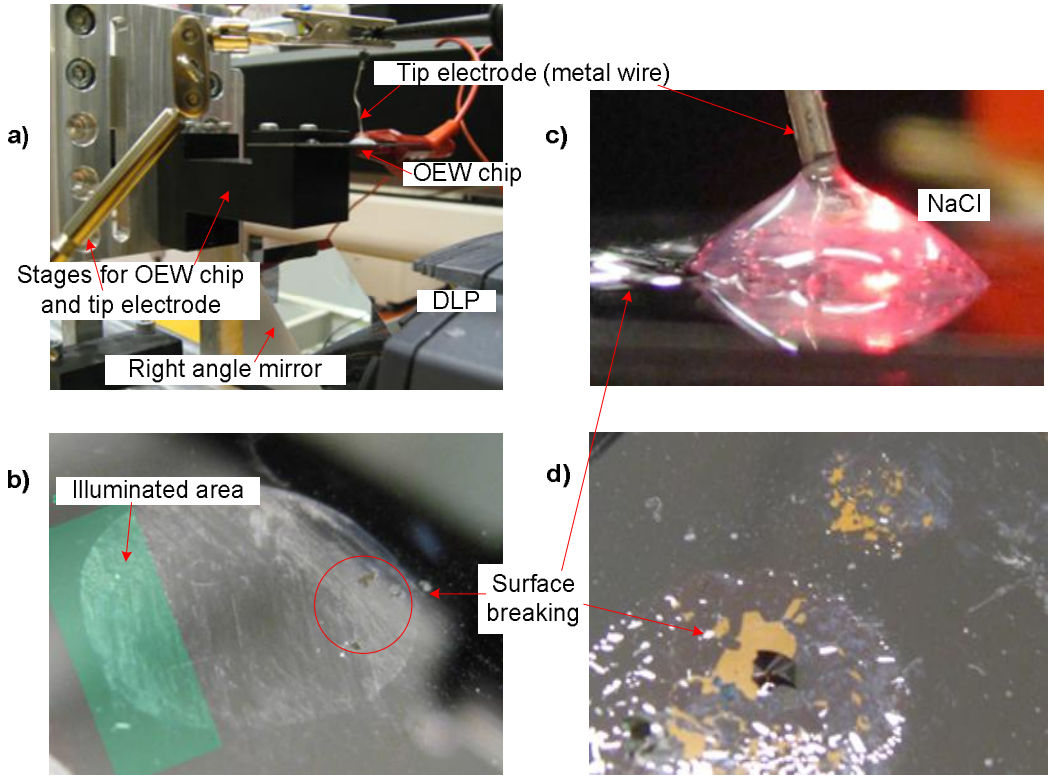

Figure 3.6: a) System set-up, b) the breakdown of the surface with DI water, c) electrolysis with NaCl (bubbles inside the droplet) and d) the breakdown of the surface with NaCl.

The experiments showed that the initial shape of the droplet was not spherical as it was assumed. This was mostly because of too large droplet volume, and might affect also the contact angle of the droplet. A so-called dimensionless Bond number gives the rationbetween gravitational and surface tension forces. If Bond number is remarkably small (~0.1), gravitational force can be neglected. It is calculated by [1]:

$$Bo = \frac{\rho * g * r^2}{\gamma} \tag{3-1}$$

where ρ represents the density of the liquid, g is acceleration of gravity, r is the radius of the droplet and γ is the surface tension of the interface (liquid-air in this case). For the liquid used here (DI water and NaCl), and assuming contact angle to be 90°, using values ρ = 1000 kg/m^3, g = 9.81 m/s^2, γ = 0.072 N/m, gives Bond number around 0.13 for a 2 µl-droplet that was chosen for the new droplet volume. When Bond number is relative low as in this case, it can be assumed that the droplet has a spherical shape. [1] For this reason, next tests were performed using 2 µl droplets.

The first goal of the proof-of-concept test was to observe any electrowetting effect. For this reason, DC-voltage without illumination was applied to NaCl droplet to enhance electrowetting on each side of the droplet [48]. This experiment is shown in Figure 3.7.

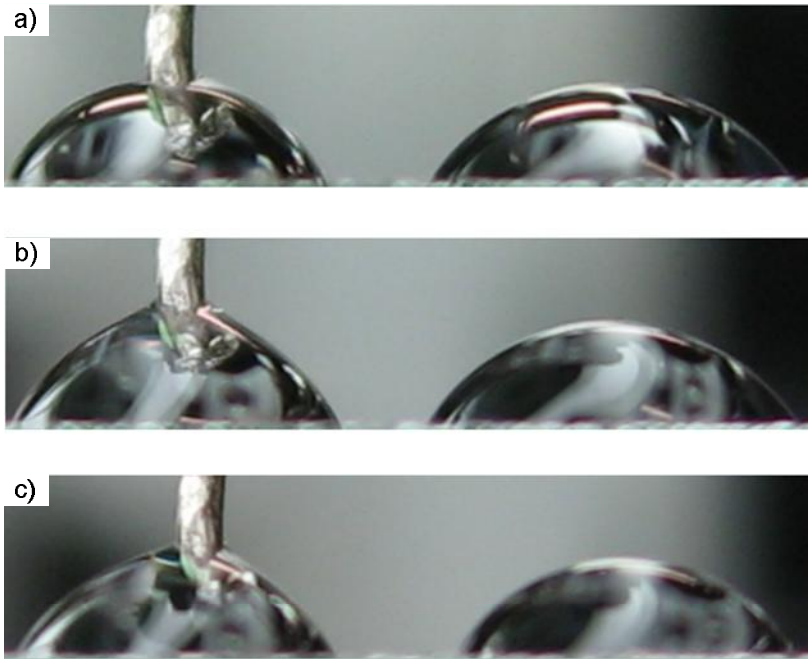

Figure 3.7: a) 2 µl DI water droplet on initial state without any applied voltage, b) the droplet after one minute of 45V (DC) treatment, and c) a reference droplet after one minute without any voltage showing similar shape.

Even though the shape of the droplet shown in Figure 3.7 changed slightly, it was not because of electrowetting effect but as a result of capillary effect on the tip electrode. This can be easily noticed in Figure 3.7c), where the tip electrode was introduced to the droplet but without applying any voltage. Furthermore, when higher voltage was applied, the surface was destroyed similarly than it was previously reported and shown in Figure 3.6d).

3.2.5. Conclusion

Based on the experiments that were performed using the chips fabricated in the project, the unworkability of the optoelectrowetting was obvious. During the tests, the origin of optoelectrowetting was still partly unknown, for instance the reasons for dielectric breakdown even with very low voltages were not understand. To obtain better knowledge about the underlying physic of these experiments, it was decided to model the test set-up to discover the reasons for unworkability of the performed tests. The modelling process is described in the next section.

3.3. OEW modelling process based on the previous studies

As reported in Section 0, no successful OEW phenomena were achieved during the first experiments. It was decided to build a model of the used OEW device based on the parameters shown in Figure 3.8 to discover the reason for the result that were obtained. The model should describe the situation of the OEW proof-of-concept test with a sessile droplet as was reported in the previous section.

The model consists of three parts, which are explained next. The droplet is modelled as a parallel combination of a capacitive and a resistive part whereas for the insulator layer the combination of two capacitive parts (7nm Teflon® and 12nm Si_3N_4) was used. Even though these layers are relatively thin, the capacitance of the electrical double layer (EDL) is neglected because it would not remarkably change the total capacitance of the insulator layer. This is based on the Helmholtz simplifying assumption where the counter-ions are located at a constant distance from the surface, the thickness of EDL is only a few nanometers [1; 3; 21]. The bottom photoconductive a-Si layer is modelled as a parallel combination of capacitive and resistive part, where the latter is modelled as an adjustable resistor depending on the intensity of illuminated light.

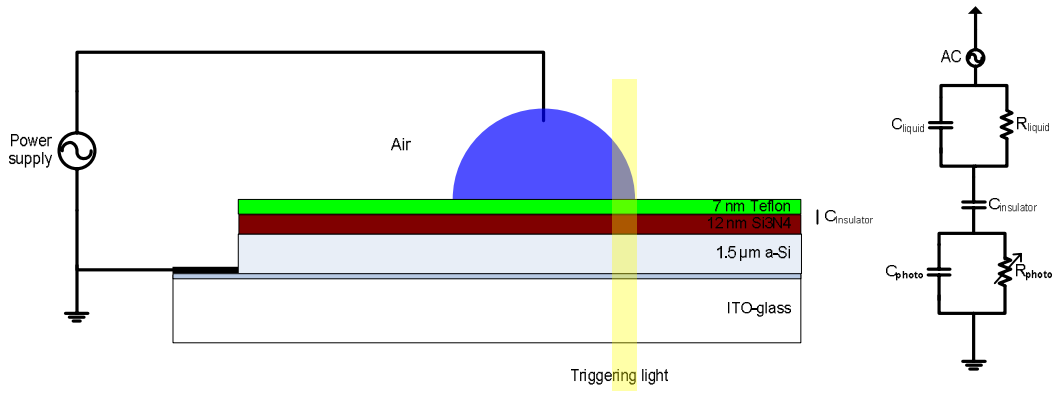

Figure 3.8: A schematic of initial OEW tests (not in scale) and the equivalent circuit of the experiment.

To understand the working mechanism of the set-up presented here, each component has to be valued. Before this validation, it was decided to investigate the models given in publications [48-53]. The goal was to inspect, is it possible to model these systems as they have been reported, assuring that the necessary knowledge about OEW-mechanism have been achieved thus enabling to model the own system properly. The modelling processes of three different OEW publications [48; 50; 52] are described next, whereas the validation of the own model is illustrated in Section 0.

3.3.1. Grid-based optoelectrowetting device

In the first OEW-publication [48], two simulations (presented in Figures 4 and 8 in the study) can be modelled. The system set-up, shown in Figure 3.9, uses an electrode grid consisting of over 20 000 electrodes. The simulated voltage drop over the insulator layer (silicon dioxide, S_iO_2) with different photoconductive ratio c ($c = 1$ represents dark state, $c = 10$ ten times higher conductivity of the photoconductor layer) when applied voltage was $U = 100V$ is shown in Figure 3.10a). The voltage drop is calculated simply by comparing the impedance of the insulator layer to the total impedance of the system, as was described in Equation (2-18). The required parameters for the modelling, such as resistance and conductance of water (R_w and C_w in the publication, expressed as R_{liquid} and C_{liquid}, respectively, in this thesis) or photoconductive layer (R_{asi} and C_{asi} in the publication, expressed as R_{photo} and C_{photo}, respectively, in this thesis) or conductance of the insulator layer (C_{oxide} in the publication, expressed as C_{ins} in this thesis) were not given. For this reason, it was required to define these. The hypothesis was that each capacitive part could be modelled as a parallel capacitance, for instance, the liquid (DI water) would have an area equal to A (depending on the choice) while height being equal to gap (500µm). The resistive part of the material, expressed as R, and the parallel plate capacitor with capacitance C and reactive impedance X_c, can be calculated using equation:

$$C = \frac{\varepsilon_0 * \varepsilon_d * A}{d}$$
$$X_C = \frac{1}{j * \omega * C} = -j\frac{d}{\omega * \varepsilon * \varepsilon_0 * A} \tag{3-2}$$
$$R = \frac{1}{\sigma} * \frac{d}{A}$$

where ε_0 , ε_d are the permittivity of the vacuum and the relative permittivity of the material, respectively, with the thickness d, ω is the angular frequency of the applied electric field, and σ is the conductivity of the material. The total impedance Z and the absolute value Z_{abs} of a layer modelled as a parallel combination of capacitor C and resistant R (liquid and photoconductive layers) can be understand as a parallel RC circuit and can be calculated using equations:

$$Z = R \parallel X_c = \frac{R * X_c}{R + X_c} = \frac{R * \frac{1}{j\omega C}}{R + \frac{1}{j\omega C}} = \frac{R}{1 + j\omega RC} = \frac{R - j\omega R^2 C}{1 + (\omega RC)^2}$$

$$|Z| = \sqrt{(Z(\mathrm{Re}))^2 + (Z(\mathrm{Im}))^2} = \sqrt{\left(\frac{R}{1+(\omega RC)^2}\right)^2 + \left(\frac{-\omega R^2 C}{1+(\omega RC)^2}\right)^2} \qquad (3\text{-}3)$$

$$= \frac{\sqrt{R^2\left(1+(\omega RC)^2\right)}}{1+(\omega RC)^2} = R\frac{\sqrt{\left(1+(\omega RC)^2\right)}}{1+(\omega RC)^2} = \frac{R}{\sqrt{\left(1+(\omega RC)^2\right)}}$$

Both the total impedance of the system Z_{tot}, when a thin hydrophobic Teflon® layer is neglected, and the voltage drop over insulator layer U_{ins}, are then calculated by combining Equation (2-18) and Equation (3-3):

$$Z_{tot} = Z_{photo} + Z_{ins} + Z_{liquid}$$

$$= \frac{R_{photo}}{\sqrt{\left(1+(\omega R_{photo} C_{photo})^2\right)}} + \frac{1}{j\omega C_{ins}} + \frac{R_{liquid}}{\sqrt{\left(1+(\omega R_{liquid} C_{liquid})^2\right)}}$$

$$U_{ins} = \frac{Z_{ins}}{Z_{tot}} * U = \frac{\frac{1}{j\omega C_{ins}}}{\frac{R_{photo}}{\sqrt{\left(1+(\omega R_{photo} C_{photo})^2\right)}} + \frac{1}{j\omega C_{ins}} + \frac{R_{liquid}}{\sqrt{\left(1+(\omega R_{liquid} C_{liquid})^2\right)}}} * U \qquad (3\text{-}4)$$

where U is the RMS-value of the applied electric field. Using the equations presented here, the voltage drop over the insulator layer was calculated. When trying to simplify the model, the important issue is that how each layer should modelled. The main task is to define, what is the size A for each layer that should be used. Different methods were tried before reaching the goal. Given properties of each layer (photoconductor, insulator and droplet), such as conductivity and permittivity, were used whenever they were given.

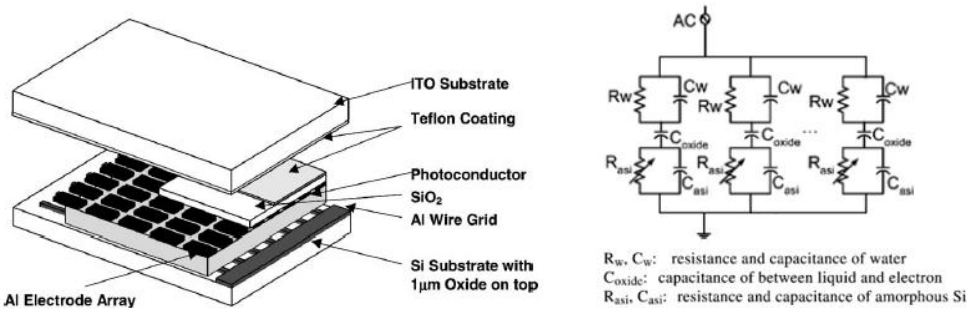

Figure 3.9: A schematic structure of the OEW device and its equivalent circuit [48].

The first method to model the voltage drop over the insulator layer as shown in Figure 3.10a) was performed by using an area of one electrode (50 µm x 100 µm [48]) as *A* to represent each layer. The result of this is shown in Figure 3.10b). As can be seen, it is not even close to the reference result. It can be concluded that publication [48] did not model the area *A* as the area of one electrode. Also value of $c = 80$, which is based on their photoconductive measurement, is plotted because it will be used later in contact angle measurement as shown in Figure 3.12.

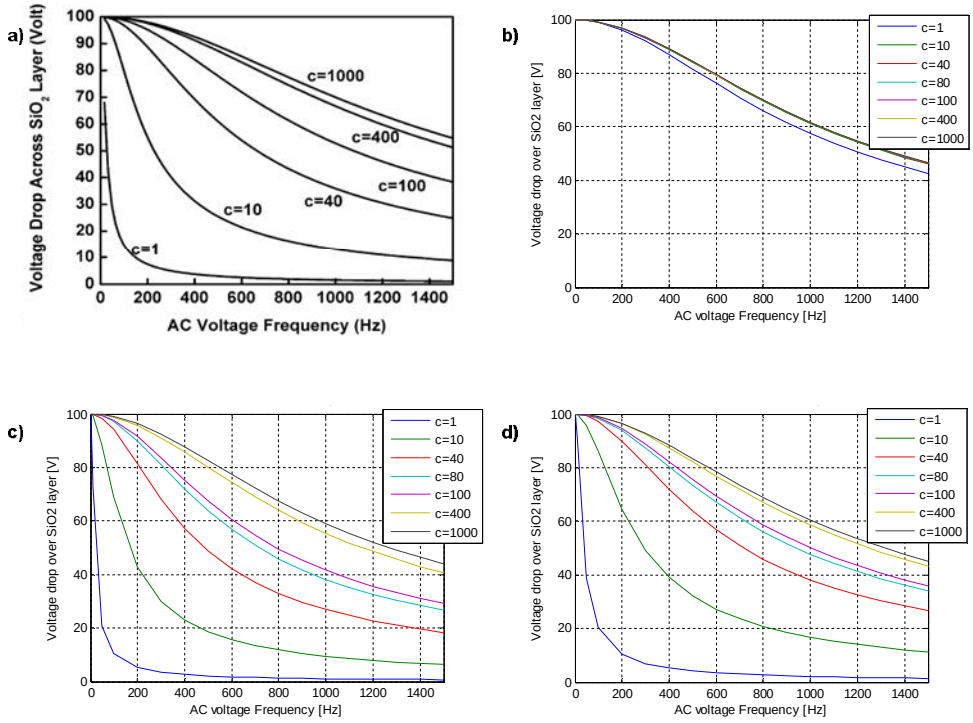

Figure 3.10: a) Published simulated voltage drop over the insulator layer [48], b) the first own simulation result using one electrode area for each layer,, c) the second method using one electrode area representing photoconductive layer and other modelled as an area of the droplet, d) the last model using a parallel combination of the two electrode areas for photoconductive layer. See text for the details.

Another modelling was performed using one electrode area for the photoconductive layer and modelling the insulator and the droplet layer as the size of the droplet. All the parameters were not given to simulate the process shown in Figure 3.10a), for example the used volume of the droplet in the simulation part was not reported. The diameter of the droplet is 2 mm, which was used here for calculating the area of droplet. The droplet was idealized as following: the bottom was assumed to be circular, and the height of the droplet was as the used gap (500 µm) with a rectangular cross-section as shown in Figure 3.11. The area of a cylinder shape droplet, expressed as a droplet contact area A_c,

is simply calculated by $A_c = \pi*(diameter/2)^2$. As can be seen in Figure 3.10c), this method gives remarkably better results.

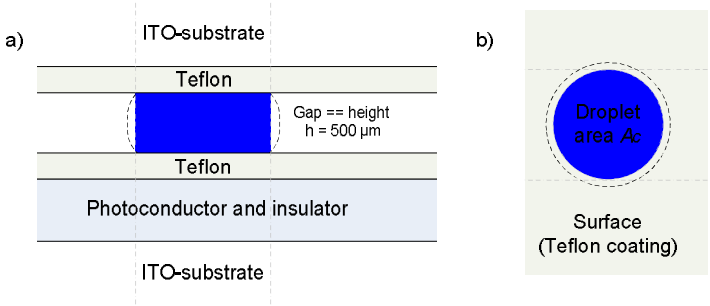

Figure 3.11: A schematic of the droplet simplification. Grey lines are representing the area that is used for impedance calculation of a circular droplet with height of 500µm and having a rectangular side shape, a) Side-view, b) top-view.

The third model, results shown in Figure 3.10d), uses a similar method to the second model, except here the photoconductive layer is modelled as a size of two electrodes, $A = 2*A_{electrode}$ meaning that illuminated area is two times the are of the previous model. Instead of one parallel RC circuit (R_{photo} and C_{photo}), there are now two of these in parallel, resulting that the total value of the resistive part will be $0.5xR_{photo}$ and that the total capacitance is two times the initial value C_{photo}. As it can be noticed, this method gives even better result. If more electrode areas would be multiplied together, the difference between own simulation and the published could be decreased. The conclusion is, that the voltage drop has been simulated using the droplet area for droplet and insulator layers, and electrode areas (depending on the light spot size) for photoconductive layer. To further verify the own calculations, the next task was to model the published contact angle as a function of light intensity plot (Figure 8 in [48**]**) shown in Figure 3.12b). However, in the paper it was mentioned only, that 70 V (assumed to be RMS-value) was applied, not which frequency was used. Therefore, it is required to calculate, which frequency is used to achieve a new contact angle of 75° using Equation (2-20). The result, as shown in *Figure 3.12*a), indicates that 575 Hz of 70 V is needed to change the initial contact angle $\theta_0 = 105°$ to $75°$ when the conductivity of the photoconductor is increased 80x times ($c = 80$) as it was measured with light intensity of 65 mW/cm^2 [48**]**.

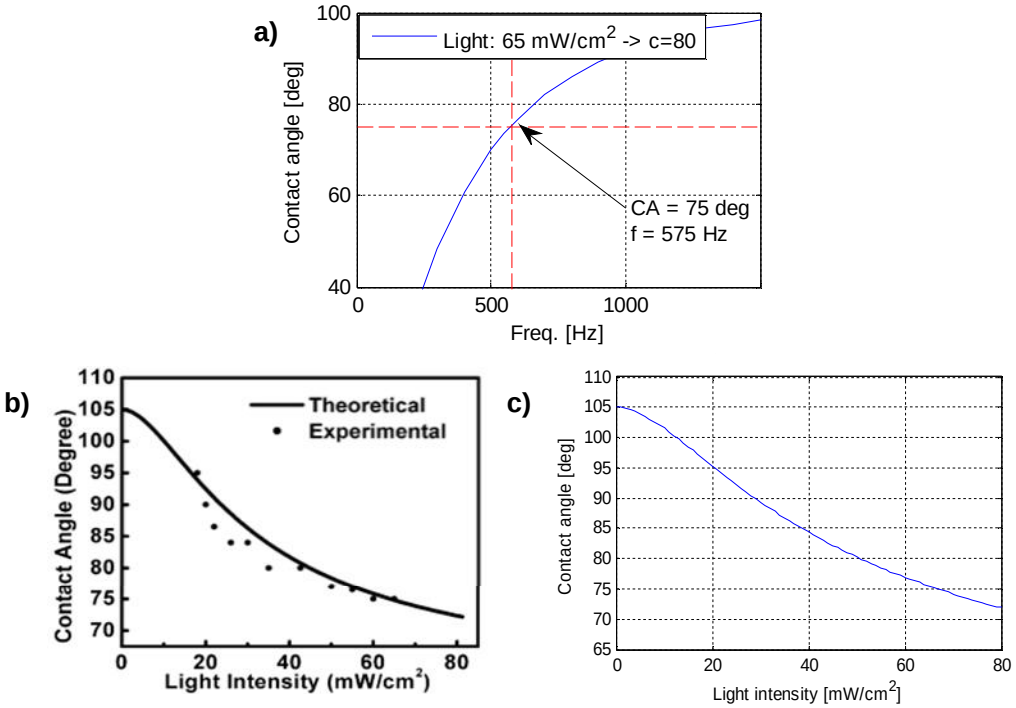

Figure 3.12: Contact angle with different light intensities. a) Defining the used frequency of the applied voltage of 70 VRMS, b) Published data [48], c) calculated data using a size of an electrode for the photoconductor layer and a size of a droplet for the other layers. See text for the details.

To model Figure 3.12b), the photoconductor layer is modelled as the size of one electrode whereas as other layers are modelled based on the droplet size, using the same method that was explained earlier and shown in Figure 3.10c). The contact angle as a function of the light intensity when applied voltage is 70 V_{RMS} (575 Hz) is plotted in *Figure 3.12*c). There are minor differences between the simulated and published data, but it can be confirmed that these are not remarkable. The major differences might come with some used values, which were not given in the paper, for example because of the frequency was not given, it had to first calculated as was presented in Figure 3.12a). Based on the results, it can be concluded that the published data [48] was successfully modelled. However, there is still a question how the area of photoconductor layer should be modelled when the light is applied. This issue will be discussed more later in this and next sections together with other publications.

3.3.2. Open optoelectrowetting device

Open optoelectrowetting experiment [52], a schematic shown in Figure 3.13, was also decide to be modelled. In this set-up, droplets are controlled by triggering the electrodes located on the same plane using the same method than the open electrowetting devices described in Section 2.2.4.

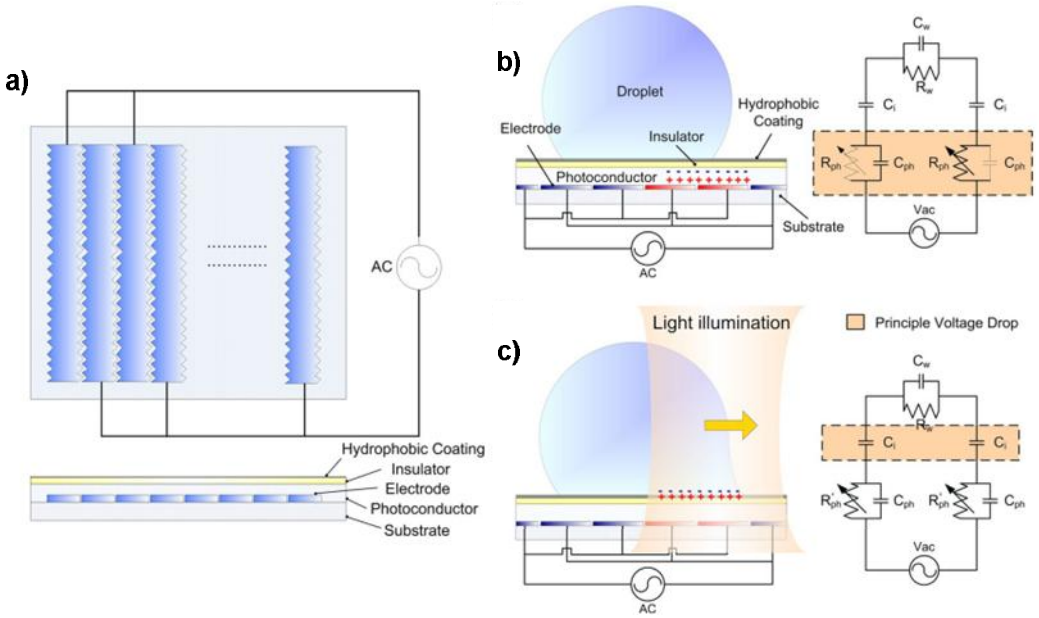

Figure 3.13: Open optoelectrowetting device, a) a schematic of the layout, b) and c) working mechanism of the device [adapted from 52].

It was noticed that there is a mistake in the given equation (Equation 1 in the paper) for voltage drop (expressed as U_{OEW} in the paper) because a resistive part of a photoconductor and a droplet is missing from divisor. There will be a parallel combination of resistive and capacitive part. Using Equation (3-3) and for example [50], original and corrected equations to calculate U_{OEW} are given in Equation (3-5).

$$U_{OEW} = U * \frac{\frac{1}{j\omega C_i}}{\frac{2}{j\omega C_i} + \frac{R_w}{1 + j * \omega * C_w} + \frac{2 * R_{ph}}{1 + j * \omega * C_{ph}}}$$

$$U_{OEW\_corrected} = U * \frac{\frac{1}{j\omega C_i}}{\frac{2}{j\omega C_i} + \frac{R_w}{1 + j * \omega * C_w * R_w} + \frac{2 * R_{ph}}{1 + j * \omega * C_{ph} * R_{ph}}} \quad (3\text{-}5)$$

It was observed that the simulations results, illustrated in Figure 3.14a), were performed using the given incorrect equation. To compare the results, the voltage drop over the insulator layer was calculated in this work using the equation given in the publication [52].

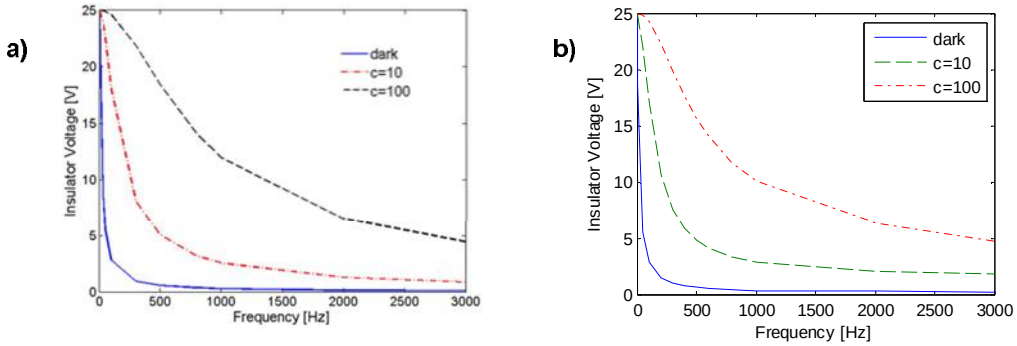

Figure 3.14: Voltage drop over one insulator layer (expressed as C_i in [52] as shown in Figure 3.13); a) published [52], and b) calculated data. See text for the details.

Some crucial parameters of the model are not given in the paper. Therefore parameters given in other publications were used in the simulations: conductivities of the droplet (DI water) and the photoconductor (dark state) were 10^{-3} and 10^{-7} mS/cm, respectively. Relative permittivities of the droplet, photoconductor and insulator were chosen to be 72, 11.8 and 4, respectively. Furthermore, based on Figure 3.13b) and c), a hypothesis is that the insulator and the photoconductor layers could be modelled with an area equal to half of the droplet area. The droplet is assumed to have a shape of a perfect hemisphere (contact angle being 90°) with a radius of 300 µm, resulting the volume of around 57 nanoliters. When thin Teflon® layer is neglected, the calculated result in Figure 3.14b) shows similar response than the published data. The most probable reason for differences between the results is due to the assumptions for the parameters that were not given.

3.3.3. Continuous optoelectrowetting device

A so-called continuous optoelectrowetting device [50], a schematic shown in Figure 3.15a), was chosen to be modelled because the layout of this device is very close to chips that were fabricated during this project. Therefore, if assuming that the published model is correct, being able to remodel this would confirm that own model is proper and could be used for modelling of the OEW system. Since the used volume of the droplet was not given direcly in the paper, it is assumed to be 50 picoliter because this volume was used in the experimental part of the paper. With a gap of 10 µm and initial contact angle of 118°, the droplet contact area is calculated to be ~4870 µm^2. Used simplified method to model the droplet is shown in Figure 3.15d) and e). This calculated area is then used in the modelling process, as will be explained next.

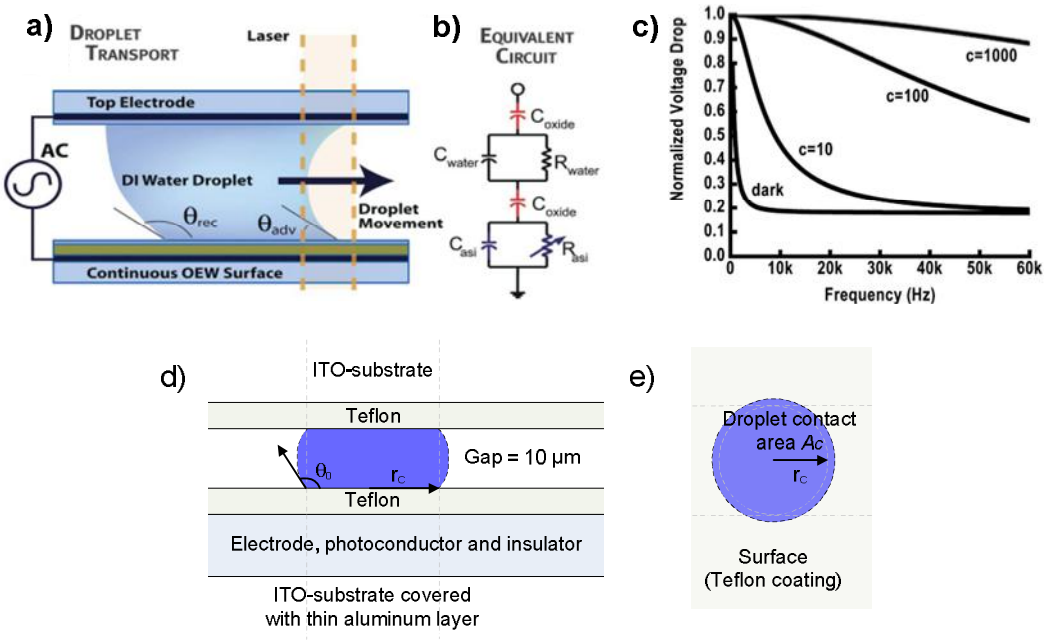

Figure 3.15: a) A schematic of droplet movement by optical beam, b) an equivalent circuit, c) a simulated voltage drop across two insulator layers [50]. d) A side-view of a contact radius that is used for impedance calculation of a circular droplet with a height of 10 µm and having an initial contact angle θ_0 = 118°, and e) a top-view where grey circle is presenting the area of the droplet used for calculations.

The paper provides a normalized voltage drop as a function of frequency for different photoconductive ratios. The normalized voltage drop over the insulator layers is calculated by dividing U_{ins} in Equation (3-4) by U. To verify the normalized voltage drop over the both insulator layers (in this set-up, also the top electrode is covered with the insulator layer) shown in Figure 3.15c), different methods have been used. These are shown in Figure 3.16 when Teflon® layer is neglected and light size is assumed to be ~310 µm^2 based on the given diameter of 20 µm and assuming it to be a circular.

In the first model, the calculated droplet contact area is used for each layer. When light is applied, the resistive part of the photoconductive layer is modelled as a parallel combination of illuminated and dark resistances. This issue will be discussed more in the next section. Based on the result presented Figure 3.16a), this method does not give similar response to original data when light is applied. For this reason, the hypothesis was to model the photoconductor layer as a size of the light beam while other would be still modelled as the droplet contact area. Using this approach, the resistive part of the photoconductive layer would be modelled as a resistance, which value is directly proportional to ratio of *c = photoconductive / dark conductivity*. However, as shown in Figure 3.16b), this model does not represent the published result. During the dark state, the impedance of the insulator layer will be remarkably lower than the photoconductor layer when the applied frequency is higher than a few hundred of hertz. Based on this result, the third method is to model the photoconductor and the insulator layers as a size

of the light, and using the droplet contact area for the liquid layer. As shown in Figure 3.16c), neither this method will give the comparable result with larger photoconductive values and higher frequencies, mainly because the impedance of the droplet will be lower in this case. The result is that the main voltage drop with high *c* will be over insulator layer even for higher frequencies because the impedance of the insulator layer will overcome the impedance of the droplet.

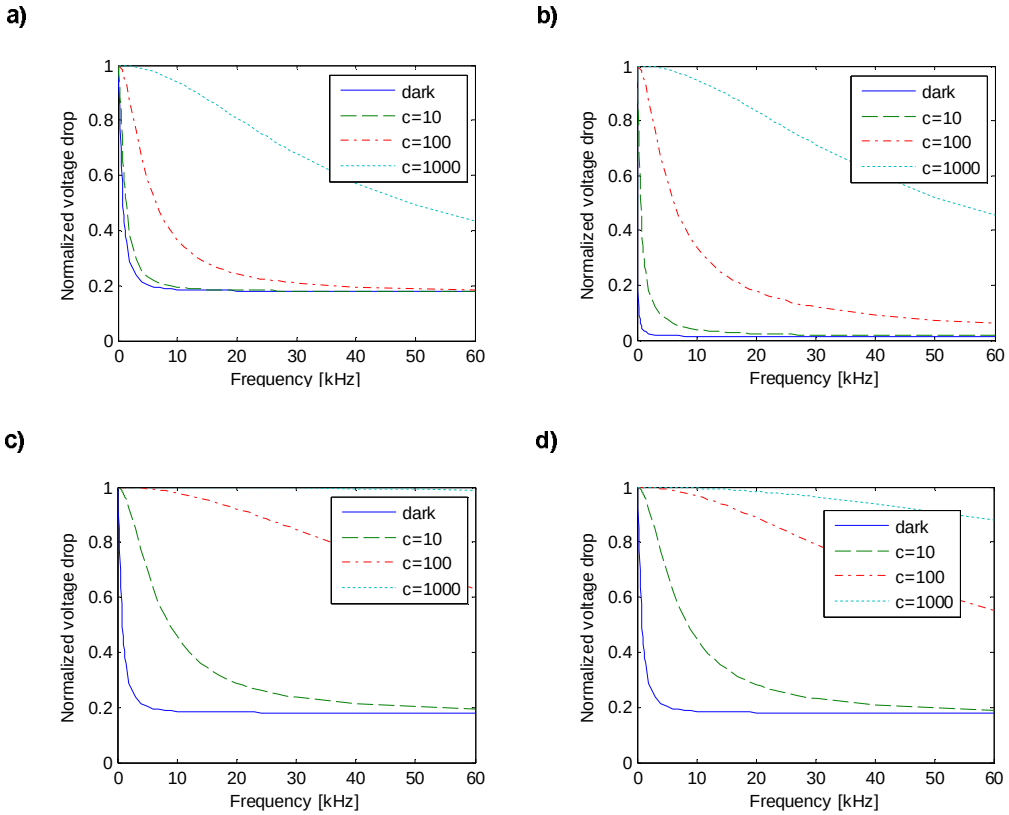

Figure 3.16: Calculated voltage drops over <u>two</u> insulator layers using: a) the droplet area size for each layer, b) the droplet area size for the droplet and the insulator layer and the beam size for the photoconductor layer, c) the droplet area size for the droplet and the beam size for the photoconductor and the insulator layers, d) the beam size for each layer. See text for the details.

Based on the previously presented methods, in the last model shown in Figure 3.16d), each layer is assumed to be the size of light. As it can be seen, this model is close to published data. It can be concluded that modelling the third publication is successful using the last presented method. However, the big question mark here is that is it valid to model each layer as a size of the applied light as it has been done. Especially, how valid is the presented model if only the dark state is concerned?

3.3.4. Conclusion

Some devices presented in the literature together with an own set-up were inspected in this section. The goal was to model these OEW devices to understand the OEW mechanism properly. However, at the moment no general agreement exists on how an OEW device should be modelled. While optoelectrowetting is a relative new phenomenon, the number of papers covering the concept is limited and the provided theory is not comprehensive. Furthermore, based on the own analysis of previous publications, the reporting of the used models is insufficient; for example, the method to calculate the voltage drop over the insulator layer in OEW devices is not identical in every study. Secondly, compared to EWOD-modelling, many important parameters required for calculations are usually missing, and some simplifications without any proper explanations have been done. However, the own results were most of the time comparable with the reference material. The main problem that was encountered is that how each layer in OEW device should be modelled to develop an equivalent circuit presented in many publications. Especially it seems to be unclear how the photoconductor and the insulator layers should be presented during the dark and illuminated states. This issue will be discussed in the next section during the validation of an own OEW device where the proposed modifications for the optoelectrowetting model are given.

3.4. Modelling of own OEW device

Based on the work reported in the previous section, the key issue is how each layer of the OEW device should be presented in the equivalent circuit. It was noticed, that the most used method is to use one area size for each layer in both, illuminated and dark, states. This simplification has been used because it highlights the effect of illumination. However, this model is unable to explain satisfactorily why the same area can be used with and without the illumination. For this reason, in this thesis the hypothesis is that each layer should be modelled using the size of the droplet. This new method is used because the surrounding air is assumed to be perfectly insulating, therefore the electrical circuit will be created only through liquid as shown in Figure 3.17. In this new proposed model, the resistive part of the photoconductive layer is modelled as a parallel compination of the resistances of the dark and the illuminated areas. The modelling process, where each layer is modelled using proper resistor and parallel-plate capacitor values, is described in more details next.

3.4.1. Modelling process

Impedance of each component in a circuit consisting of resistors and capacitors, commonly named as a RC circuit, can be calculated using Equations (3-2) and (3-3). In this model, the resistive part of photoconductive layer is modelled as a parallel combination of two, illuminated and dark, resistances. These are expressed as R_{photo_light}

and R_{photo_dark}, respectively, as shown in Figure 3.17b). Using Equation (3-6), total value of the resistive part of the photoconductor with the thickness d and the dark conductivity σ can be calculated with and without light.

$$
\begin{aligned}
&R_{photo\_tot\_no\_light} = \frac{1}{\sigma} * \frac{d}{A_{liquid}} \\
&A_{dark} = A_{liquid} - A_{light} \\
&R_{photo\_light} = \frac{1}{\sigma * c} * \frac{d}{A_{light}}, R_{photo\_dark} = \frac{1}{\sigma} * \frac{d}{A_{dark}} = \frac{1}{\sigma} * \frac{d}{A_{liquid} - A_{light}} \\
&R_{photo\_tot\_light} = R_{photo\_light} \parallel R_{photo\_dark} \\
&= \frac{R_{photo\_light} * R_{photo\_dark}}{R_{photo\_light} + R_{photo\_dark}} = \frac{d}{\sigma} \frac{1}{(c-1) * A_{light} + A_{liquid}}
\end{aligned}
\tag{3-6}
$$

When no light is applied to the system, the dark area of the photoconductor is equal to the contact area of the droplet A_c, and there will be only one resistance, expressed as $R_{photo\_tot\_no\_light}$, as illustrated in Figure 3.17a). It is assumed that a uniform light with a size of A_{light} is directed to the droplet area, resulting that the dark area A_{dark} is equal to A_c - A_{light}. The conductivity of illuminated area will increase c-times and there will be a parallel combination of light and dark resistances, R_{photo_light} and R_{photo_dark}, respectively. Total resistance $R_{photo\_tot\_light}$ can be calculated using Equation (3-6). Table 3.1 lists all the assumptions that have been used in the model.

Table 3.1: Listed assumptions in the proposed model.

	Issue	**Idealization**
1	Surrounding air	Perfectly insulating → no droplet oscillating [16]
2	Insulator (including hydrophobic coating)	Homogeneous, electrochemically inert layer does not give rise to spontaneous adsorption of charge [1]
3	Droplet shape	Droplet modelled as a parallel plate capacitor (Figure 3.15d)) → Cylinder with a circular contact area [1; 3; 16]
4	Fringe field (edge effect)	Ignored [1; 16]
5	Electrical properties of each layer	Ideal: constant permittivity and conductivity [16]
6	Capacitance of the droplet	Constant (even during motion) [16], no electric field inside the droplet [100]
7	NaCl	A perfect conductor with used frequencies (~1 kHz) [100]
8	Joule heating (inside the droplet)	Neglected with used frequencies (~1 kHz) [100]
9	Osmotic contributions gravity, inertia and viscous forces electrostatic pressure and electrical double layer	Neglected [1; 16]
	Optoelectrowetting	
A	Profile of light intensity	Uniform
B	Area of each layer	Droplet contact area $A_{liquid} = A_{ins} = A_{photo}$ ($= A_{dark} + A_{light}$)
C	Size and position of light	Light brought on one edge of the droplet → $A_{liquid} = A_{dark} + A_{light} = A_{photo}$

In Table 3.1, the simplified issues and the explanations are presented. In addition, references that explain more why the particular assumption is valid in that particular case are given whenever it is possible. In this thesis, each layer is modelled as a size of the droplet contact area as it has been described earlier and shown in Figure 3.17.

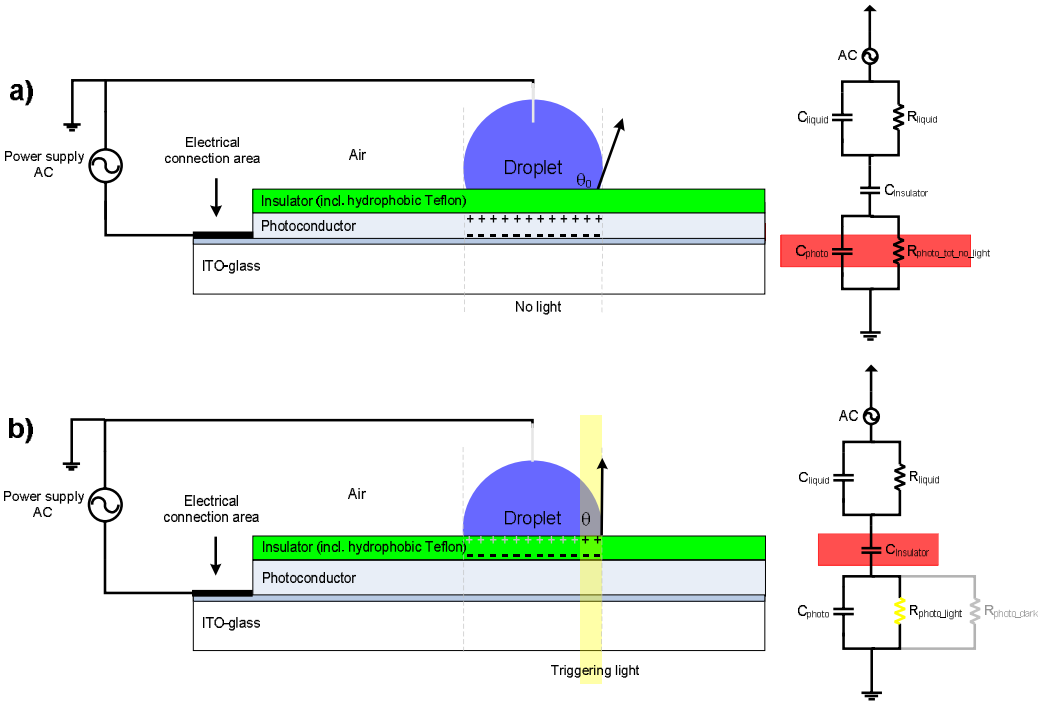

Figure 3.17: A schematic of the used OEW chip and its equivalent circuit, a) without light photoconductor layer is modelled as a size of a droplet, b) when triggering light is applied, there will be a parallel combination of illuminated and dark areas. Red line is marking the major voltage drop.

Based on the proposed model, the absolute impedance values of each layer of the test discussed in Section 3.2.4 are calculated. It is assumed that the 2 µl droplet has a perfect hemisphere shape, resulting that the droplet contact area A_c = ~3 mm^2. Furthermore, the triggering light is assumed to enhance 100x times the conductivity of photoconductor (c = 100) and have an area of A_{light} = 0.1 x A_c. If assuming a circular light spot, this results a light beam with a diameter of slighly over the diameter of the used laser beam (0.6 mm, [99]). The parameters, listed in Table 3.2, that are used for the calculations are from [48-52]. The results for typical DI water and electrically more conductive NaCl droplets with dark and light states are plotted in Figure 3.18. The absolute impedance value of each layer is calculated using Equation (3-3).

For an effective OEW, when light is not applied, the major voltage drop should be over the photoconductor, resulting that the impedance of the photoconductive layer should be larger than any other layer. On the other hand, when light is applied, the insulator layer should have the highest impedance value to enable electrowetting. This would lead that the major voltage drop is shifted from the photoconductive layer to the

insulator layer. As shown in Figure 3.18b), the operation frequency range with NaCl droplet is starting from ~100 Hz when the impedance of the insulator layer equals to the impedance of the photoconductor during the dark state. On the other hand, the upper frequency is around 1100 Hz, which is the frequency when the impedance of the insulator layer equals to the impedance of the photoconductor layer.

Table 3.2: Used parameters to plot Figure 3.18.

Material	**Relative permittivity ε**	**Electrical conductivity σ (mS/cm)**	**Common parameters**
DI water	72	$1*10^{-3}$	ε_0 = 8.854e-12 (F/m) Droplet volume (hemisphere): 2 µl Droplet area: 3.0465 mm^2 Light area: 0.1x $A_{droplet}$ Photoconductivity (a-Si) c: 100
NaCl	72	15	
Teflon®	1.9	-	
Si_3N_4	7	-	
a-Si	11.8	$1.67*10^{-5}$ (dark state) $1.67*10^{-3}$ (light state)	

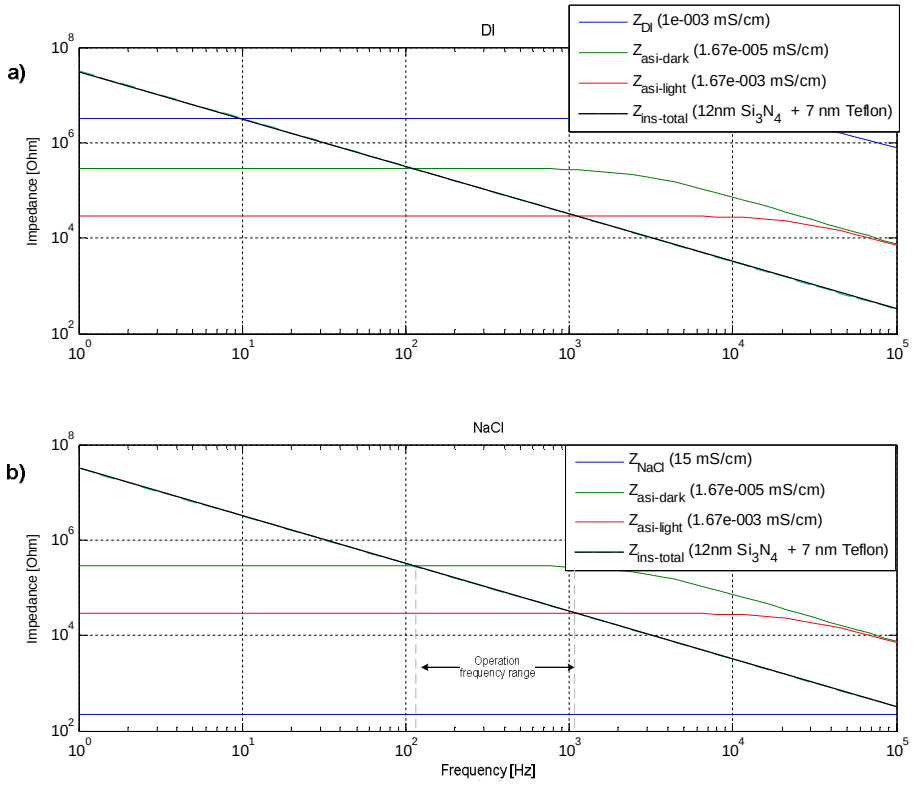

Figure 3.18: Calculated absolute values of impedances of each layer as a function of frequency, when the droplet is a) DI water, b) NaCl.

Based on the results presented in Figure 3.18 , the normalized voltage drops over each layer are calculated and plotted in Figure 3.19. These normalized voltage drops, calculated using Equations (2-19) and (3-3), are showing maximum values, resulting

that these voltage drops are not in same phase and that their sum is larger than one with a certain frequency as shown in Figure 3.19. As it can be seen from the results in Figure 3.19a), with DI water having large impedance, effective optically controlled manipulation is not possible with this system when frequency is above ~10 Hz because then the major voltage drop is over the liquid layer, not over the insulator layer that is required for electrowetting. On the other hand, for the NaCl droplet, the result shows that the voltage drop over the photoconductor layer is controllable by light.

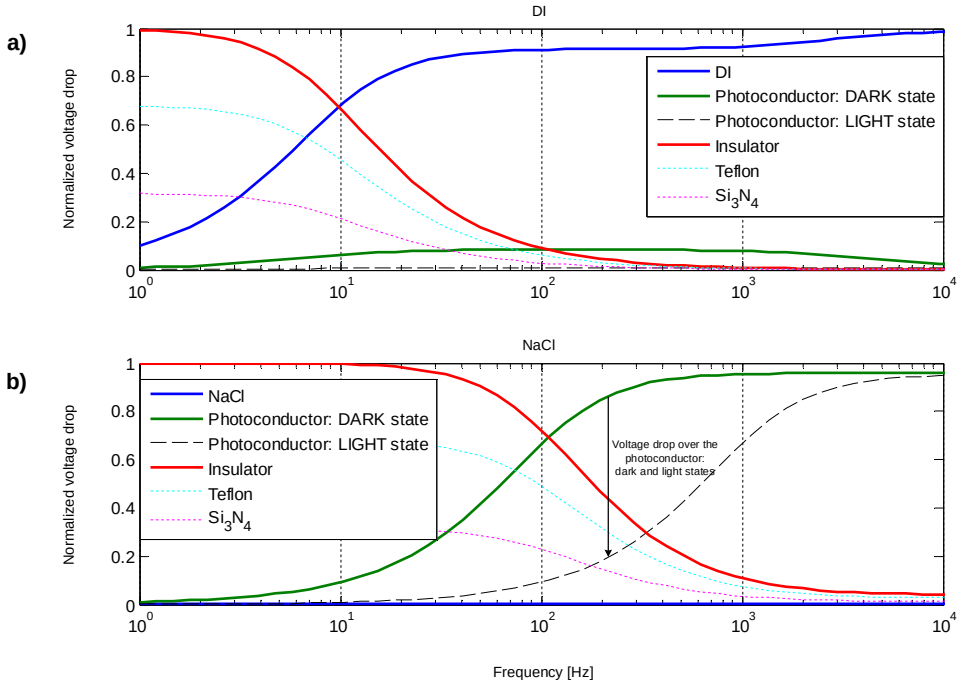

Figure 3.19: Calculated voltage drops over each layer at the dark state, a) with DI water, the major voltage drop is over liquid when frequency is over 10Hz, b) with NaCl, the voltage drop over the photoconductor layer can be controlled by light. In both figures, the voltage drop over the photoconductor layer when light is applied is also plotted to verify the difference between the dark and the illuminated states.

It is essential to optimize the used frequency to be able to operate effectively an OEW device. In this thesis, a MATLAB-based function to provide a visual tool for the designing task is developed. The function plots the normalized voltage drop over each layer at the illuminated state, thus the normalized voltage drop over the insulator layer at the dark state. The purpose of the function is to illustrate the difference between the voltage drops over the insulator layer in both states, as shown in Figure 3.20. It can be noticed in Figure 3.20a) that with DI water, the manipulation is not possible. For NaCl droplet, the result shows that the optimal frequency range for OEW with the used system is between around 300-1100 Hz as shown in Figure 3.20b). At this frequency range, the difference between the illuminated and the dark states, marked as OEW-voltage, is the largest, thus the optoelectrowetting control is the most effective.

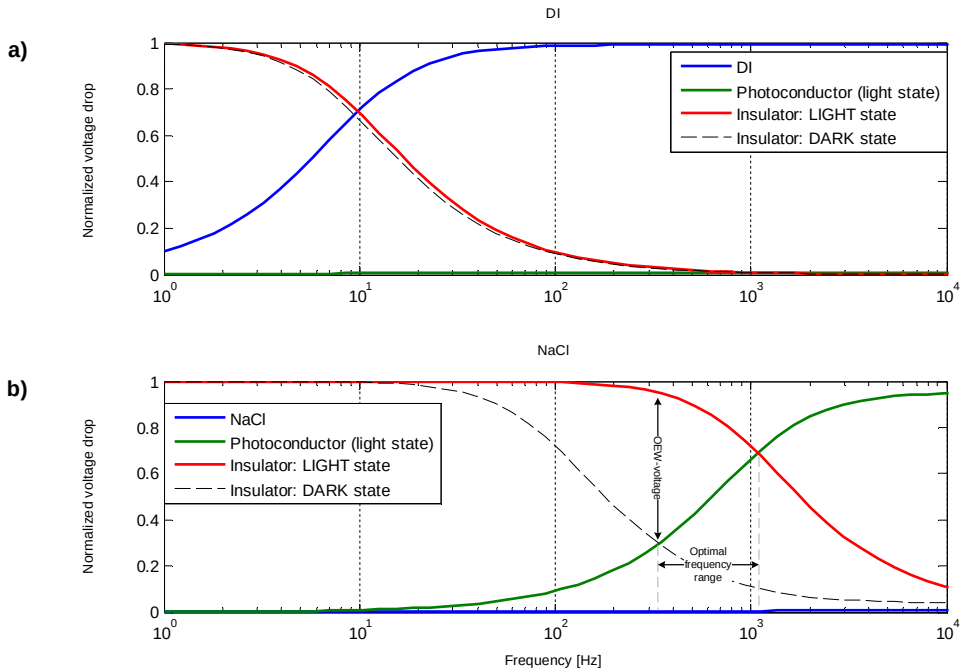

Figure 3.20: Calculated voltage drops over each layer when light is applied, a) with DI water, the major voltage drop is over liquid when frequency is over 10Hz, b) with NaCl, the optimal frequency range for OEW is between ~300 and 1100 Hz. In both figures, the voltage drop over the insulator layer at the dark state is also plotted to verify the difference between the dark and the illuminated states (the difference expressed as OEW-voltage in the lower figure).

It is possible to analyse the OEW tests with the developed tool. As was shown in Figure 3.5 for DI water, the initial contact angle of the droplet on the Teflon® surface used in the experiments that were presented in Section 3.2.4 was remarkably lower than expected. Now, when the contact angle was initially low, and because typically the contact angle will saturate at around 75° [48] or oven at 80° [30], the result might be that no noticeable electrowetting effect is observed. A possible reason for that electrowetting was not detected with NaCl, is related to dielectric breakdown of the Teflon® layer. To obtain a reliable electrowetting behaviour, voltage over each layer has to smaller than DB-voltage. Because in the used set-up, Teflon® layer is relative thin (~7nm), when applying a voltage with a low frequency or DC, the major voltage drop is over Teflon® as presented in Figure 3.19b). It shows that normalized voltage over Teflon® layer is around 0.7 (dotted magenta line in the figure). When the applied voltage is 1V, the maximum voltage drop over the Teflon® layer is 0.7V. On the other hand, using Equation (2-5) and the theoretical dielectric strength of Teflon® (59 MV/m [1]), the dielectric breakdown voltage U_{DB} of the seven-nanometer-thick Teflon® is 0.413V. For this reason, the hypothesis is that the Teflon® layer experienced a

dielectric breakdown (Figure 3.6b) and d)) before observable electrowetting effect was achieved.

3.4.2. Conclusion

In Section 3.4, a new analysis method for optoelectrowetting was developed and presented. In the proposed method, each layer in the OEW device is modelled as an area of the droplet contact area. In the method, the photoconductive layer is modelled as a parallel compination of illuminated and dark areas, therefore also the size of the applied light beam compared to the droplet contact area is significant, thus should be considered when designing an effective OEW device. The reason for developing the new model is that the published models have not been described comprehensively. Using the presented method, the analysis was able to explain the reasons for failures that were encountered during previously performed experiments in the most of the cases. It can be concluded, that the developed model illustrates the reasons for the results in OEW-test with the current set-up. For this reason, based on the model presented here, some modifications for the set-up are proposed in Section 3.5.

3.5. Proposed OEW device based on the developed model

In this section, parameters for the proposed OEW device are considered. A closed OEW set-up including bottom and top electrodes is used. Firstly, the requirements of an OEW device working effectively are discussed before presenting the proposed model. Using the listed assumptions, the normalized voltage drops over each layer in the proposed system are analyzed.

For effective OEW manipulation, it is essential to choose device parameters carefully. The voltage drop over the insulator layer in the dark state can be minimized by choosing remarkably thicker photoconductive layer than the insulator layer [50]. Secondly, each layer should be thick enough to prevent dielectric breakdown occurring before voltage required for effective electrowetting. For effective optical control, laser will be used as a light source. Lastly, the top layer should be transparent for visual inspection, so it is desirable to use on top a transparent electrode coated with thin hydrophobic layer.

Based on the listed requirements, a proposed two-plate device is following: a photoconductive amorphous silicon layer, deposited on top of ITO-glass used as a bottom electrode, is 5 micrometers thick. It is covered with a 300-nm-thick silicon nitride layer. The bottom electrode is finally coated with a 20 nm Teflon® layer to achieve a higher initial contact angle and lower the contact angle hysteresis, thus enhancing the electrowetting effect. For this reason, also the top electrode, transparent ITO-glass, is covered with a Teflon® layer. A thinner (7nm) layer is used to improve the electrowetting effect on the bottom of the droplet. The gap between bottom and top electrode is chosen to be 0.5 mm. With the considered droplet volume of two

microliters, and assuming the shape of the droplet to be a perfect cylinder as it was explained previously, the droplet contact area is A_c = *Volume/gap* = 4 mm^2. If assuming A_{light} = 0.1 x A_c, the diameter of the circular laser beam is required to be ~0.7 mm. A schematic of the proposed set-up is shown in Figure 3.21.

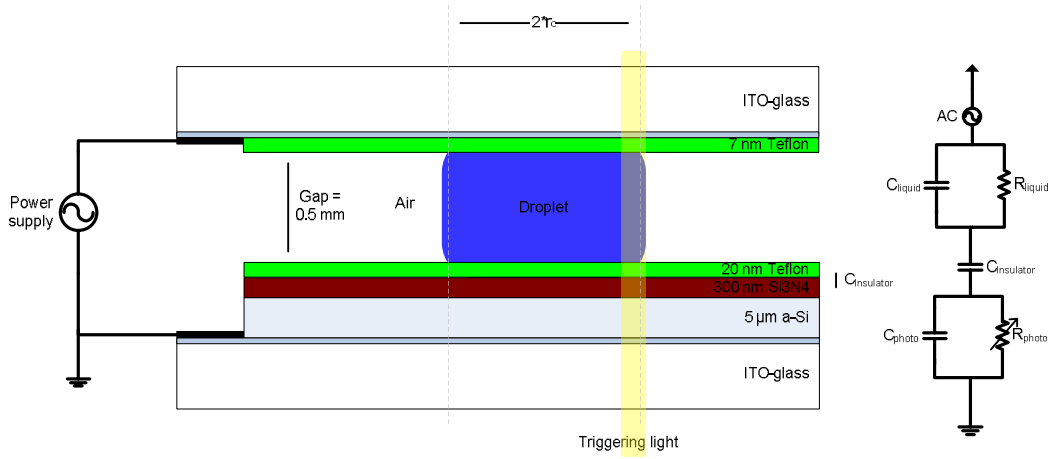

Figure 3.21: A schematic of proposed device without spacer between bottom and top plates (not in scale) and its equivalent circuit. A thin (7nm) Teflon® coating on top electrode is neglected from the equivalent circuit.

Several assumptions, that were listed in Table 3.1, have been made in the proposed set-up. Based on the assumptions, the impedance of each layer is calculated for 2 µl droplet. Used parameters are same than in Table 3.2 except the cylinder droplet shape with the height of 0.5 mm (gap) and the contact area of 4 mm^2. The calculated impedances for DI water and NaCl droplet are shown in Figure 3.22. It can be noticed, that the photoconductor layer in the dark state has larger impedance than the insulator layer when frequency is higher than ~300Hz. On the other hand, in the light state, impedances of insulator and photoconductor layers are equal when frequency is ~4 kHz. The effective frequency range for the set-up is between these two limits.

To discover the optimal frequency range of this device, the normalized voltage drop over each layer as a function of frequency is calculated using Equation (3-4) divided by *U* as was used in Section 3.3. The results with DI water and NaCl, shown in Figure 3.23, are presenting the voltage drops over each layer when light is applied. Furthermore, normalized voltage drop over the insulator layer without light is drawn with dashed black line to illustrate the difference between the dark and light states. This normalized voltage drop difference between these two states, marked as OEW-voltage in Figure 3.23b), enables optically controlled electrowetting. When working with DI water, the liquid layer will have high impedance. Therefore, no significant optically controlled electrowetting is achieved. With more conductive NaCl, the optimal working frequency range can be estimated to be between 900 Hz and 2300 Hz.

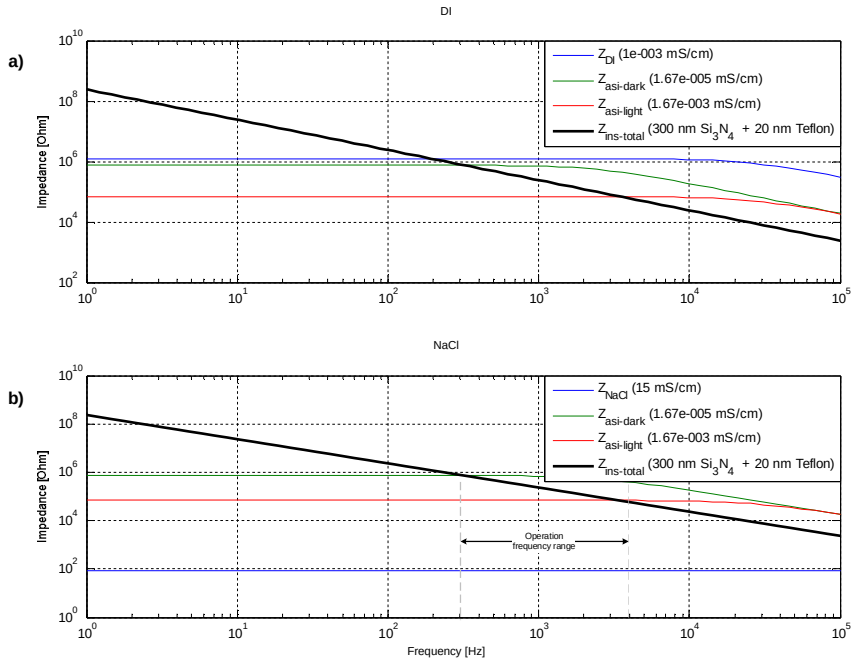

Figure 3.22: Calculated absolute values of impedances of each layer as a function of frequency for the proposed set-up when the droplet (volume: 2 µl) is a) DI water, b) NaCl.

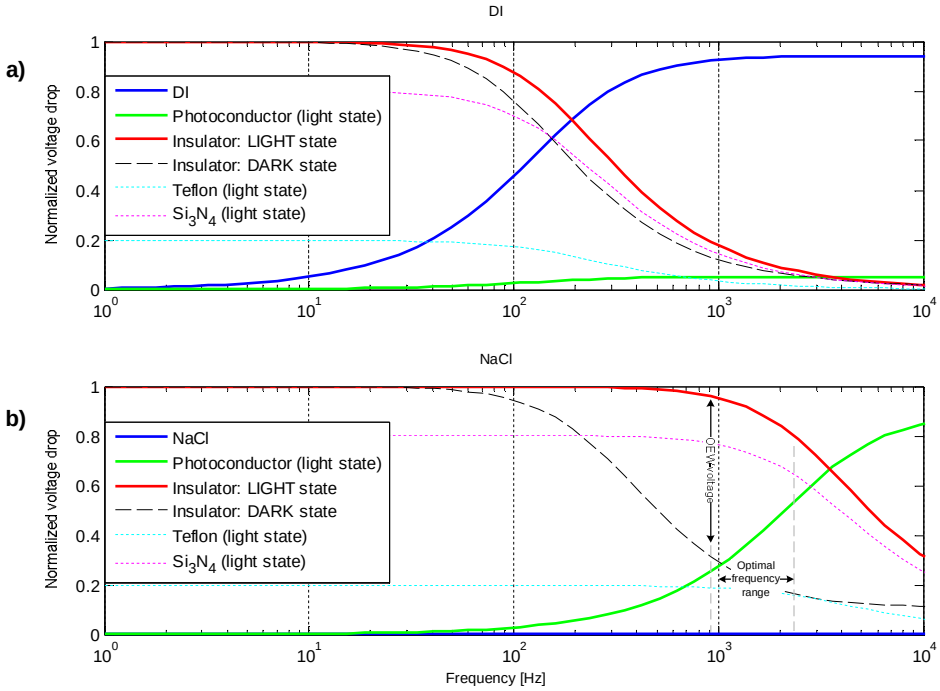

Figure 3.23: Calculated voltage drops over each layer at light state for the proposed set-up: a) with DI water, major voltage drop is over liquid when frequency is over ~200Hz, b) with NaCl, optimal frequency range for OEW is between ~900 to 2300 Hz.

It should be noticed, that even though 20nm Teflon®-coating is only around three times thicker than previously used 7nm, the electric field over Teflon® layer is remarkably lower in this case because of thicker silicon nitride layer is included in the system. This can be validated by comparing the normalized voltage drops over the Teflon® layer with NaCl droplet in both cases with used frequency range (1kHz). This value is reduced from ~0.7 in previous set-ups to ~0.2 in the proposed model as plotted with dashed cyan line in Figure 3.23b). The result is that the maximum voltage that can be applied to the system is remarkably larger than previously as reported in Section 3.4.1. Using Equation (2-5) together with the calculated normalized voltage drop (0.2), and knowing the theoretical dielectric strength of Teflon® (59 MV/m [1]), the maximum theoretical voltage that can be applied to the system without breaking the Teflon® layer is 5.9V. This is more than ten times larger voltage than in the previous set-up presented in Section 3.4.1. The hypothesis is that with the proposed system, observable electrowetting effect can be achieved without breaking the Teflon® layer.

It has been also shown that when working with the proposed frequency range, NaCl can be assumed as a perfect conductor, resulting a zero voltage drop over liquid layer. For this reason, Joule heating inside the liquid can be neglected from the analysis [100]. If the purpose is to manipulate also DI water, it is required to decrease the impedance of the liquid layer. This can be obtained by using a smaller electrode gap, thus enabling effective DI water droplet manipulation.

3.6. Conclusion

At the begin of Chapter 3, the fabrication procedure and the first experiments and their results with the used OEW chips were presented. The study of the published OEW set-ups were reported in Section 3.3. In the next section, the proposed model was presented and used when analyzing the results from the first experiments. With the model, the possible reasons for the results were discovered. Based on the model that was developed in Section 3.4, the proposed platform was described in Section 3.5. The system performance was analyzed with the developed model. The simulated results showed that the proposed set-up could be used as a platform for effective optoelectrowetting manipulation.

The main point of this chapter was to develop a model to describe the optoelectrowetting phenomenon. Inspection of the published simulation showed that there is no unambiguous model to describe optoelectrowetting. For this reason, a new model was proposed. In the model, each layer is presented as a size of the droplet contact area. Furthermore, a function to help the designing process of the OEW device was developed. The developed model together with the presented designing function provides a tool that can be used when developing the effective OEW platform.

4. SUPPORTING TESTS FOR THE PROPOSED MODEL

The purpose of this chapter is to report tests that were performed to validate the proposed model presented in Section 3.5. The first part of this section describes the impedance measurements of a sessile droplet. The objective is to verify the model used for the droplet and the measurement results. In the second section, simple electrowetting tests with DC-voltage using the third batch of OEW chips are described.

4.1. Measuring impedance of a sessile droplet

The impedance of the droplet was measured to verify the model of liquid that was used in Chapter 3. At the begin of this section, a short overview of the theory of impedance measurement of liquid using a 2-terminal technique is summarized before presenting the impedance measurement set-up and the results.

4.1.1. Theory of impedance measurement of liquid

The impedance of the material can be obtained by applying the AC voltage to the material, and defining the ratio of the measured voltage to the measured current. In a 2-terminal measurement configuration, only two cables are used to connect the material to the impedance measurement device. When the measured material is liquid, the interface of electrode-electrolyte (droplet) affects the measurement results. The reason for this is that the electrons are the carriers of current in electrodes, whereas through the liquid current is carried by ions of the electrolyte. For this reason, a transfer mechanism to enable current flux is needed. The transfer mechanism can be modelled as a resistor R_b in series with a parallel combination of resistor R_d and capacitor C_d, as presented in Figure 4.1a). R_b can be understood as a bulk resistance associated with the resistance of the electrode material itself and interfacial effects, whereas R_d and C_d represent the impedance of electrode-electrolyte interface and its polarization. As shown in Figure 4.1a), together these three components are expressed as $Z_{interface}$. [101]

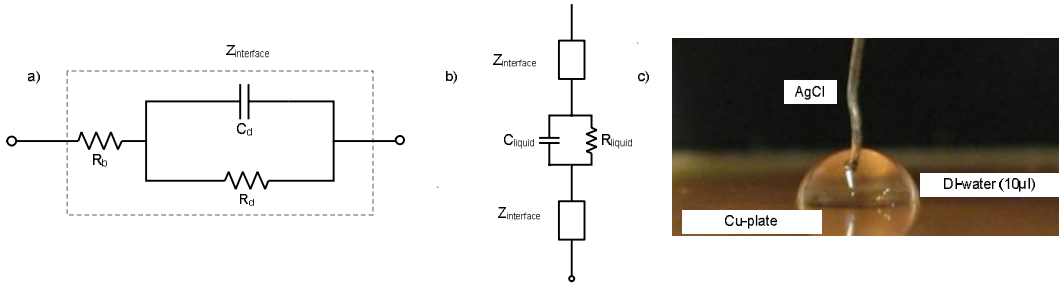

Figure 4.1: Impedance measurement: a) an equivalent circuit of the interface of electrode-electrolyte [redrawn from 101], b) an equivalent circuit of the impedance of the droplet with two interfaces, c) a photo of measuring the impedance of de-ionized (DI) water (volume: 10 µl) using a top (silver-chloride, AgCl) tip electrode and a bottom copper (Cu) plate electrode plate.

At low frequencies, where the impedance is dominated by the serie combination of R_b and R_d, these two interfaces (droplet contacts with both upper and lower electrodes) are remarkable, and should be taken into account when verifying the model. At high frequencies, the impedance is closely to R_b. Figure 4.1b) represent the equivalent model when measuring the impedance of the liquid droplet. [101] In this thesis, the droplet is modelled as a parallel combination of a resistor (R_{liquid}) and a parallel capacitor (C_{liquid}.).

4.1.2. Measuring impedance of a droplet

Impedance measurements presented here were performed in facilities provided by Department of Biomedical Engineering, Tampere University of Technology [102] using Impedance/Gain-phase Analyzer (1260A from Solartron Analytical [103]). A house-made set-up, shown in Figure 4.2, where a tip electrode of silver chloride (AgCl) was attached to a translation stage from Standa [104], enables precisely adjustment of the height of tip. A large copper (Cu) plate was used as a bottom electrode.

The used 2-terminal measurement configuration is the simplest method of connecting the inspected material, thus contains many possible error sources. Furthermore, a relative simple house-made set-up using a copper plate was used in the measurements. For this reason, it was crucial to analyze first the impedance of the measurement system itself without a droplet. This was performed by bringing a tip electrode to contact with the bottom plate electrode.

Figure 4.3 illustrates, that no significant noise was observed. It can be noticed that impedance of the measurement set-up itself is negligible (~1-5 Ω) and can be neglected in the droplet impedance analysis. It can be concluded that workability of this set-up is good enough because the typical impedance of a DI water droplet is several hundreds of kilo-ohms.

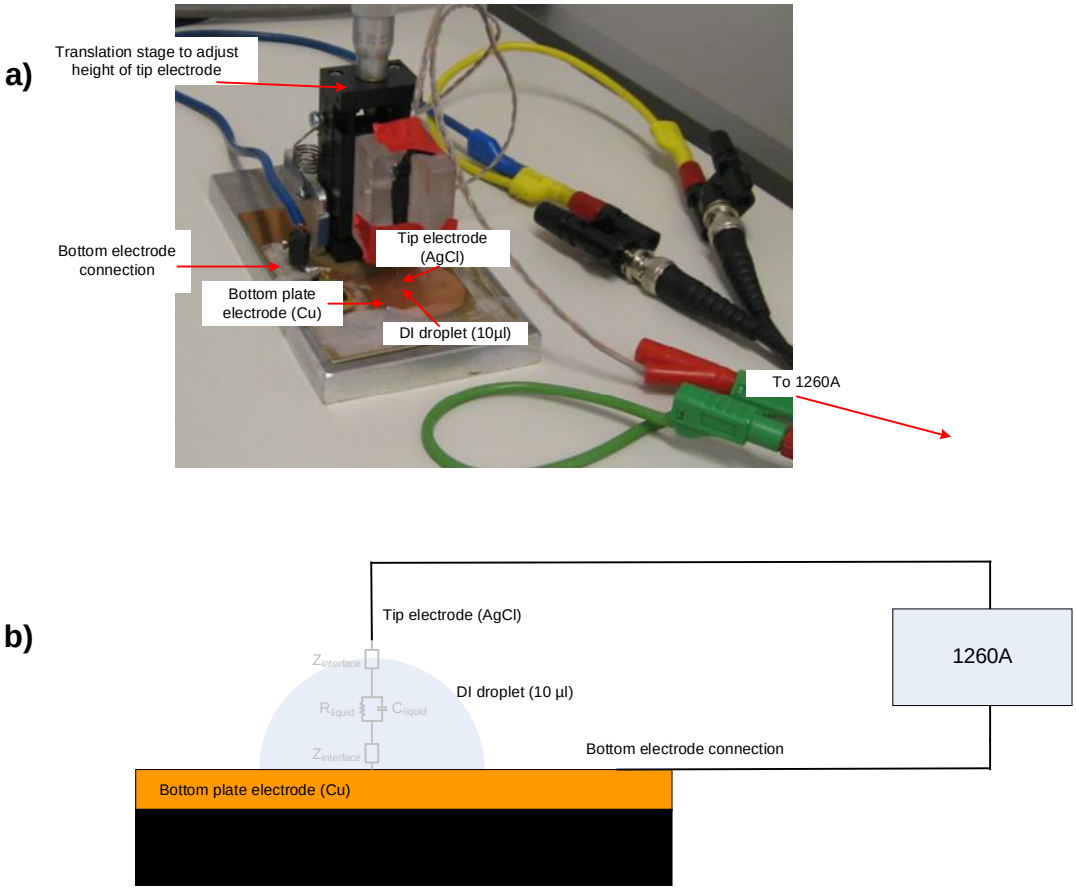

Figure 4.2: Impedance measurement, a) set-up used for impedance measurement, b) a schematic of the set-up including the equivalent circuit of impedance measurement (not in scale).

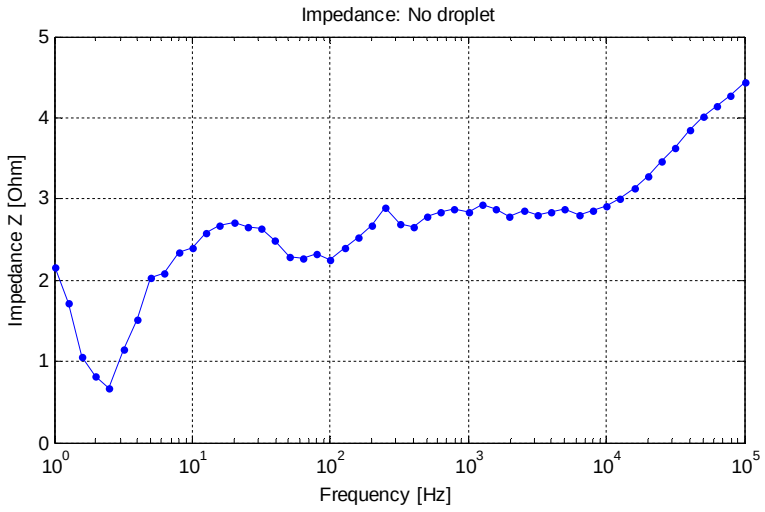

Figure 4.3: Impedance measurement without a droplet.

The original plan was to use 2 µl droplets in the experiments. However, it was noticed immediately that these droplets evaporated too fast with the set-up and normal room temperature conditions. For this reason, 10 µl DI water was used as shown in Figure 4.2. Three measurements and their mean value are plotted together with model using hemisphere assumption (contact angle is 90°) and with previously given values (Table 3.2) in Figure 4.4a). As it was discussed in the previous section, two interfaces between electrode and electrolyte include addition impedances to the system that are not included in the model of the droplet. With low frequencies, because of parallel combination of R_d and C_d, as is presented in Figure 4.1a), $Z_{interface}$ is larger and thus measurement set-up impedances are notably affecting the results. [101] For this reason, it is more reliable to compare the responses of modelled and measured with higher frequencies (from 1kHz to 100 kHz). As it can be seen, the model describes the measured behaviour well having approximately same cut-off frequency f_c.

Even though the behaviour of impedance is similar between modelled and measured ones in the frequency range of 1kHz to 100 kHz, the model shows higher impedance. In the model, it was assumed that the droplet is a perfect hemisphere. However, as it could be seen in Figure 4.1c), the estimated contact angle is closer to 80°, not 90° as it was assumed. Assuming a spherical droplet with the known volume and the contact angle θ, the contact radius r_c and the droplet area A_c, the droplet height h can be calculated by [16]:

$$\begin{aligned} r_c &= \sqrt[3]{\frac{3*Volume}{\pi\left(\cos^3\theta - 3*\cos\theta + 2\right)}} \\ A_c &= \pi * r_c^{\,2} \\ h &= \frac{r_c}{\sin\theta} * (1-\cos\theta) \end{aligned} \tag{4-1}$$

The impedance of the droplet with a contact angle of 80° is calculated and plotted in Figure 4.4b). As it can be seen, the modelled and measured impedances have similar values except at low frequencies. This is mainly because of the impedance of the electrode-electrolyte interface $Z_{interface}$ as it was discussed in Section 4.1.1.

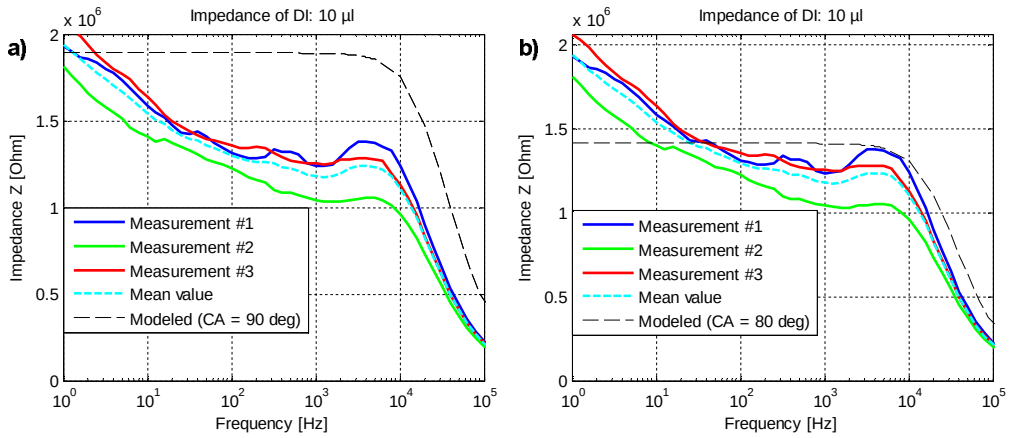

Figure 4.4: Impedance measurement with 10 µl DI water droplet together with a: a) model based on hemisphere assumption, b) model where the droplet contact area and the height of the droplet are calculated using Equation 4.1 and assuming that the contact angle is 80°.

In this section, the measured droplet impedances were compared to the calculated values using a simple model. In the model, the droplet is assumed as a cylinder shape with the bottom area being equal to the droplet contact area and the height being the height of droplet with the assumed contact angle. The measurement results showed that the impedance of a sessile droplet on a smooth surface could be estimated by using the proposed droplet model.

4.2. Electrowetting experiments with the third OEW chip using DC-voltage

Tests that were performed using OEW chips from the third batch are reported in this section. The goal was to identify, is it possible to observe any change in the contact angle of the droplet thus introducing electrowetting effect by using DC-voltage. Before presenting the results, the structure of the used OEW chip and the used set-up in these test together with the developed algorithm and and an initial evaporation test are briefly summarized.

4.2.1. Structure of the used OEW chip and the system set-up

The fabrication process was similar than was reported in Section 3.1. Photoconductive a-Si layer (1.5µm) was deposited on ITO-glass. It was then coated with 10 nm Teflon®. The structure of third batch is similar than smooth Teflon® side in Figure 3.1 a) except now coating is slightly thicker. Modelled impedances and voltage drops over each layer are similar than was plotted previously in Figure 3.18 and Figure 3.20, respectively. Based on the model, when using DC-voltage, the major voltage drop should be over the insulator, thus leading to electrowetting even without using any triggering light.

For the contact angle measurement, a new set-up show in Figure 4.5 is used. It consists of a manually controlled precision DC-power source Switchbox 6303DS [105], a motorized zoom microscope [94] and a house-made stage for the OEW chip. Video is taken using XCD-X710 camera from Sony [95]. In addition, the used tip electrode (AgCl) is attached to the translation table from Standa [104] to enable precise positioning.

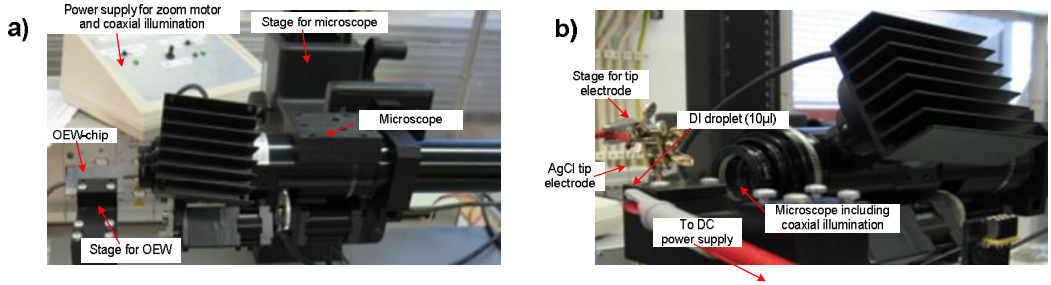

Figure 4.5: Set-up for DC-electrowetting test, a) top-view, b) side view.

During the measurements, coaxial illumination that is integrated in the microscope is used. For side-view inspection during the experiments, microscope is turned horizontally and aligned precisely using an electrical angle measurement device.

4.2.2. Developed algorithm for contact angle calculation and an evaporation test

To analyze experimental results, a MATLAB-based algorithm was developed at the research group. A screenshot of the user-interface for contact angle analysis of a sessile droplet during electrowetting test is shown in Figure 4.6. The contact angle calculation includes the following steps: firstly, circles on the droplet and its shadow are fitted (red and blue lines, only one pair shown in Figure 4.6). The surface is determined by drawing a line between found contact points at intersections of fitted circles (green line). On both sides of the droplet, a tangent to the circle is drawn from intersection (purple lines). Lastly, the contact angle is determined by calculating an angle between the surface line and tangent from the intersection on both sides of the droplet as shown in Figure 4.6.

During the EWOD-tests, a 2 µl droplet is used. For this reason, the evaporation rate of a sessile droplet on test environment (temperature 22° Celsius, humidity 88%) was first tested to be sure that droplet evaporation does not need to be considered during the electrowetting tests reported in the next section. Evaporation of a 2 µl size droplet that is not experiencing electrical actuation is mainly because of a so-called Marangoni flow, which describes a random motion inside the droplet [1].

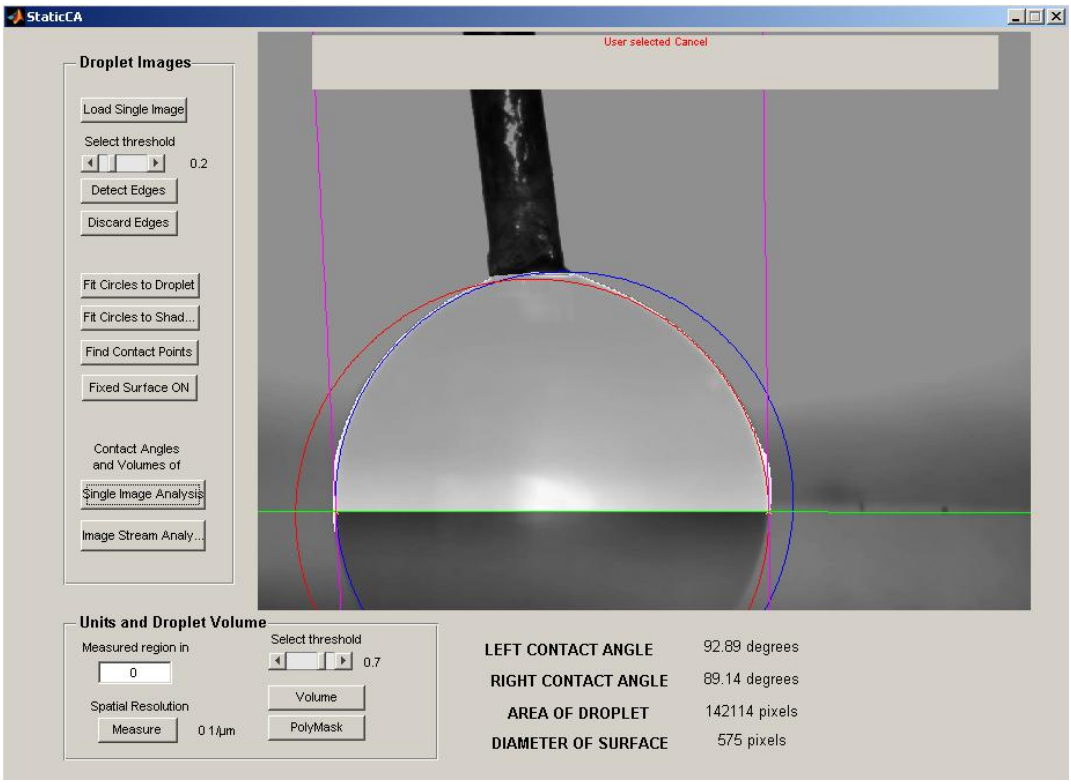

Figure 4.6: A screenshot of a developed user-interface for contact angle calculation.

In the evaporation experiment, a droplet is pipetted on the surface of the used OEW chip. Compared to Figure 4.6, there is no tip electrode to be contact with the droplet. After the experiment, photos are analyzed with the presented algorithm. Based on the analysis together with Equation (4-1), the calculated droplet volume and the left contact angle (CA) for DI water are plotted in Figure 4.7.

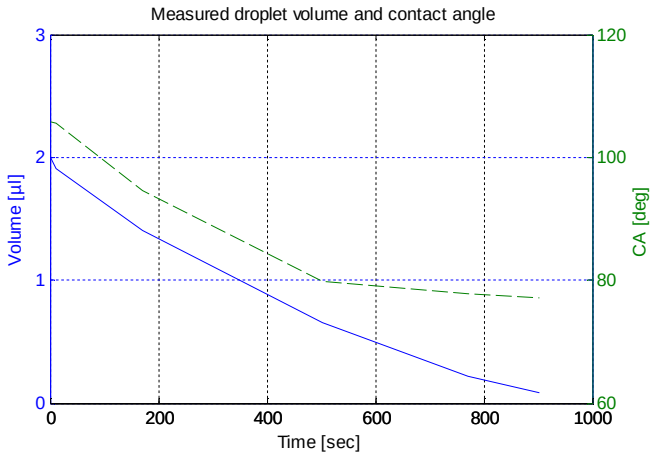

Figure 4.7: The analyzed DI water droplet volume (blue line) and the left contact angle (dashed green line) as a function of time.

Evaporation test shows, how the contact angle change at each evaporation stage. The contact angle changes approximately ten degrees at first 170 seconds. The conclusion is that in our electrowetting tests to be presented in Section 4.2.3, where the phenomena to be observed should happen in a scale of less than a second, evaporation is negligible. During the evaporation test, it was also observed that in the third batch of OEW chips, the initial contact angle of the droplet is up to around 105°.

4.2.3. DC-electrowetting proof-of-concept test with a sessile droplet

In this section, experiments with DC-voltage together with DI water and NaCl droplets are reported. The goal was to observe electrowetting effect that should happen even without applying light when using DC-voltage as it was simulated in Figure 3.20. The used set-up was described in Section 4.2.1. Tests were performed in the same environment conditions that was previously reported during the evaporation test. First, a 2 µl droplet was pipetted on the OEW-surface that was connected to power source and was electrically grounded. To close the electrical circuit, the bottom tip electrode that is also connected to power source was brought inside the droplet using the translation stage. DC-voltages between zero to 32.1 V were applied to the droplet. A left and right contact angles, a diameter and and area of the droplet were analyzed from taken images using developed MATLAB-based algorithm as was explained in Section 4.2.2.

Altogether three EWOD-tests with DI water and five tests with NaCl were performed. At the begin, zero voltage was applied to the droplet before increasing DC-voltage manually. The goal was to study also a reversible EWOD-effect by returning the voltage back to zero and grounding the bottom electrode. During the first unsuccessful test (not included in the analysis), grounding was noticed to be essential. It was observed that to minimize undesirable electrostatic energy that could affect the initial contact angle of the droplet, the bottom OEW chip and supporting parts, such as stages for the tip electrode and the OEW chip, have to be grounded before pipetting a droplet on the surface.

Tables providing information about each test are given in Appendix. Measured values are mean values of two separate analyses that have been done for each test. In these tables, an applied voltage U, left and right contact angles (θ), an area of the droplet, a contact diameter ($2*r_c$), a video frame rate, a reference image (point when a measurement time is chosen to be zero) and a measurement time are given together with their standard deviations. Procedure of a single image analysis was explained in Section 4.2.2. The volume of the tip electrode inside the droplet was neglected from the analysis. This simplification was done, because the volume of the used tip electrode with a diameter of 300 µm and assuming that it is at the maximum 500 µm deep inside the droplet is around 0.035 µl, which is only a fraction of the total droplet volume (initially 2 µl). Based on the analysis, no reversible electrowetting was observed. It was not noticed that the contact angle returned (or increased) to the original state when the voltage was decreased to zero. For this reason, the summary of performed tests provided in Table 4.1 presents only the initial contact angle of before the voltage was

increased and the contact angle change after the voltage, excluding steps when the voltage was decreased.

Table 4.1: Summary of EWOD tests presenting approximated values of initial contact angle (θ_{0_d}) and its change $\Delta\theta$ straight after voltage is applied.

DI water		**θ_{0_d} [°]**		**$\Delta\theta$ [°]**	
Test #	**Voltage**	**Left**	**Right**	**Left**	**Right**
1	0.0 → 9.6	85	82	-	-
1	9.6 → 27.2	83	80	-	-
2	27.2 → 32.1	80	78	-	-
2	0.0 → 6.3	88	91	-	-
2	6.3 → 21.1	88	88	2	-
2	21.1 → 32.1	85	87	-	-
3	0.0 → 31.2	98	94	6	7
NaCl					
Test #	**Voltage**	**Left**	**Right**	**Left**	**Right**
1	0.0 → 7.7	87	87	22	20
1	0.0 → 32.1	60	60	-	-
2	0.0 → 8	90	88	-	-
2	8 → 17.4	87	84	-	-
2	17.4 → 32.1	86	81	1	-
3	0.0 → 2.3	77	90	1	3
3	2.3 → 5.6	76	93	-	-
3	0.0 → 6.0	77	92	2	-
3	0.0 → 32.1	84	84	-	2
4	0.0 → 12.6	82	78	3	3
4	0.0 → 20.1	< 70	< 70	4.5	2
4	0.0 → 32.1	< 60	< 60	-	-
5	0.0 → 15.1	88	88	6	7

It can noticed from the results presented in Table 4.1 that with the new batch of OEW, some electrowetting effect was observed. However, tests were not repeatable, for example with NaCl droplets, there was a large variation in contact angle change when voltage was applied even the initial shape of the droplet would have been similar (for instance the first and the fifth NaCl tests). Furthermore, significantly higher electrowetting effects with smaller applied voltages were noticed with electrically more conductive NaCl droplet than DI water. Based on the analyses in Chapter 3, this was excepted observation. The largest contact angle changes were observed from the third and the first measurement of DI water and NaCl, respectively. Images before and after voltage is applied in these tests are shown in Figure 4.8, showing the maximum detected contact angle change with both liquids. It is easy to notice that with NaCl remarkably larger changes were observed with smaller applied voltages.

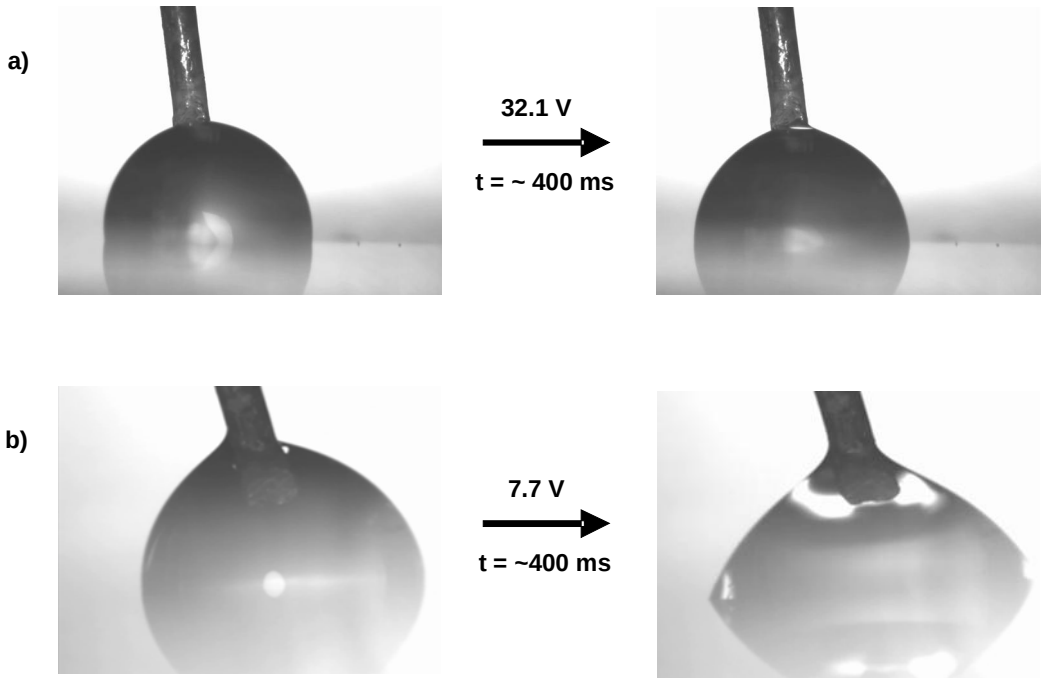

Figure 4.8: Images from DC-electrowetting test showing change in the droplet contact angle before (left figure) and after (right figure) voltage is applied: a) the third DI water test, b) the first NaCl test. See text for the details.

As mentioned, a reversible electrowetting effect was not detected during any experiment. Even in the first NaCl-test, where the contact angle reduction of over 20° as shown in Figure 4.8 b) was observed, the contact angle did not experiment any increment when voltage was returned to zero and the bottom electrode was grounded. The following hypotheses were concerned: the creation of capillary forces, the contact angle hysteresis and the surface contamination. These are shortly discussed next.

The first hypothesis is that the generated capillary forces between the droplet and the tip electrode are restraining the droplet so that it cannot return to original shape. However, it does not seem to be probable reason because no publication, to the best knowledge of the author, has reported this phenomenon. A more plausible reason is that reversible electrowetting effect was not noticed because of the contact angle hysteresis. As it was discussed in Section 2.2.6, a typical hysteresis value of a DI water droplet in an air environment is 7-9° [1]. The maximum observed electrowetting effect with DI water was less than this, so return of the contact angle might be prevented by the contact angle hysteresis. However, over 20° change in the contact angle was detected with NaCl droplets. Therefore, the contact angle hysteresis can not explain why the contact angle did not return at all when zero voltage was applied. In the NaCl droplet case, one possible reason is that the surface was contaminated during the experiment, thus preventing the control of the contact angle with the applied voltage. To confirm that this effect would be the correct reason for the observed behaviour of the droplets, more study about the properties of the surface that was used in the experiments is required.

4.3. Conclusion

Tests supporting the previously proposed model were presented in this chapter. Impedance measurement showed that modelling a droplet as a combination of a resistor and a parallel plate capacitance with a thickness equal to the height of the droplet gives reasonable values. Therefore, the model can be used for designing an OEW-device. With the third batch of OEW device, some electrowetting effects on sessile droplets were observed. The results showed that the electrowetting effect was enhanced when replacing a DI water droplet with an electrically more conductive NaCl solution. This was expected results from the modelling process and further emphasize that the model, even including several assumptions and simplifications, is valid. However, the developed model is not able to explain, why the reversible electrowetting effect was not observed during the experiments. Some hypothesis for this behaviour were proposed, but the real reason for it remains still unclear and would require further inspection.

5. CONCLUSION AND FUTURE DEVELOPMENT

The aim of this thesis work was to present a dynamic and reconfigurable device capable of microliter droplet manipulation operations using optically induced electrowetting. The first task was to identify and understand the studied phenomenon. Based on the study, the goal was to develop a relative simple but still sufficiently precise model describing the optoelectrowetting phenomenon. The purpose of the presented model was to propose a design tool that could be effectively used when developing a platform for parallel multiple droplets manipulation. The integration of multiple operations in the same optically controlled platform would enable remarkably higher flexibility and automation level of the system when compared to conventional microfluidic microsystems. While the need of miniaturized fluidic components such as pumps, mixers and valves could be minimized, the system using optoelectrowetting principle could revolutionize for instance biological and medical research.

Firstly, a shortly summary of each chapter and a brief conclusion of the work is presented Section 5.1. The latter part of this chapter introduces the possible future development. This part outlines steps that should be performed for further developing the concept of optoelectrowetting platform.

5.1. Conclusion

This thesis is summarized in this section. The outline of each chapter is given and the most important issues are reported.

In Chapter 2, the theoretical background of optoelectrowetting-based droplet manipulation was considered. The requirements for the effective droplet manipulation using electrical fields were discussed. While the focus was on electrowetting-related operations, also other implementations where photoconductive surface could be used were briefly presented. To emphasize and illustrate the benefits of the concept, also some applications where the light-triggered virtual electrodes could be used were presented in this chapter.

The main goal of this work, the optoelectrowetting modelling process, was presented in Chapter 3. In the first part of the chapter, fabrication procedure of the platform was described. This part reported also the initial tests that were performed using the devices provided by the project. It was observed, that desirable optoelectrowetting effect was not achieved with the used set-up. The latter part of the chapter focused on the modelling process. Firstly, the published studies were closely

inspected to achieve a better knowledge of the optoelectrowetting phenomenon. It was discovered, that the comprehensive and unambiguous model to present optoelectrowetting mechanism is missing. For this reason, a new model describing the optoelectrowetting phenomenon was developed based on the own studies. The model included certain simplifications that were listed and considered in the optoelectrowetting point-of-view. In the presented model, each layer is modelled as a size of the droplet. Thefore, in this new method, the photoconductive layer has to be modelled as a parallel combination of the dark and the illuminated areas. Furthermore, using the presented model, a design tool for developing an efficient droplet manipulation platform was provided. In addition, the required design rules for the effective optoelectrowetting-based droplet manipulation were discussed. These includes the consideration of the size of the light spot and the used droplet, thus that how the impedances of each layer are affecting to the manipulation efficiency. Based on the simplified model, a designed platform was suggested in the last part of Chapter 3. In the proposed platform, thicker insulator layer is used to prevent the observed dielectric breakdown of the tested chips. Based on the results achieved from the modelling, this platform could be used for effective droplet manipulation.

Tests that support the developed model were reported in Chapter 4. Droplet impedance measurements verified that the proposed simplified model to present a droplet is valid. Therefore, it can be used when calculating the impedance of the liquid layer. This chapter reported also the electrowetting experiments that were performed on sessile droplets using DC-voltage. It was observed, that the repeatability of the system to induce electrowetting effect was very low. The reasons for the behaviour were analyzed. It was concluded that the most probable reason for the noticed behaviour is related to the surface properties, which were observed to provide insufficient droplet behaviour. The further investigation of the fabrication process is required to obtain the demands that are essential for optoelectrowetting-based droplet manipulation.

Based on the work presented here, some important issues were observed to be very crucial to perform successful droplet manipulation operations. Especially the surface properties and the used optical triggering light are essential to provide powerful droplet manipulation. The first issue is related to the initial contact angle of the droplet and is crucial to obtain an effective optoelectrowetting-based droplet manipulation system. The fabrication process should be optimized to provide a large contact angle, thus enabling powerful control of microliter droplets. Even though several challenges were encountered during this work, it can be concluded that compared to conventional microfluidics, droplet-based microfluidics provides great opportunities and benefits in various research areas. However, a careful choice of the set-up parameters and fabrication methods is essential to provide an effective parallel multiple droplets manipulation platform. If the platform is designed properly, it can perform multiple operations that are required in various applications in the field of biological and biomedical diagnostic, to just highlight a few possible examples.

5.2. Future development

In this thesis, a model presenting an optoelectrowetting phenomenon was developed. Based on the presented model, a structure of new optoelectrowetting device that could be manufactured was outlined. The first task for the future work would be to verify the proposed model by building the platform and test it experimentally. For the proposed concept in this thesis, the initial test could be performed using a 4-5 milliwatt laser as a triggering light. Using a laser with higher power is more desirable because the focusing objective for the laser beam is not necessary required, thus reducing the complexity of the system set-up.

The first required experiment that should be performed with the developed device is the initial contact angle test with a sessile droplet. The test that was explained already in Chapter 3 provides an easy and fast verification to check that do the used light source, the developed surface and the applied voltage together satisfy the requirements for a significant light triggered contact angle reduction, that is required for effective droplet manipulation. If this test is successful, fundamental droplet operations, such as moving, cutting and merging droplets, can be demonstrated. The next step could be to verify the considered reconfigurable valve concept, where the size of the liquid could be controlled optically.

For the further development of the platform to enable even better droplet manipulation control, the optical power requirements of the photoconductor layer has to be considered. Various set-ups using different light sources have been reported. Typically, 1-5 milliwatt lasers have been used in the experiments. [48-52]. Integrating a laser with a scanning mirror, a precise control of a droplet has been provided [49; 50]. For a parallel multiple droplets manipulation, more laser beams are required. Manipulating four droplets in parallel using two lasers has been demonstrated by implementing the lasers with two galvanometer scanning mirrors [50].

Even though it has been demonstrated that it is possible to create four effective laser beams using only two lasers by time-division scanning [50], this approach would not be desirable for droplet manipulation when the goal is to provide a platform for controlling more than a few droplets in parallel. For this reason, recently it has been demonstrated a concept, where the requirements for the optical power and the required voltage are significantly reduced by using a thin aluminum oxide layer as an insulator layer [106]. Because the higher dielectric constant and easier deposition of the insulator layer, thinner layers were possible to use, reducing the optical power demands of the system on the level that a simple commercial DLP-projector could be used to create and pattern the virtual electrodes. This opens new opportunities of the control systems that would be especially suitable for mobile platform. Without the need of optical alignments using optical components such as lens, objectives and mirrors that are required to direct the patterned light on the optoelectrowetting surface, a more compact device can be implemented. The hypothesis presented here is that the DLP-projector could be further replaced by a high intensity lamp that provides a uniform light. In the system, the

patterns to create virtual electrodes would be generated by Liquid Crystal Device (LCD) module that is placed between the light source and the OEW-device. With this direct image translation concept, while the elimination of lens and other instruments is performed, a thinner and more tolerant platform especially for portable applications can be developed, similarly as it has already been demonstrated for microparticle manipulation [107].

REFERENCES

1 Berthier, J. 2008. *Microdrops and Digital Microfluidics.* William Andrew Publishing.

2 Lippmann, M.G. 1875. *Relations entre les ph´enom`enes ´electriques et capillaries*. Annales de Chimie et de Physique, Vol. 5 (11), pp. 494-549.

3 Mugele, F., Baret, J.C. 2005. *Electrowetting: from basics to applications.* Journal of Physics Condensed Matter, Vol. 17 (28), pp. R705-R774.

4 Harrison, D.J., Manz, A., Fan, Z., Lüdi, H., Widmer, H.M. 1992. *Capillary electrophoresis and sample injection systems integrated on a planar glass chip.* Analytical Chemistry, Vol. 64 (17), pp. 1926-1932.

5 Haeberle, S., Zengerle, R. 2007. *Microfluidic platforms for lab-on-a-chip applications.* Lab on a Chip - Miniaturisation for Chemistry and Biology, Vol. 7 (9), pp. 1094-1110.

6 Luk, V.N., Wheeler, A.R. 2009. *A digital microfluidic approach to proteomic sample processing*. Analytical Chemistry, Vol. 81 (11), pp. 4524-4530.

7 Miller, E.M., Wheeler, A.R. 2009. *Digital bioanalysis.* Analytical and Bioanalytical Chemistry, Vol. 393 (2), pp. 419-426.

8 Fair, R.B. 2007. *Digital microfluidics: Is a true lab-on-a-chip possible?* Microfluidics and Nanofluidics, Vol. 3 (3), pp. 245-281.

9 Schwartz, J.A., Vykoukal, J.V., Gascoyne, P.R.C. 2004. *Droplet-based chemistry on a programmable micro-chip*. Lab on a Chip - Miniaturisation for Chemistry and Biology, Vol. 4 (1), pp. 11-17.

10 Chen, C.-H., Tsai, S.-L., Jang, L.-S. 2009. *Droplet creation using liquid dielectrophoresis.* Sensors and Actuators, B: Chemical, Vol. 142 (1), pp. 369-376.

11 Jones, T.B., Gunji, M., Washizu, M., Feldman, M.J. 2001. *Dielectrophoretic liquid actuation and nanodroplet formation.* Journal of Applied Physics, Vol. 89 (2), pp. 1441-1448.

12 Deval, J., Tabeling, P., Ho, C. M. 2002. *A Dielectrophoretic Chaotic Mixer*. 15th IEEE International Conference on MEMS (MEMS 2002), Las Vegas, NV, pp. 36–39.

13 Young, P.M., Mohseni, K. 2009. *Force Characterization of Dielectrophoresis in Droplet Transport*. Annals of the New York Academy of Sciences 1161, pp. 463-471.

14 Young, P.M., Mohseni, K. 2008. *Calculation of DEP and EWOD forces for application in digital microfluidics.* Journal of Fluids Engineering, Transactions of the ASME, Vol. 130 (8), pp. 0816031-0816039.

15 Jones, T.B., Wang, K.-L., Yao, D.-J. 2004. *Frequency-dependent electromechanics of aqueous liquids: Electrowetting and dielectrophoresis.* Langmuir, Vol. 20 (7), pp. 2813-2818.

16 Torkkeli, A. 2003. *Droplet microfluidics on a planar surface.* Dissertation for the degree of Doctor of Science in Technology, Helsinki University of Technology.

17 Berge, B. 1993. *Electrocapillarite et mouillage de films isolants par l'eau*. (*Electrocapillarity and wetting of insulator films by water*). Comptes rendus de l'Acad´emie des Sciences, S´eries II , Vol. 317, pp. 157–163.

18 Shapiro, B., Moon, H., Garrell, R.L., Kim, C.-J. 2003. *Equilibrium behavior of sessile drops under surface tension, applied external fields, and material variations.* Journal of Applied Physics, Vol. 93 (9), pp. 5794-5811.

19 Jones, T.B. 2009. *More about the electromechanics of electrowetting.* Mechanics Research Communications, Vol. 36 (1), pp. 2-9.

20 Berthier, J., Clementz, Ph., Raccurt, O., Jary, D., Claustre, P., Peponnet, C., Fouillet, Y. 2006. *Computer aided design of an EWOD microdevice.* Sensors and Actuators, A: Physical, Vol. 127 (2), pp. 283-294.

21 Lee, J., Moon, H., Fowler, J., Schoellhammer, T., Kim, C.-J. 2002. *Electrowetting and electrowetting-on-dielectric for microscale liquid handling.* Sensors and Actuators, A: Physical, Vol. 95 (2-3), pp. 259-268.

22 Moon, H., Cho, S.K., Garrell, R.L., Kim, C.-J. 2002. *Low voltage electrowetting-on-dielectric.* Journal of Applied Physics, Vol. 92 (7), pp. 4080-4087.

23 DuPont company web page. [WWW]. [Cited 20.4.2010]. Available at: http://www2.dupont.com/DuPont_Home/en_US/index.html/.

24 Pollack, MG. 2001. *Electrowetting-based microactuation of droplets for digital microfluidics.* Dissertation for the degree of Doctor of Science in Technology, Duke University.

25 Berry, S., Kedzierski, J., Abedian, B. 2006. *Low voltage electrowetting using thin fluoroploymer films* [sic]. Journal of Colloid and Interface Science, Vol. 303 (2), pp. 517-524.

26 Cho, S.K., Kim, C.-J. 2003. *Particle Separation and Concentration Control for Digital Microfluidic Systems.* IEEE 16th International Conference on Micro Electro Mechanical Systems, pp. 686-689.

27 Pollack, M.G, Fair R.B., Shenderov A.D. 2000. *Electrowetting-based actuation of liquid droplets for microfluidic applications*. Applied Physics Letters, Vol. 77 (11), pp. 1725-1726.

28 Moon, I., Kim, J. 2006. *Using EWOD (electrowetting-on-dielectric) actuation in a micro conveyor system.* Sensors and Actuators, A: Physical, Vol. 130-131 (special issue), pp. 537-544.

29 Abdelgawad, M., Park, P., Wheeler, A.R. 2009. *Optimization of device geometry in single-plate digital microfluidics.* Journal of Applied Physics 105 (9), art. no. 094506.

30 Cho, S.K., Moon, H., Kim, C.-J. 20003. *Creating, transporting, cutting, and merging liquid droplets by electrowetting-based actuation for digital microfluidic circuits.* Journal of Microelectromechanical Systems, Vol. 12 (1), pp. 70-80.

31 Verheijen, H.J.J, Prins, M.W. J. 1999. *Reversible electrowetting and trapping of charge: model and experiments.* Langmuir, Vol. 15 (20), pp. 6616–6620.

32 Restolho, J., Mata, J.L., Saramago, B. 2009. *Electrowetting of Ionic Liquids: Contact Angle Saturation and Irreversibility.* Journal of Physical Chemistry C, Vol. 113 (21), pp. 9321-9327.

33 Vallet, M., Vallade, M., Berge, B. 1999. *Limiting phenomena for the spreading of water on polymer films by electrowetting.* European Physical Journal B, Vol. 11 (4), pp. 583-591.

34 Peykov, V., Quinn, A., Ralston, J. 2000. *Electrowetting: a model for contact angle saturation.* Colloid and Polymer Science, Vol. 278 (8), pp. 789-793.

35 Quilliet, C., Berge, B. 2001. *Electrowetting: A recent outbreak.* Current Opinion in Colloid and Interface Science, Vol. 6 (1), pp. 34–39.

36 Blake, T. D. Clarke, A., Stattersfield, E. H. 2000. *Investigation of electrostatic assist in dynamic wetting.* Langmuir, Vol. 16 (6), pp. 2928– 2935.

37 Song, J.H., Evans, R., Lin, Y.-Y., Hsu, B.-N., Fair, R.B. 2009. *A scaling model for electrowetting-on-dielectric microfluidic actuators.* Microfluidics and Nanofluidics, Vol. 7 (1), pp. 75-89.

38 Srinivasan, V., Pamula, K., Fair R. B. 2004. *An integrated digital microfluidic lab-on-a-chip for clinical diagnostics on human physiological fluids.* Lab on a Chip - Miniaturisation for Chemistry and Biology, Vol. 4 (4), pp. 310-315.

39 Seyrat, E., Hayes, R.A. 2001. *Amorphous fluoropolymers as insulators for reversible low-voltage electrowetting.* Journal of Applied Physics, Vol. 90 (3), pp. 1383-1386.

40 Abdelgawad, M., Wheeler, A.R. 2008. *Low-cost, rapid-prototyping of digital microfluidics devices.* Microfluidics and Nanofluidics, Vol. 4 (4), pp. 349-355.

41 Bayiati P., Tserepi A., Petrou P.S., Kakabakos S.E., Misiakos K., Gogolides E. 2007. *Electrowetting on plasma-deposited fluorocarbon hydrophobic films for biofluid transport in microfluidics.* Journal of Applied Physics, Vol. 101 (10), art. no. 103306.

42 Yoon J.-Y., Garrell R.L. 2003. *Preventing biomolecular adsorption in electrowetting-based biofluidic chips.* Analytical Chemistry, Vol. 75 (19), pp. 5097-5102.

43 Yang, Z., Chakrabarty, K. 2009. *Cross-contamination avoidance for droplet routing in digital microfluidic biochips.* Proceedings-Design, Automation and Test in Europe, DATE , art. no. 5090864, pp. 1290-1295.

44 Wu, J., Yue, R., Zeng, X., Kang, M., Wang, Z., Liu, L. 2006. *An open-configuration electrowetting-based biofluidics actuation for preventing biomolecular adsorption.* Proceedings of 1st IEEE International Conference on Nano Micro Engineered and Molecular Systems, 1st IEEE-NEMS , art. no. 4135151, pp. 1152-1155.

45 Luk, V.N., Mo, G.Ch., Wheeler, A.R. 2008. *Pluronic additives: A solution to sticky problems in digital microfluidics.* Langmuir, Vol. 24 (12), pp. 6382-6389.

46 Yang, H., Luk, V.N., Abelgawad, M., Barbulovic-Nad, I., Wheeler, A.R. 2009. *A world-to-chip interface for digital microfluidics*. Analytical Chemistry, Vol. 81 (3), pp. 1061-1067.

47 Chatterjee, D., Hetayothin, B., Wheeler, A.R., King, D.J., Garrell, R.L. 2006. *Droplet-based microfluidics with nonaqueous solvents and solutions.* Lab on a Chip - Miniaturisation for Chemistry and Biology, Vol. 6 (2), pp. 199-206.

48 Chiou, P.-Y., Moon, H., Toshiyoshi, H., Kim C.-J., Wu, M.C. 2003. *Light actuation of liquid by optoelectrowetting.* Sensors and Actuators, A: Physical, Vol. 104 (3), pp. 222–228.

49 Chiou, P.-Y., Chang, Z., Wu, M.C. 2008. *Droplet manipulation with light on optoelectrowetting device*. Journal of Microelectromechanical Systems, Vol. 17 (1), pp. 133-138.

50 Chiou, P.Y., Park, S.-Y., Wu, M.C. 2008. *Continuous optoelectrowetting for picoliter droplet manipulation.* Applied Physics Letters, Vol. 93 (22), art. no. 221110.

51 Krogmann, F., Qu, H., Mönch, W., Zappe, H. 2008. *Push/pull actuation using opto-electrowetting*. Sensors and Actuators, A: Physical, Vol. 141 (2), pp. 499-505.

52 Chuang, H.-S., Kumar, A., Wereley, S.T. 2008. *Open optoelectrowetting droplet actuation*. Applied Physics Letters, Vol. 93 (6), art. no. 064104.

53 Inui, N. 2006. *Relationship between contact angle of liquid droplet and light beam position in optoelectrowetting*. Sensors and Actuators, A: Physical, Vol. 140 (1), pp. 123-130.

54 Wang W., Lin Y.-H., Guan R.-S., Wen T.-C., Guo T.-F., Lee G.-B. 2009. *Bulk-heterojunction polymers in optically- induced dielectrophoretic devices for the manipulation of microparticles.* Optics Express, Vol. 17 (20), pp. 17603-17613.

55 Pohl, H. 1978. *Dielectrophoresis.* Cambridge University Press, Cambridge, UK.

56 Chiou, P.-Y., Chang, Z., Wu, M.C. 2003. *A novel optoelectronic tweezer using light induced dielectrophoresis*. IEEE/LEOS International Conference on Optical MEMS, Kona, Hawaii, USA, pp. 8–9.

57 Chiou, P.-Y., Ohta, A.T., Wu, M.C. 2005. *Massively parallel manipulation of single cells and microparticles using optical images.* Nature, 436: pp. 370–372.

58 Ohta, A.T., Chiou, P.-Y., Han, T.H., Liao, J.C., Bhardwaj, U., McCabe, E.R.B., Yu, F., Sun R., Wu, M.C. 2007. *Dynamic Cell and Microparticle Control via Optoelectronic Tweezers.* Journal of Microelectromechanical Systems, Vol. 16 (3), pp.491–499.

59 Chiou, P.-Y., Ohta, A.T, Wu, M.C. 2005. *Microvison-activated automatic optical manipulator for microscopic particles* [sic]. IEEE 18th International Conference on Micro Electro Mechanical Systems, pp. 682- 685.

60 Hsu, H.Y., Ohta, A.T., Chiou, P.-Y., Jamshidi, A., Wu, M.C. 2007. *Phototransistor-based optoelectronic tweezers for cell manipulation in highly conductive solution*. TRANSDUCERS and EUROSENSORS '07 - 4th International Conference on Solid-State Sensors, Actuators and Microsystems, art. no. 4300171, pp. 477-480.

61 Ohta, A.T., Hsu, H.Y., Jamshidi, A., Wu, M.C. 2008. *Optical MEMS and nano-photonics for diagnostics*. IEEE-BIOCAS Biomedical Circuits and Systems Conference, BIOCAS 2008, art. no. 4696945, pp. 345-348.

62 Ho, C.-M. 2001. *Fluidics-the link between micro and nano sciences and technologies.* IEEE 14th International Conference on Micro Electro Mechanical Systems, pp. 375-384.

63 Lin, W.-Y., Lin Y.-H., Lee, G.-B. 2009. C*ontiunous micro-particle separation using optically-induced dielectrophoretic forces* [sic]. IEEE 22nd International Conference on Micro Electro Mechanical Systems, pp. 47–50.

64 Khine, M., Lau, A., Ionescu-Zanetti, C., Seo, J., Lee, L.P. 2005. *A single cell electroporation chip.* Lab on a Chip - Miniaturisation for Chemistry and Biology, Vol. 5 (1), pp. 38-43.

65 Weaver, J. C. 2000. *Electroporation of Cells and Tissues.* IEEE Transactions on Plasma Science, Vol. 28 (1), pp. 24-33.

66 Weaver, J.C., Chizmadzhev, Y.A. 1996. *Theory of electroporation: A review.* Bioelectrochemistry and Bioenergetics, Vol. 41 (2), pp. 135-160.

67 Valley, J.K., Neale, S., Hsu, H.-Y., Ohta, A.T., Jamshidi, A., Wu, M.C. 2009. *Parallel single-cell light-induced electroporation and dielectrophoretic manipulation.* Lab on a Chip - Miniaturisation for Chemistry and Biology, Vol. 9 (12), pp. 1714-1720.

68 Lee, S.-W., Tai, Y.-C. 1999. *A micro cell lysis device.* Sensors and Actuators A: Physical, Vol. 73(1), pp. 74-79.

69 Lin, Y.-H., Lee, G.-B. 2009. *An optically induced cell lysis device using dielectrophoresis.* Applied Physical Letters, Vol. 94, pp. 033901-1-033901-3.

70 Valley, J.K., Ohta, A.T., Hsu, H.-Y., Neale, S.L., Jamshidi, A., Wu, M.C. 2009. *Optoelectronic Tweezers as a Tool for Parallel Single-Cell Manipulation and Stimulation.* IEEE Transactions on Biomedical Circuits and Systems, Vol. 3 (6), pp. 424-431.

71 Ramadan, Q., Samper, V., Poenar, D., Liang, Z., Yu, C., Lim, T.M. 2006. *Simultaneous cell lysis and bead trapping in a continuous flow microfluidic device.* Sensors and Actuators, B: Chemical, Vol. 113 (2), pp. 944–955.

72 Takayama, Y., Moriguchi, H., Saito, A., Kotani, K., Jimbo, Y. 2009. *Ensemble stimulation of embryoid bodies using microfabricated ITO substrates.* Annual International Conference of the IEEE Engineering in Medicine and Biology Society, pp. 5993-5996.

73 Sauer, H., Rahimi, G., Hescheler, J., Wartenberg, M. 1999. *Effects of Electrical Fields on Cardiomyocyte Differentiation of Embryonic Stem Cells.* Journal of Cellular Biochemistry, Vol. 75 (4), pp. 710–723.

74 Sauer, H., Bekhite, M.M., Hescheler, J., Wartenberg, M. 2005. *Redox control of angiogenic factors and CD31-positive vessel-like structures in mouse embryonic stem cells after direct current electrical field stimulation.* Experimental Cell Research, Vol. 304 (2), pp. 380– 390.

75 Radisic, M., Park, H., Shing, H., Consi, T., Schoen, F.J., Langer, R., Freed, L.E., Vunjak-Novakovic, G. 2004. *Functional assembly of engineered myocardium by electrical stimulation of cardiac myocytes cultured on scaffolds.* Proceedings of the National Academy of Sciences of the United States of America, Vol. 101 (52), pp. 18129-18134.

76 Serena, E., Figallo, E., Tandon, N., Cannizzaro, C., Gerecht, S., Elvassore, N., Vunjak-Novakovic, G. 2009. *Electrical stimulation of human embryonic stem cells: Cardiac differentiation and the generation of reactive oxygen species.* Experimental Cell Research, Vol. 315 (20), pp. 3611-3619.

77 Shah, G.J., Chiou, P.-Y., Gong, J., Ohta, A.T., Chou, J.B., Wu, M.C., Kim, C.-J. 2006. *Integrating Optoelectronic Tweezers for Individual Particle Manipulation with Digital Microfluidics Using Electrowetting-On-Dielectric (EWOD).* IEEE 19th International Conference on Micro Electro Mechanical Systems, pp. 130–133.

78 Shah, G.J., Ohta, A.T., Chiou, P.-Y., Wu, M.C., Kim, C.-J.C.J. 2009. *EWOD-driven droplet microfluidic device integrated with optoelectronic tweezers as an automated platform for cellular isolation and analysis.* Lab on a Chip - Miniaturisation for Chemistry and Biology, Vol. 9 (12), pp. 1732-1739.

79 Ohta, A.T. 2008. *Optofluidic Devices for Cell, Microparticle, and Nanoparticle Manipulation*. Dissertation for the degree of Doctor of Science in Technology, Electrical Engineering and Computer Sciences University of California, pp. 125-134.

80 Whitesides, G.M. 2006. *The origins and the future of microfluidics.* Nature, Vol. 442, pp. 368-373.

81 Cheng, J.-Y., Hsiung, L.-C. 2004. *Electrowetting (EW)-based valve combined with hydrophilic teflon microfluidic guidance in controlling continuous fluid flow.* Biomedical Microdevices, Vol. 6 (4), pp. 341-347.

82 Fejtl, M., Stett, A., Nisch, W., Boven, K.-H., Möller, A. 2006. *On micro-electrode array revival: its development, sophistication of recording, and stimulation.* Advances in Network Electrophysiology Using Multi-Electrode Arrays. Taketani M., Baudry M., Eds. New York: Springer, pp. 24–37.

83 Kristensen, B.W., Noraberg, J., Thiébaud, P., Koudelka-Hep, M., Zimmer, J. 2001. *Biocompatibility of silicon-based arrays of electrodes coupled to organotypic hippocampal brain slice cultures.* Brain Research, Vol. 896 (1-2), pp. 1-17.

84 Neumann, A., Reske, T., Held, M., Jahnke, K., Ragoß, C., Maier, H.R. 2004. *Comparative investigation of the biocompatibility of various silicon nitride ceramic qualities in vitro*. Journal of Materials Science: Materials in Medicine, Vol. 15 (10), pp. 1135-1140.

85 Sohrabi, A., Holland, C., Kue, R., Nagle, D., Hungerford, D.S., Frondoza, C.G. 2000. *Proinflammatory cytokine expression of IL-1β and TNF-α by human osteoblast-like MG-63 cells upon exposure to silicon nitride in vitro.* Journal of Biomedical Materials Research, Vol. 50 (1), pp. 43-49.

86 Amaral, M., Lopes, M.A., Silva, R.F., Santos, J.D. 2002. *Densification route and mechanical properties of Si3N4-bioglass biocomposites.* Biomaterials, Vol. 23 (3), pp. 857–862.

87 Gascoyne, P.R.C., Vykoukal, J.V. 2004. *Dielectrophoresis-Based Sample Handling in General-Purpose Programmable Diagnostic Instruments*. Proceedings of the IEEE, Vol. 92 (1), pp. 22-42.

88 The Control Engineering Group, The Department of Automation and Systems Technology, The Faculty of Electronics, Communications and Automation, Helsinki University of Technology research group web page [WWW]. [Cited 26.4.2010]. Available at: http://autsys.tkk.fi/en/MicroNanorobotics.

89 Micronova web page. [WWW]. [Cited 26.4.2010]. Available at: http://www.micronova.fi/.

90 Oxford Instruments, *Plasmalab 80 Plus product web page*. [WWW]. [Cited 26.4.2010]. Available at: http://www.oxfordplasma.de/systems/80plus.htm.

91 Praezisions Glas & Optik GmbH company web page. [WWW]. [Cited 26.4.2010]. Available at: http://www.pgo-online.com/intl/index.html.

92 Canon, *Canon Digital IXUS 800 IS product web page*. [WWW]. [Cited 15.5.2010]. Available at: http://www.canon.co.uk/for_home/product_finder/cameras/ digital_camera/ ixus/ digital_ixus_800_is/index.aspx.

93 Quinn, A., Sedev, R., Ralston, J. 2005. *Contact angle saturation in electrowetting*. Journal of Physical Chemistry B, Vol. 109 (13), pp. 6268-6275.

94 Navitar, *12x Zoom Vision System product web page*. [WWW]. [Cited 21.5.2010] Available at: http://www.machinevision.navitar.com/catalog/?c=372.

95 Sony, *XCD-X710 data brochure*. [WWW]. [Cited 21.5.2010]. Available at: http://pro.sony.com/bbsccms/static/files/mkt/industrialautomation/brochures/ieee1394/XCDSeriesBrochure.pdf.

96 Agilent, *33120A data sheet*. [WWW]. [Cited 25.5.2010]. Available at: http://cp.literature.agilent.com/litweb/pdf/5968-0125EN.pdf.

97 Piezomechanik GmbH, *SVR-150-3 data brochure*. [WWW]. [Cited 27.5.2010]. Available at: http://www.piezomechanik.com/f/core/frontend/http/http.php?dl=55-file-1.

98 InFocus company web page. [WWW]. [Cited 27.5.2010]. Available at: http://www.infocus.com/.

99 MEL Mikroelektronik GmbH company web page. [WWW]. [Cited 28.5.2010]. Available at: http://www.melsensor.de/en-home.html?Itemid=103.

100 García-Sánchez, P., Ramos, A., Mugele, F. 2010. *Electrothermally driven flows in ac electrowetting*. Physical Review E - Statistical, Nonlinear, and Soft Matter Physics, Vol. 81 (1), art. no. 015303.

101Neuman, M. R. 2000. *Biopotential Electrodes*. The Biomedical Engineering Handbook: Second Edition, Boca Raton: CRC Press LLC, Chapter 48.

102 Department of Biomedical Engineering, Tampere University of Technology web page. [WWW]. [Cited 29.5.2010]. Available at: http://www.tut.fi/index.cfm?mainsel=20596&sel=20596&Show=33348&siteid=213&CFID=175522355&CFTOKEN=18272462.

103 Solartron Analytical company web page. [WWW]. [Cited 30.5.2010]. Available at: http://www.solartronanalytical.com/index.htm.

104Standa, *Translation & Rotation Stages product web page*. [WWW]. [Cited 31.5.2010]. Available at: http://www.standa.lt/products/catalog/translation_rotation.

105 Switchbox, *6303DS data sheet*. [WWW]. [Cited 31.5.2010] Available at: http://www.craftec.info/productPDF/Switchbox_3000_6000.pdf.

106 Pei, S.N., Valley, J.K., Neale, S.L., Jamshidi, A., Hsu, H.-Y., Wu, M.C. 2010. *Light-actuated digital microfluidics for large-scale, parallel manipulation of arbitrarily sized droplets*. Proceedings of the IEEE International Conference on Micro Electro Mechanical Systems (MEMS), art. no. 5442519, pp. 252-255.

107 Choi, W., Kim, S.-H., Jang, J., Park, J.-K. 2007. *Lab-on-a-display: A new microparticle manipulation platform using a liquid crystal display (LCD)*. Microfluidics and Nanofluidics, Vol. 3 (2), pp. 217-225.

APPENDIX: TABLES OF EWOD-TESTS

The results of the EWOD measurements presented in Chapter 4 are listed. In the tables, mean values of two separate analyses are provided.

Table A.1: The first EWOD-test with DI water droplet.

DI Test #	Image #	U [V]	Left θ [°]	Right θ [°]	Area [pixels]	$2*r_c$ [pixels]	Video [fps]	Reference image [#]	Time [s]	Standard deviation			
										Left θ	Right θ	Area	$2*r_c$
1	800	0	98.74	92.28	1.50E+05	557.5	30	800	0.00	4.05	0.44	1756.5	2.12
	2842	0	85.40	82.53	1.35E+05	561.5	30	800	68.07	2.16	0.73	1639.8	0.71
	2843	9.6	84.63	83.45	1.34E+05	560.5	30	800	68.10	1.81	1.66	1637.7	0.71
	2850	9.6	88.06	83.22	1.34E+05	559.5	30	800	68.33	5.08	1.49	1651.1	3.54
	2870	9.6	86.03	83.05	1.34E+05	561	30	800	69.00	2.32	1.44	1651.8	1.41
	2900	9.6	84.71	82.06	1.34E+05	562.5	30	800	70.00	1.70	0.60	1645.4	0.71
	3500	9.6	83.52	79.77	1.30E+05	561.5	30	800	90.00	2.26	0.67	1657.5	0.71
	3501	27.2	82.65	79.80	1.30E+05	560.5	30	800	90.03	2.09	0.63	1635.5	0.71
	3510	27.2	82.37	79.64	1.30E+05	562.5	30	800	90.33	2.68	0.66	1644.7	0.71
	3550	27.2	82.10	80.27	1.30E+05	562	30	800	91.67	2.15	2.07	1642.6	1.41
	3600	27.2	83.00	80.20	1.30E+05	561	30	800	93.33	3.60	0.87	1656.8	1.41
	4000	27.2	80.70	78.61	1.28E+05	562	30	800	106.67	2.44	1.72	1647.6	1.41
	4001	32.1	80.84	78.71	1.28E+05	561.5	30	800	106.70	2.14	1.16	1655.3	0.71
	4010	32.1	80.07	78.47	1.27E+05	562	30	800	107.00	1.15	1.68	1657.5	0.00
	4050	32.1	81.14	78.73	1.27E+05	561	30	800	108.33	2.46	1.68	1657.5	1.41
	4100	32.1	83.10	77.74	1.26E+05	560	30	800	110.00	5.28	1.51	1653.2	2.83
	4479	32.1	79.08	75.53	1.24E+05	562.5	30	800	122.63	0.64	1.24	1637.7	0.71
	4480	0	78.77	76.44	1.24E+05	563	30	800	122.67	3.70	2.08	1620.7	2.83
	4490	0	80.70	74.74	1.25E+05	562.5	30	800	123.00	4.05	0.04	1661.7	0.71
	4530	0	77.91	74.58	1.24E+05	564.5	30	800	124.33	2.61	0.39	1656.8	0.71
	4600	0	78.34	74.43	1.24E+05	564	30	800	126.67	1.89	0.49	1646.9	0.00
	5000	0	79.39	76.30	1.23E+05	550	30	800	140.00	2.47	0.40	1600.9	0.00
	5769	0	77.98	76.53	1.16E+05	537	30	800	165.63	2.85	1.23	1556.3	1.41

Appendix

Table A.2: The second EWOD-test with DI water droplet.

DI Test #	Image #	U [V]	Left θ [°]	Right θ [°]	Area [pixels]	$2*r_c$ [pixels]	Video [fps]	Reference image [#]	Time [s]	Standard deviation			
										Left θ	Right θ	Area	$2*r_c$
2	1001	0	91.67	91.89	1.50E+05	602	30	1140	-4.63	0.37	0.47	650.5	0.00
	1140	0	90.59	93.18	1.51E+05	600	30	1140	0.00	0.03	0.26	658.3	0.00
	1501	0	89.10	91.92	1.50E+05	599.5	30	1140	12.03	0.53	0.57	651.2	0.71
	1502	6.3	88.59	91.75	1.50E+05	599.5	30	1140	12.07	0.35	0.01	649.8	0.71
	1525	6.3	88.61	91.90	1.50E+05	600	30	1140	12.83	0.08	0	649.1	0.00
	1600	6.3	89.85	91.52	1.49E+05	598	30	1140	15.33	0.48	0.01	647.0	0.00
	2051	6.3	87.72	90.24	1.46E+05	598	30	1140	30.37	0.56	0.73	13.4	2.83
	2052	21.1	87.95	88.08	1.46E+05	599	30	1140	30.40	0.64	0.12	648.4	0.00
	2060	21.1	85.17	88.00	1.45E+05	600	30	1140	30.67	0.11	0.26	646.3	0.00
	2100	21.1	85.97	87.23	1.45E+05	598	30	1140	32.00	0.08	0.44	644.2	0.00
	2210	21.1	85.04	86.83	1.44E+05	598	30	1140	35.67	0.15	0.53	647.7	1.41
	2211	32.1	84.72	86.77	1.44E+05	600	30	1140	35.70	0.18	0.28	648.4	0.00
	2217	32.1	86.82	84.90	1.41E+05	599	30	1140	35.90	0.16	0.28	647.0	0.00
	2400	32.1	84.94	85.05	140197.5	599	30	1140	42.00	0.47	0.30	648.4	0.00
	2660	32.1	84.75	83.75	1.38E+05	597.5	30	1140	50.67	0.09	0.63	649.1	0.71
	2661	0	84.02	82.30	1.38E+05	599	30	1140	50.70	0.50	0.15	647.0	0.00
	2700	0	83.75	82.27	1.37E+05	601	30	1140	52.00	0.45	0.51	647.7	0.00
	3000	0	84.01	82.00	1.36E+05	599	30	1140	62.00	0.89	0.30	644.2	0.00
	3630	0	81.75	76.59	1.34E+05	601	30	1140	83.00	0.41	0.01	649.1	0.00

Appendix

Table A.3: The third EWOD-test with DI water droplet.

DI Test #	Image #	U [V]	Left θ [°]	Right θ [°]	Area [pixels]	$2*r_c$ [pixels]	Video [fps]	Reference image [#]	Time [s]	Standard deviation			
										Left θ	Right θ	Area	$2*r_c$
3	280	0	88.72	104.68	8.20E+04	375.5	7.5	280	0.00	2.05	1.15	2.1	0.71
	926	0	77.04	98.87	7.18E+04	377.0	7.5	280	86.13	1.48	0.70	0.0	0.00
	927	2.3	77.11	98.94	7.12E+04	376.5	7.5	280	86.27	1.76	1.08	2.1	0.71
	932	2.3	76.53	98.45	7.09E+04	377.5	7.5	280	86.93	1.60	1.43	2.1	0.71
	940	2.3	75.73	96.01	6.99E+04	384.5	7.5	280	88.00	1.55	1.03	2.8	0.71
	1196	2.3	76.91	93.88	6.67E+04	372.0	7.5	280	122.13	1.84	0.32	0.0	0.00
	1197	5.6	77.59	93.63	6.55E+04	370.0	7.5	280	122.27	2.24	1.06	0.7	0.00
	1210	5.6	76.91	93.99	6.77E+04	372.5	7.5	280	124.00	2.03	0.47	0.7	0.71
	1476	5.6	75.34	89.92	6.11E+04	367.5	7.5	280	159.47	3.31	0.60	55.2	0.71
	1478	0	74.54	90.24	6.05E+04	370.0	7.5	280	159.73	1.58	0.82	0.7	0.00
	1490	0	74.62	89.98	6.13E+04	368.0	7.5	280	161.33	2.23	0.01	0.7	0.00
	1640	0	76.96	91.75	5.75E+04	355.5	7.5	280	181.33	4.40	1.36	0.7	0.71
	1642	6	74.83	91.76	5.84E+04	358.0	7.5	280	181.60	2.32	0.20	0.7	0.00
	1650	6	74.75	92.33	5.80E+04	357.0	7.5	280	182.67	2.29	0.58	0.0	0.00
	1660	6	73.19	91.87	5.85E+04	357.0	7.5	280	184.00	1.93	0.41	3.5	0.00
	1800	6	72.15	89.98	5.55E+04	353.0	7.5	280	202.67	2.27	0.32	3.5	0.00
	1957	6	70.70	88.79	5.41E+04	349.0	7.5	280	223.60	1.88	0.55	0.7	0.00
	1958	0	71.01	88.77	5.35E+04	349.0	7.5	280	223.73	1.96	0.50	0.0	0.00
	1965	0	68.17	87.58	5.24E+04	354.0	7.5	280	224.67	2.20	0.22	0.0	0.00
	1970	0	64.91	81.36	5.11E+04	369.0	7.5	280	225.33	2.80	1.53	0.7	0.00
	1971	0	65.52	82.41	5.16E+04	366.0	7.5	280	225.47	2.39	0.77	1.4	0.00
	2077	0	67.17	83.38	5.13E+04	355.5	7.5	280	239.60	2.37	0.73	3.5	0.71
	2078	32.1	67.28	83.40	5.07E+04	355.5	7.5	280	239.73	2.45	0.73	4.2	0.71

Appendix

Table A.4: The first EWOD-test with NaCl droplet.

NaCl Test #	Image #	U [V]	Left θ [°]	Right θ [°]	Area [pixels]	$2*r_c$ [pixels]	Video [fps]	Reference image [#]	Time [s]	Standard deviation			
										Left θ	Right θ	Area	$2*r_c$
1	227	0	91.78	89.22	1.93E+05	669	7.5	227	0.00	0.26	0.45	7.1	0.00
	274	0	87.39	87.39	1.93E+05	677	7.5	227	6.27	0.06	0.01	4.2	0.00
	275	7.7	67.68	70.53	1.81E+05	775.5	7.5	227	6.40	0.12	1.97	6.4	2.12
	277	7.7	64.95	66.64	1.81E+05	786	7.5	227	6.67	0.32	0.87	7.8	1.41
	289	7.7	66.84	67.72	1.79E+05	780.5	7.5	227	8.27	0.31	0.87	4.2	2.12
	686	7.7	61.96	63.35	1.71E+05	780	7.5	227	61.20	0.60	0.06	25.5	1.41
	688	0	62.77	63.77	1.71E+05	779.5	7.5	227	61.47	0.72	0.34	3.5	2.12
	888	0	59.86	60.71	1.63E+05	785	7.5	227	88.13	0.63	0.06	5.7	1.41
	900	32.1	59.04	58.70	1.62E+05	786.5	7.5	227	89.73	0.39	0.20	4.9	0.71
	1035	32.1	60.01	59.67	1.60E+05	778	7.5	227	107.73	1.22	0.16	24.0	2.83
	1054	0	57.13	59.92	1.58E+05	781.5	7.5	227	110.27	0.34	0.26	8.5	0.71
	1133	0	56.32	58.67	1.54E+05	778.5	7.5	227	120.80	0.60	0.46	17.0	2.12

Appendix

Table A.5: The second EWOD-test with NaCl droplet.

NaCl Test #	Image #	U [V]	Left θ [°]	Right θ [°]	Area [pixels]	$2*r_c$ [pixels]	Video [fps]	Reference image [#]	Time [s]	Standard deviation			
										Left θ	Right θ	Area	$2*r_c$
2	0	0	92.93	92.94	1.98E+05	694.5	30	1001	-33.37	0.74	0.90	2938.7	0.71
	1001	0	90.93	87.94	1.98E+05	694.5	30	1001	0.00	0.85	1.15	2943.0	2.12
	1193	0	90.39	87.90	1.96E+05	692	30	1001	6.40	0.52	0.86	2930.3	1.41
	1194	8	90.65	87.83	1.97E+05	693	30	1001	6.43	0.94	0.91	2910.5	1.41
	1200	8	90.60	88.07	1.96E+05	692	30	1001	6.63	0.84	0.56	2911.9	1.41
	1230	8	90.75	87.40	1.97E+05	693.5	30	1001	7.63	1.34	0.94	2935.2	2.12
	1500	8	90.84	87.60	1.94E+05	691.5	30	1001	16.63	0.92	1.35	2935.2	2.12
	2000	8	88.56	85.25	1.92E+05	694	30	1001	33.30	1.15	0.84	2932.4	1.41
	2435	8	87.19	83.88	1.89E+05	693.5	30	1001	47.80	0.60	0.91	2900.6	0.71
	2436	17.4	87.41	84.08	1.89E+05	692.5	30	1001	47.83	0.69	0.97	2935.2	0.71
	2450	17.4	86.95	84.07	1.89E+05	692.5	30	1001	48.30	0.76	0.63	2922.5	0.71
	2500	17.4	88.28	83.57	1.88E+05	691	30	1001	49.97	1.07	0.68	2904.8	1.41
	3380	17.4	85.87	80.82	1.83E+05	691	30	1001	79.30	0.92	0.97	2930.3	1.41
	3381	32.1	84.75	80.95	1.83E+05	692.5	30	1001	79.33	0.85	0.92	2943.0	0.71
	3400	32.1	84.74	80.83	1.83E+05	692.5	30	1001	79.97	0.95	1.02	2925.3	0.71
	3500	32.1	84.11	80.53	1.82E+05	693.5	30	1001	83.30	0.74	1.02	2912.6	0.71
	4000	32.1	83.03	78.91	1.79E+05	691.5	30	1001	99.97	0.89	0.90	2909.0	0.71
	4425	32.1	81.84	77.78	1.76E+05	692.5	30	1001	114.13	0.89	0.94	2921.1	0.71
	4426	0	81.87	77.66	1.75E+05	690.5	30	1001	114.17	0.87	0.95	2920.4	0.71
	4440	0	81.84	77.81	1.76E+05	692.5	30	1001	114.63	0.89	0.93	2918.2	0.71
	4500	0	81.52	77.54	1.76E+05	691.5	30	1001	116.63	0.90	0.90	2914.0	0.71
	4800	0	80.38	76.46	1.73E+05	691.5	30	1001	126.63	1.02	1.04	2916.1	0.71
	5200	0	79.58	74.92	1.70E+05	689	30	1001	139.97	1.05	1.16	2899.1	1.41
	5515	0	78.30	73.47	1.68E+05	691	30	1001	150.47	1.16	1.16	2871.6	1.41

Appendix

Table A.6: The third EWOD-test with NaCl droplet.

NaCl Test #	Image #	U [V]	Left θ [°]	Right θ [°]	Area [pixels]	$2*r_c$ [pixels]	Video [fps]	Reference image [#]	Time [s]	Standard deviation			
										Left θ	Right θ	Area	$2*r_c$
3	280	0	88.72	104.68	8.20E+04	375.5	7.5	280	0.00	2.05	1.15	2.1	0.71
	926	0	77.04	98.87	7.18E+04	377.0	7.5	280	86.13	1.48	0.70	0.0	0.00
	927	2.3	77.11	98.94	7.12E+04	376.5	7.5	280	86.27	1.76	1.08	2.1	0.71
	932	2.3	76.53	98.45	7.09E+04	377.5	7.5	280	86.93	1.60	1.43	2.1	0.71
	940	2.3	75.73	96.01	6.99E+04	384.5	7.5	280	88.00	1.55	1.03	2.8	0.71
	1196	2.3	76.91	93.88	6.67E+04	372.0	7.5	280	122.13	1.84	0.32	0.0	0.00
	1197	5.6	77.59	93.63	6.55E+04	370.0	7.5	280	122.27	2.24	1.06	0.7	0.00
	1210	5.6	76.91	93.99	6.77E+04	372.5	7.5	280	124.00	2.03	0.47	0.7	0.71
	1476	5.6	75.34	89.92	6.11E+04	367.5	7.5	280	159.47	3.31	0.60	55.2	0.71
	1478	0	74.54	90.24	6.05E+04	370.0	7.5	280	159.73	1.58	0.82	0.7	0.00
	1490	0	74.62	89.98	6.13E+04	368.0	7.5	280	161.33	2.23	0.01	0.7	0.00
	1640	0	76.96	91.75	5.75E+04	355.5	7.5	280	181.33	4.40	1.36	0.7	0.71
	1642	6	74.83	91.76	5.84E+04	358.0	7.5	280	181.60	2.32	0.20	0.7	0.00
	1650	6	74.75	92.33	5.80E+04	357.0	7.5	280	182.67	2.29	0.58	0.0	0.00
	1660	6	73.19	91.87	5.85E+04	357.0	7.5	280	184.00	1.93	0.41	3.5	0.00
	1800	6	72.15	89.98	5.55E+04	353.0	7.5	280	202.67	2.27	0.32	3.5	0.00
	1957	6	70.70	88.79	5.41E+04	349.0	7.5	280	223.60	1.88	0.55	0.7	0.00
	1958	0	71.01	88.77	5.35E+04	349.0	7.5	280	223.73	1.96	0.50	0.0	0.00
	1965	0	68.17	87.58	5.24E+04	354.0	7.5	280	224.67	2.20	0.22	0.0	0.00
	1970	0	64.91	81.36	5.11E+04	369.0	7.5	280	225.33	2.80	1.53	0.7	0.00
	1971	0	65.52	82.41	5.16E+04	366.0	7.5	280	225.47	2.39	0.77	1.4	0.00
	2077	0	67.17	83.38	5.13E+04	355.5	7.5	280	239.60	2.37	0.73	3.5	0.71
	2078	32.1	67.28	83.40	5.07E+04	355.5	7.5	280	239.73	2.45	0.73	4.2	0.71
	2085	32.1	67.20	83.49	5.01E+04	354.5	7.5	280	240.67	2.17	0.45	72.1	0.71
	2400	32.1	64.21	80.58	4.53E+04	343.5	7.5	280	282.67	2.78	1.44	95.5	0.71
	2525	32.1	62.82	79.74	4.28E+04	340.0	7.5	280	299.33	3.15	1.40	104.7	0.00
	2526	0	62.34	79.81	4.30E+04	340.0	7.5	280	299.47	3.09	1.97	105.4	0.00
	2538	0	63.88	79.58	4.28E+04	339.5	7.5	280	301.07	1.12	1.65	101.8	0.71

Appendix

3	3150	0	86.74	84.64	9.89E+04	479	7.5	280	382.67	0.82	1.35	305.5	0.00
	3329	0	84.43	82.38	9.53E+04	479	7.5	280	406.53	0.45	0.72	307.0	0.00
	3330	32.1	84.53	84.79	9.56E+04	479.67	7.5	280	406.67	0.50	3.03	290.9	0.58
	3370	32.1	84.55	82.76	9.50E+04	476.33	7.5	280	412.00	0.93	1.41	302.1	0.58
	3450	32.1	83.23	81.16	9.30E+04	478	7.5	280	422.67	0.42	0.97	305.0	0.00
	3470	32.1	81.24	82.73	9.13E+04	477	7.5	280	425.33	0.56	1.38	307.0	0.00
	3571	32.1	80.53	82.01	8.87E+04	475.67	7.5	280	438.80	1.57	1.60	297.8	0.58
	3572	0	80.42	82.37	8.86E+04	476.33	7.5	280	438.93	1.08	1.62	303.7	0.58
	3600	0	80.07	81.98	8.91E+04	476	7.5	280	442.67	0.95	1.33	304.3	0.00
	3800	0	78.38	79.50	8.47E+04	475	7.5	280	469.33	0.78	1.62	305.9	0.00
	4000	0	74.84	78.39	8.18E+04	473	7.5	280	496.00	1.01	2.02	309.0	0.00
	4250	0	72.43	79.27	7.92E+04	473	7.5	280	529.33	1.39	5.72	306.6	1.00
	4336	0	71.66	79.07	7.74E+04	472.33	7.5	280	540.80	1.20	5.93	307.5	1.53

Appendix

Table A.7: The fourth EWOD-test with NaCl droplet.

NaCl Test #	Image #	U [V]	Left θ [°]	Right θ [°]	Area [pixels]	$2*r_c$ [pixels]	Video [fps]	Reference image [#]	Time [s]	Standard deviation			
										Left θ	Right θ	Area	$2*r_c$
4	730	0	87.83	86.33	9.11E+04	476	7.5	730	0.00	0.14	0.93	0.00	0.00
	1000	0	86.04	82.46	8.65E+04	475	7.5	730	36.00	0.72	2.05	15.56	1.41
	1200	0	83.03	78.14	8.34E+04	474.5	7.5	730	62.67	0.89	0.99	7.07	0.71
	1235	0	81.24	77.76	8.27E+04	474.5	7.5	730	67.33	1.17	0.97	0.71	0.71
	1236	12.6	82.48	77.96	8.30E+04	474	7.5	730	67.47	1.28	1.31	1.41	1.41
	1255	12.6	78.57	74.49	8.08E+04	483	7.5	730	70.00	1.27	2.15	1.41	1.41
	1268	12.6	77.68	74.21	8.06E+04	483	7.5	730	71.73	1.37	1.21	1.41	1.41
	1280	12.6	78.25	71.79	8.00E+04	486.5	7.5	730	73.33	1.87	1.72	16.26	2.12
	1400	12.6	73.78	69.52	7.91E+04	492	7.5	730	89.33	1.36	1.64	1.41	1.41
	1401	0	73.49	69.52	7.93E+04	493	7.5	730	89.47	1.86	1.80	2.83	2.83
	1680	0	69.11	64.77	7.37E+04	491.5	7.5	730	126.67	1.62	1.72	16.97	2.12
	1681	20.1	68.94	64.69	7.36E+04	492.5	7.5	730	126.80	2.33	1.55	0.71	2.12
	1685	20.1	64.49	62.56	7.36E+04	506.5	7.5	730	127.33	1.17	1.83	8.49	2.12
	1800	20.1	63.52	60.63	7.06E+04	505.5	7.5	730	142.67	2.94	1.75	3.54	3.54
	1801	0	63.12	60.65	7.13E+04	506.5	7.5	730	142.80	1.66	1.82	2.12	2.12
	1900	0	63.49	58.75	6.93E+04	504	7.5	730	156.00	1.78	1.88	9.90	2.83
	2133	0	58.68	54.85	6.54E+04	505	7.5	730	187.07	1.30	1.95	1.41	1.41
	2134	32.1	58.73	54.97	6.48E+04	505	7.5	730	187.20	1.34	1.73	1.41	1.41
	2160	32.1	57.84	54.60	6.51E+04	503	7.5	730	190.67	1.61	2.06	2.83	2.83
	2250	32.1	55.45	54.54	6.34E+04	506	7.5	730	202.67	0.32	0.00	1.41	1.41
	2251	0	55.60	54.46	6.37E+04	505	7.5	730	202.80	0	0	0	0
	2536	0	54.90	53.58	6.18E+04	503	7.5	730	240.80	0	0	0	0

Appendix

Table A.8: The fifth EWOD-test with NaCl droplet.

NaCl Test #	Image #	U [V]	Left θ [°]	Right θ [°]	Area [pixels]	$2*r_c$ [pixels]	Video [fps]	Reference image [#]	Time [s]	Standard deviation			
										Left θ	Right θ	Area	$2*r_c$
5	1400	0	91.30	93.37	1.23E+05	512	30	1400	0.00	0.12	0.19	1039.4	0
	2000	0	92.02	91.86	1.19E+05	507	30	1400	20.00	0.53	0.43	1011.2	1.41
	2200	0	88.95	89.15	1.18E+05	509.5	30	1400	26.67	0.39	0.01	1037.3	0.71
	2292	0	88.49	88.50	1.18E+05	510	30	1400	29.73	0.44	0.02	1033.1	1.41
	2294	15.1	88.05	88.66	1.18E+05	510.5	30	1400	29.80	0.18	0.00	1032.4	0.71
	2299	15.1	86.02	86.39	1.15E+05	513	30	1400	29.97	0.53	0.22	1033.8	1.41
	2300	15.1	86.05	85.59	1.16E+05	516.5	30	1400	30.00	0.65	0.09	1037.3	0.71
	2305	15.1	83.91	83.02	1.15E+05	522	30	1400	30.17	0.58	0.18	1030.3	1.41
	2308	15.1	82.99	82.02	1.13E+05	525	30	1400	30.27	0.64	0.05	1028.8	1.41
	2310	15.1	82.24	81.70	1.15E+05	527	30	1400	30.33	0.47	0.26	1026.0	1.41
	2313	15.1	82.05	80.96	1.14E+05	529	30	1400	30.43	0.41	0.06	1020.4	1.41
	2345	15.1	82.34	80.12	1.15E+05	530	30	1400	31.50	0.62	0.16	1016.8	1.41
	2500	15.1	81.02	79.66	1.13E+05	531	30	1400	36.67	0.37	0.01	1018.9	1.41
	2800	15.1	79.90	78.55	1.11E+05	531	30	1400	46.67	0.63	0.05	1017.5	1.41
	3000	15.1	78.81	77.57	1.10E+05	531	30	1400	53.33	0.37	0.01	1020.4	1.41
	3150	0	78.34	76.74	1.09E+05	531	30	1400	58.33	0.48	0.06	1016.1	1.41
	3333	0	77.59	76.26	1.08E+05	530.5	30	1400	64.43	0.71	0.20	1015.4	2.12
	3450	0	77.40	75.41	1.06E+05	530	30	1400	68.33	0.56	0.02	1020.4	1.41
	3536	0	77.79	75.34	1.05E+05	528	30	1400	71.20	0.75	0.21	1004.1	1.41